Germanium-on-Silicon Photonic Integrated Circuits for the 5 µm Wavelength Range

Fotonische geïntegreerde circuits op basis van germanium-op-silicium voor een golflengtegebied rond 5 µm

Aditya Singh Malik

Promotor: prof. dr. ir. G. Roelkens
Proefschrift ingediend tot het behalen van de graad van
Doctor in de Ingenieurswetenschappen: Fotonica

Vakgroep Informatietechnologie
Voorzitter: prof. dr. ir. D. De Zutter
Faculteit Ingenieurswetenschappen en Architectuur
Academiejaar 2014 - 2015

UNIVERSITEIT GENT

ISBN 978-90-8578-781-5
NUR 926, 959
Wettelijk depot: D/2015/10.500/25

Universiteit Gent
Faculteit Ingenieurswetenschappen en Architectuur
Vakgroep Informatietechnologie

Promotoren:

Prof. Dr. Ir. Gunther Roelkens

Examencommissie:

Prof. Dr. Ir. Hendrik Van Landeghem (voorzitter)	Universiteit Gent, RVL
Prof. Dr. Ir. Gunther Roelkens	Universiteit Gent, INTEC
Prof. Dr. Ir. Roel Baets	Universiteit Gent, INTEC
Prof. Dr. Ir. Dries Van Thourhout	Universiteit Gent, INTEC
Prof. Dr. Ir. Peter Bienstman	Universiteit Gent, INTEC
Dr. Goran Mashanovich	University of Southampton, ORC
Dr. Ir. Joris Van Campenhout	IMEC
Prof. Dr. Ir. Kristiaan Neyts	Universiteit Gent, ELIS

Universiteit Gent
Faculteit Ingenieurswetenschappen en Architectuur

Vakgroep Informatietechnologie
Sint-Pietersnieuwstraat 41, B-9000 Gent, België

Tel.: +32-9-264.33.41
Fax.: +32-9-264.35.93

Acknowledgement

Tiger likes to hunt
Bird likes to fly
Man likes to ask himself why, why why.

These lines by Kurt Vonnegut describe why a boy from a small village in India would cross lands and seas to work for four years to get a doctorate. I would begin by thanking my parent for supporting all my endeavors. They never let me feel the need for anything. This journey actually started in 2005 when I moved to New Delhi to pursue my undergraduate studies in Ramjas College, University of Delhi. Ah, that was the time! Full of roaming around Delhi in its new metro and eating out at every restaurant. Shekhar, Mukta, Avantika thak you guys for the memorable years and all the good times. We are the 'Mahasharifs'! Reader, if you ever visit Delhi, do ask for a few tips of where to hang out. I also met my soul-mate in DU but that story is for some other time. In 2008 I started my masters in IIT Delhi which in beginning appeared to be a bit strange kind of place because there were always surprise tests besides the regular ones but soon I got the hang of that system as well and managed to get funds to do an internship in FU Berlin. I would say that I understood what research is, working in the lab of Prof. Bittl and decided that this is something I would like to do after masters. Thanks a lot to Jana, Marc, Axel, Christian for the good time and some nice advice.

So enough of the days before I moved to Ghent. I must confess that I was a bit skeptical of this country when I first arrived at the airport. To begin with the train was nothing like DB Bahn ICEs and secondly it was a day when trains were running **very** slow. I was under the impression that all of Europe is just like Germany and everything would go very efficiently. How wrong was I at that time! Many thanks to Rajesh and Sukumar for the help in those initial days.

On a professional note, I consider myself to be lucky to have Gunther as my supervisor. He has been very supportive through out the past years. In the beginning when I was trying to build a setup and optimize the etching etc. in the cleanroom, he would always come up with valuable and more importantly practical suggestions which made working in the lab quite fun. The amount of novel

ideas that he has makes me think I would be able to do a good job in future if I can get 1% of those. Life in the lab would have been very difficult if the mid-ir team wasn't there for help. Thanks to Bart for showing me the tricks of aligning a free space laser in a fiber, Francois for the getting ultrasonic cleaver from ULB and Alban for all the work with the FTIR. Thanks is also due to Muneeb for his assistance in all the designs and numerous discussions about the components. I learn something new each time from our discussions. Chen, Nannicha, Utsav - thanks a lot guys for accommodating my request of lending out an instrument or two. Thanks to the whole team for providing remarks in the mid-ir meetings (although I miss that non-linear guys are not with us) and for the delicious cakes we used to have. Maybe its time that we restart the tradition of having cake (brought by the person who has his/her birthday most close) in the mid-ir meeting.
One thing that I like most about our group is that since there are so many of us, there is always someone who can help you with an issue. I would like to thank many people starting with Shibnath who helped me in the beginning to master the tricks of Ipkiss. Thanks are also due to Sarvagya for all the help in Comsol. In the cleanroom, Steven has contributed a lot in doing all the processes. Everything I know about processing has been taught to me by Steven. I would like to thank Liesbet for taking all the SEM pictures, many of them on a short notice and for performing the drilling of the free standing heaters. Peter Guns also has my thanks for making the customized parts, again on short notice. I met a lot of people- Cristina, Elewout, Wout, Marie, Kristof, Tom, Thijs, Eva, Sam, Pauline, Yannick, Martijn, Martin (I pronounce both as Mar-tin), Khai, Stevan, Shankar, Amit, Andrea, Andreas, Sarah, Diedrik, Linghua, Zhechao, Yanlu. All the professors in the group, Roel, Dries, Peter, Wim, Geert, Nicolas - thanks for creating a creative atmosphere in the group. It has been great to know you all. Also, the entire microphotonics team, especially Thomas and Herbert for taking the 'Thin Films' lab with me, deserves a special mention. Having lunch with all the people - Michael, Shibnath, Ananth, Utsav, Sarvagya,Alfonso, Jan Willem ,Jesper, Ashim, Andrew, Daan, Frederic, Pijush, Antonio, Bendix, and discussing about various topics of the world, helped me clear my head. Although now a days I get to eat very nice food at home so I have started to skip these brain storming sessions but feel free to discuss any issue anytime. Recently I have enjoyed working with Anton a lot and I hope that our joint ventures in mid-ir gas sensing would produce good results soon.
There were quite some activities outside the office as well. I would like to thank Shibnath for introducing me to gym and all the tips. Hopefully I can start the Kris Gethin program soon. Alfonso - thank you as well for the company. It would be nice to have you back in escape fitness. Thanks to the Indian community in Ghent - Ark, Sameer, Abhishek, Sandeep, Manan, Kartik, Ashok, Ana-

nth for the cricket matches. Ananth and Sarvagya also deserves a special thanks for all those eat together/outside sessions. Sarvagya we should start frequenting Starbucks again for those Sunday afternoon coffee breaks (although now you live so far that asking for it is like asking you to come to the gym). Michael, thanks for all the philosophical discussions and telling me and Shibnath about the famous fritches place. I hope you attain 'moksha'! Thanks to Bendix and Floriane for hosting me many times at their place on various occasions and also for the muffins/cakes. Hope you guys always find joy with Kiya and Meline, Also, thanks to Ananth, Kamal, Sarvagya, Utsav to all the trips to Antwerp for Bollywood movies. Recently this group has expanded to create the 'Happy New year' Group. All the members of this prestigious (where admission is by invitation only) group - Manan, Namrata, Saurav, Sulakshna, Ananth, Kamal, Kirti deserve a mention for the dinner/surprise birthday parties we are having now a days.

My soul-mate Kirti has most of my thanks for all the love and happiness. We have come a long way since those lectures of 'Modern Chemistry' and have been through many ups and downs. You have always been supportive of me and I couldn't stress the point that the four years when we lived apart would have been much more difficult if you weren't so understanding. You have become the synonym of happiness for me. May we always rejoice in our love for each other.

So finally the thesis has come to an end. I would sometimes miss being a PhD student and I hope that the hunger to learn always stays with me. Finally, I would like to sign off with another one of Vonnegut's and great Harivansh Rai Bacchan's lines.

Tiger got to rest
Bird got to land
Man got to tell himself that he understand.

तू न थकेगा कभी, तू न थमेगा कभी,
तू न मुड़ेगा कभी |
कर शपथ, कर शपथ, कर शपथ |
अग्निपथ अग्निपथ अग्निपथ ||
- बच्चन

Ghent, Oct 2010 - March 2015
Aditya Malik

Table of Contents

List of Figures

List of Tables

List of Acronyms

A

AWG	Arrayed Waveguide Grating
Au	Gold

B

BOX	Buried Oxide

C

CMOS	Complementary Metal-Oxide-Semiconductor
Cr	Chromium

D

DBR	Distributed Bragg reflector

F

FP	Fabry-Perot

FPR	Free Propagation Region
FSR	Free Spectral Range
FDTD	Finite Difference Time Domain

G

Ge	Germanium

H

HF	Hydrofluoric acid

I

ICL	Interband Cascade Laser

K

K	Kelvin

M

MMI	Multi Mode Interferometer
MZI	Mach-Zehnder interferometer

P

PA	Photo Acoustic

PCG	Planer Concave Grating
PIC	Photonic Integrated Circuit

Q

QCL	Quantum Cascade Laser

S

SEM	Scanning Electron Microscope
Si	Silicon
SiN	Silicon Nitride
SiO	Silicon Oxide
SK	Stranski-Krastanov
SNR	Signal to noise
SOI	Silicon on Insulator
SOS	Silicon on Sapphire

T

TE	Transverse Electric
Ti	Titanium
TM	Transverse Magnetic

W

WDM	Wavelength Division Multiplexing

Nederlandstalige samenvatting

Het mid-infrarood golflengtebereik is zeer interessant voor spectroscopische toepassingen. Dit is te danken aan (a) een grotere absorptiedoorsnede van moleculen in vergelijking tot het nabij-infrarood golflengtebereik en (b) het specifieke vingerafdrukspectrum van individuele moleculen. Spectroscopische systemen bestaan uit een lichtbron, een interactiepad en een detector. Met de uitvinding van de quantum cascade lasers (QCLs) en interband cascade lasers (ICLs) werd het mogelijk om een mid-infrarood lichtbron te maken op basis van halfgeleiderchips. De implementatie van deze chips om een breed afstembare lichtbron te maken in het mid-infrarood vergt nog steeds het gebruik van een bewegende tralie of 'grating' waardoor de complete verpakking van dit toestel vrij groot uitvalt.
Fotonische integratie van licht-emitterende III-V epitaxiale materialen met passieve PICs heeft het mogelijk gemaakt om draagbare lasermodules te maken in het nabij-infrarood golflengtebereik. Omwille van massaproductiecapaciteiten en de mogelijkheid om een groot aantal golfgeleidercircuits op een kleine oppervlakte te integreren is silicium-op-isolator (SOI) het materiaalplatform bij uitstek geworden voor het nabij-infrarood golflengtebereik. Men zou dus een gelijkaardig CMOS-compatibel golfgeleiderplatform willen vinden voor het mid-infrarood golflengtebereik met hetzelfde voordeel van lage productiekost. Dit golfgeleiderplatform kan enerzijds passieve golflengteselectieve componenten bevatten die terugkoppelen naar de mid-infrarode actieve laser chips. Anderzijds kan dit platform golflengtefilters bevatten die dienst doen als spectrometers in toekomstige lab-on-a-chip spectroscopische systemen.

Platform voor Passieve Golfgeleiders

De standaard SOI-golfgeleidercircuits die gebruikt worden voor het nabij-infrarood golflengtebereik bestaan uit een toplaag van silicium met een dikte tussen 220 nm en 400 nm en een hieronder begraven 2 μm dikke oxidelaag (BOX). De eerste uitdaging om SOI-golfgeleiders te gebruiken in het mid-infrarood golflengtebereik bestaat erin dat de BOX laag sterk begint te absorbe-

ren voor golflengtes vanaf 4μm. Men moet dus andere beschikbare materialen onderzoeken die transparant zijn in het mid-infrarood golflengtebereik. Dit platform moet naast transparantie nog aan twee andere voorwaarden voldoen. Ten eerste moet de fabricageprocedure voldoende eenvoudig zijn en geen kritische stappen bevatten die tot falen kunnen leiden. Ten tweede moet het mogelijk zijn om de golfgeleiders te fabriceren in een CMOS compatibele productielijn om de totale productiekosten minimaal te houden, wat te danken is aan de massaproductiecapabiliteit.
In de laatste jaren werden verschillende componenten op een reeks van golfgeleiderplatformen gedemonstreerd. Op SOI werden componenten zoals AWGs, PCGs, MZIs, ring resonatoren, roosterkoppelaars, thermo-optische faseverschuivers en dergelijke gedemonstreerd tot op een golflengte van 4 μm. Om deze componenten te gebruiken voor golflengtes langer dan 4 μm kan men proberen om de BOX laag van SOI golfgeleiders te verwijderen. Deze aanpak heeft echter een serieuze tekortkoming omdat de vrij-hangende golfgeleiders mechanisch minder robust zijn.. Verder is het niet mogelijk om brede, plaatvormige componenten te maken. Er is onderzoek geweest naar andere, waardige alternatieven voor dit platform. Silicium-op-saffier is een mogelijkheid, maar die is jammer genoeg enkel transparant tot 5μm. Silicium nitride of golfgeleider platformen op basis van chalcogeniden zijn ofwel niet compatibel met CMOS processen of hebben uiterst complexe fabricageprocedures met kritische stappen die vaak tot falen leiden tijdens de productie. Germanium-op-silicium daarentegen, voldoet aan al de voorwaarden om een geschikt golfgeleiderplatform te zijn voor het mid-infrarood golflengtebereik omdat het een veel groter transparantiebereik heeft, een rechttoe rechtaan fabricageschema heeft en volledig CMOS compatibel is. Daarom hebben we gekozen om met germanium-op-silicium te werken voor ons golfgeleiderplatform.

Fabricageschema

Het fabricageschema voor germanium-op-silicium golfgeleiders is schematisch voorgesteld in Fig. 1.
De eerste stap is de epitaxiale groei van een dunne germanium film op een (100) silicium substraat (in imec). De golfgeleiderpatronen zijn overgebracht met i-line contact lithografie in metaal (Ti-Cr) door middel van een lift-off proces op de germanium laag. Deze metalen golfgeleiderpatronen worden vervolgens droog geëtst in een RIE systeem met CF_4:O_2 plasma en het gedefinieerd patroon wordt daarbij overgezet in germanium. Het metaal wordt achteraf verwijderd in een waterstoffluoride oplossing (HF). Met deze plasmatechniek verkrijgt men golfgeleiders met ruwe zijwanden die niet perfect vertikaal zijn zoals men kan

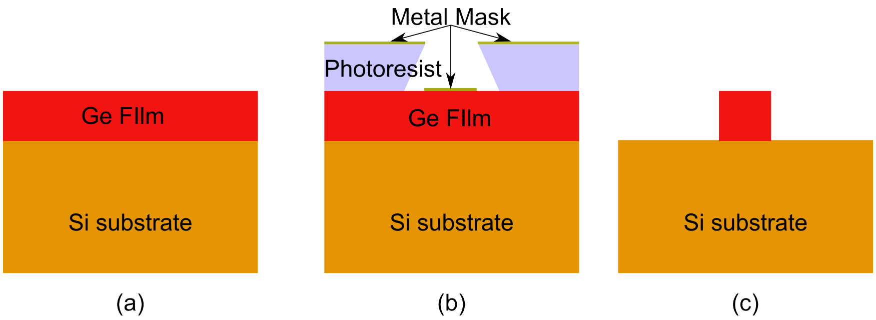

Figuur 1: *Fabricageschema voor Ge-op-Si geïntegreerde fotonische circuits. (a) Epitaxiale groei van germanium film op een Si (100) 200 mm substraat, (b) definitie van metalen masker met i-line contact lithografie en lift-off en (c) droog etsen van germanium film en het verwijderen van het metalen masker.*

zien in Fig. 2, maar we hebben ondervonden dat dit de eindkwaliteit van de componenten niet sterk ondermijnt.

Gerealiseerde optische functies

Om te beginnen hebben we aangetoond dat de golfgeleiderverliezen in de buurt van 3-4 dB/cm lagen voor volledig (2 μm dik) en partieel (1.5 μm dik) geëtste golfgeleiders voor TE en TM polarisaties. We hebben golflengte-(de)multiplexers gebaseerd op MZIs, AWGs en PCGs ontworpen en experimenteel gerealiseerd. De MZIs waren gemaakt met splitsers en samenvoegers op basis van MMIs met een gemeten insertieverlies van -0.5 dB en een extinctie-verhouding van -20 dB. Een 5×200 GHz AWG is gerealiseerd met een insertieverlies van -2.5 (-3.1) dB voor TE (TM) polarisatie en de overspraak 20 dB (16 dB). Een PCG met zes kanalen en een kanaalspatiëring van 25 nm is gerealiseerd met verschillende roosters (vlak facet, totale interne reflectie facet, DBR facet) en voor het DBR facet was het insertieverlies -4.9 dB (-4.2 dB) voor TE (TM) polarisatie en de overspraak 22 dB (23 dB). Een microscoopafbeelding van de gefabriceerde AWG en PCG is getoond in Fig. 3.
We hebben ook een thermo-optische faseverschuiver gerealiseerd die het mogelijk maakt om het spectrum van de golflengtefilters af te stellen. Een gewone faseverschuiver gemaakt met het Ge-op-Si platform bleek zeer inefficiënt te zijn met een verbruik van 700 mW voor een 2π fase verschuiving. Om de efficiëntie te verhogen hebben wij de structuur ondergeëtst met de FIB en dit resulteerde in een veel lager verbruik van 80 mW. Om het verbruik te verminderen op een elegantere manier introduceren we een thermische isolator in het warmtepad

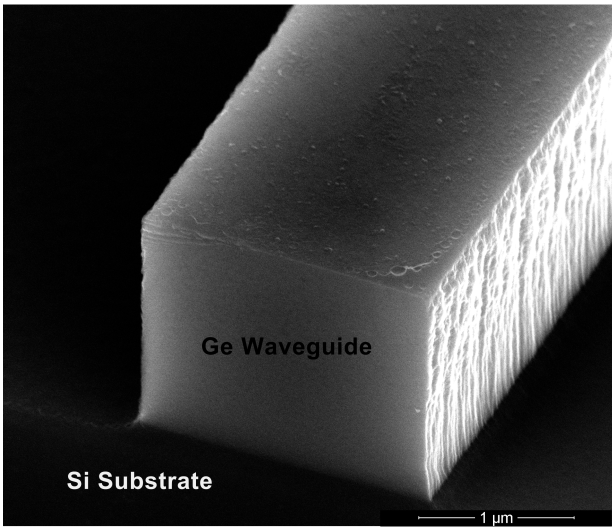

Figuur 2: *Gekliefd facet van een Ge-op-Si golfgeleider, geëtst in een CF_4:O_2 plasma in 40:10 verhouding met een vermogen van 600 W en een druk van 10 mtorr. Het metalen masker was verwijderd met HF.*

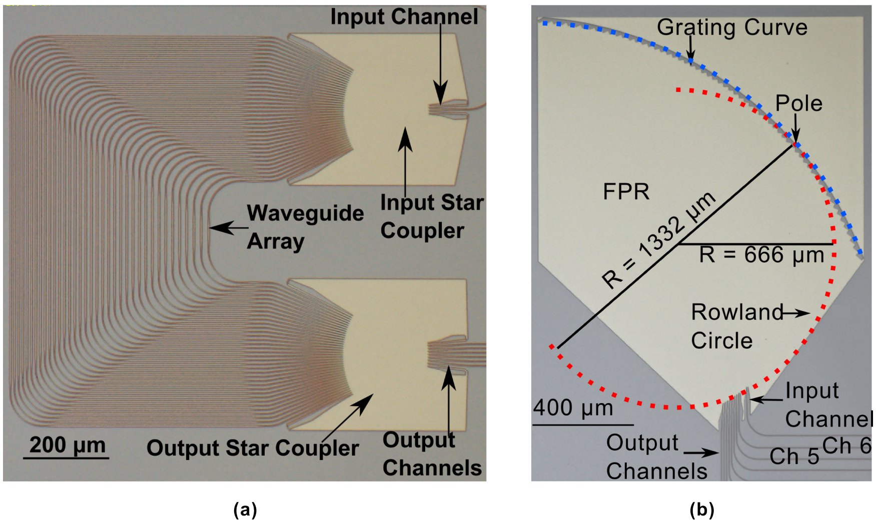

Figuur 3: *Microscoop afbeelding van (a) gefabriceerde 5×200 GHz AWG en (b) een zes kanalen PCG met kanaalspatiëring van 25 nm*

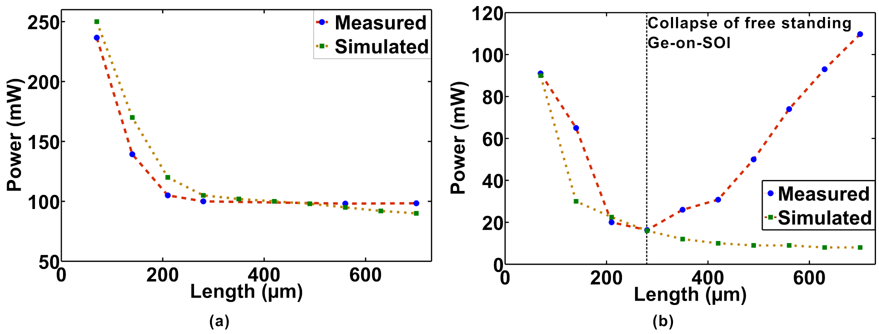

Figuur 4: *Verbruikt vermogen in functie van de lengte van het warmte-element voor een Ge-op-SOI thermo-optische faseverschuiver (a) met onderliggend oxide en (b) nadat dit ondergeëtst werd.*

van de component. Om dit te bereiken hebben we huisgemaakte germaniumlagen epitaxiaal gegroeid op SOI wafers. De golfgeleiderverliezen zijn hierdoor wat hoger (7 dB/cm), wat betekent dat een verdere optimalisatie van het groeiproces nodig is maar het benodigd vermogen voor een 2 π fase verschuiving is nu 105 mW en dit werd verder verlaagd tot 16 mW door de onderliggend oxidelaag (BOX) te verwijderen. Het verloop van het benodigd vermogen in functie van de lengte voor een Ge-op-SOI thermo-optische faseverschuiver is getoond in Fig. 4 (a) en (b) respectievelijk met en zonder het verwijderen van het onderliggend silicium oxide.

Conclusies

Uit de bovenstaande discussie kan men afleiden dat germanium-op-silicium een beloftevol kandidaat blijkt te zijn om de dezelfde rol te vervullen in het mid-infrarood golflengtebereik zoals SOI in het nabij-infrarood golflengtebereik. De fabricageprocedure is rechttoe rechtaan en kan geïmplementeerd worden in een CMOS productielijn. Het gebruik van standaard processen in een CMOS lijn kan zeker de performantie van passieve golfgeleider filters verbeteren en potentieel ook de golfgeleiderverliezen alsnog verbeteren. Dit zou ons ook toelaten om componenten te realiseren die uiterst smalle afmetingen nodig hebben zoals ring resonatoren die niet optimaal ontworpen konden worden in deze thesis omwille van de beperkingen van de beschikbare lithografie. Op basis van deze componenten zou men dan draagbare lasermodules of complete spectroscopische systemen kunnen realiseren die werken in het mid-infrarood golflengtebereik en die geïntegreerd zijn op germanium-op-silicium golfgeleidercircuits.

English summary

The mid-infrared wavelength range is of interest for spectroscopic sensing applications. This interest is related to (a) a large absorption cross section of molecules compared to the near-infrared wavelength range and (b) the specific fingerprint absorption spectrum of individual molecules. Spectroscopic systems contain a light source, an interaction path and a detector. Light generation in the mid-infrared wavelength range using semiconductor chips was made possible by the invention of quantum cascade laser (QCLs) and interband cascade lasers (ICLs). The implementation of these chips to realize widely tunable sources however still uses a mechanism involving a moving grating, which makes the complete package bulky.
Photonic integration has enabled the realization of hand-held laser modules in the near-infrared wavelength range as the light emitting III-V epitaxial materials can be integrated with passive PICs which provide the required feedback. Because of their mass-manufacturability and the ability to pack a large amount of waveguide circuits in small space, silicon-on-insulator (SOI) has now become a material platform of choice in the near-infrared wavelength range. One can therefore envisage the use of a CMOS compatible waveguide platform for the mid-infrared wavelength range which would have a similarly lower production cost. This waveguide platform could either contain the passive wavelength selective devices which provide feedback to the mid-infrared gain chips or they could contain wavelength filters to act as spectrometers which pave the way for a hand-held lab-on-a-chip spectroscopic system.

Passive Waveguide Platform

The standard SOI waveguide circuits used for the near-infrared wavelength range consist of a top silicon layer of thickness ranging from 220 nm to 400 nm and a 2 μm thick buried oxide (BOX). The first challenge in using the SOI waveguide platform for the mid-infrared wavelength range is that the BOX layer starts to absorb heavily after 4 μm wavelength. One then needs to investigate available materials which are transparent in the mid-infrared wavelength range.

Apart from transparency, there are two key requirements which the waveguide platform needs to meet. Firstly, the fabrication scheme of the waveguide circuits should be straight-forward and shouldn't contain critical failure steps. Secondly, it should be possible to fabricate the waveguide circuits in a CMOS pilot line in order to keep the overall cost of production to be minimal because of the mass-manufacturing capability.
In recent years, there have been demonstrations of various devices on a range of waveguide platforms. On SOI, devices such as AWGs, PCGs, MZIs, ring resonators, grating couplers, thermo-optic phase shifters etc. have been demonstrated till a wavelength of 4 μm. To extend the operation beyond 4 μm, one can think about removing the BOX from the SOI waveguides. This approach however has a serious drawback as the free standing waveguides are prone to collapsing and moreover its not possible to realize wide slab based devices. There has been work done on various other waveguide platforms like silicon-on-sapphire, which is transparent only up to 5 μm and silicon nitride or chalcogenide based waveguide platforms which either have fabrication schemes containing critical failure steps or are not CMOS compatible. Germanium-on-silicon fits all the requirements for a suitable waveguide platform for the mid-infrared wavelength range since it has a very wide transparency window, a straight forward fabrication scheme and is completely CMOS compatible. We therefore chose germanium-on-silicon as our waveguide platform of choice.

Fabrication Scheme

The fabrication scheme of germanium-on-silicon waveguide circuits is detailed in Fig. 5.

The first step is the epitaxial growth of a germanium film on a (100) silicon substrate (in imec). The waveguide circuits are transferred using i-line contact lithography and metal (Ti-Cr) liftoff on the germanium film which is subsequently dry etched in a RIE system using CF_4:O_2 plasma. Although this particular fabrication scheme results in rough waveguide side walls which are not perfectly vertical as shown in Fig. 6, we observed that it doesn't severely degradedevice performance.

Realized devices

To begin with, we demonstrated that the waveguide losses are in the range of 3-4 dB/cm for fully (2 μm layer thickness) and partially (1.5 μm etch depth) etched waveguides for TE and TM polarization. We designed and experimentally demonstrated wavelength (de)multiplexers based on MZIs, AWGs and

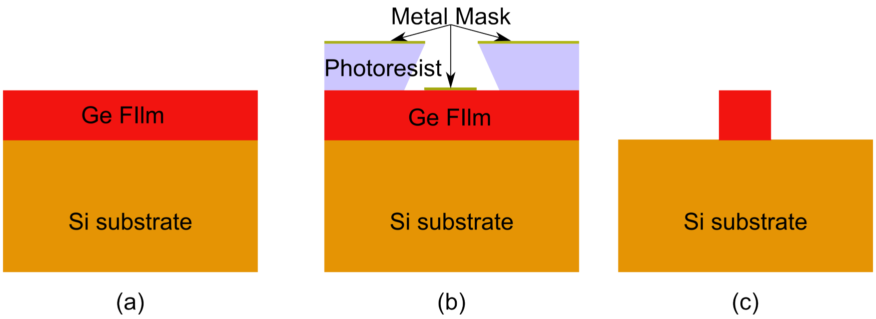

Figure 5: *Fabrication flow for Ge-on-Si integrated photonic circuits. (a) Epitaxial growth of germanium film on a Si (100) 200 mm substrate, (b) metal mask definition using i-line contact lithography and lift-off and (c) dry etching of germanium film and removal of metal mask.*

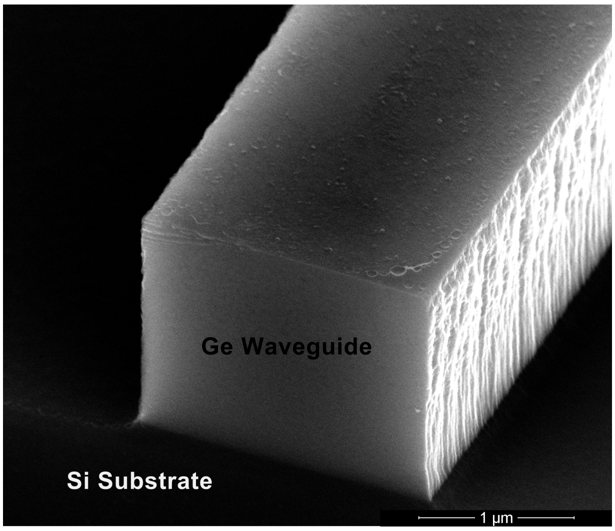

Figure 6: *Cleaved facet of a Ge-on-Si waveguide etched in a CF_4:O_2 plasma in 40:10 ratio at a power of 600 W and pressure 10 mtorr. The metal mask has been removed using HF.*

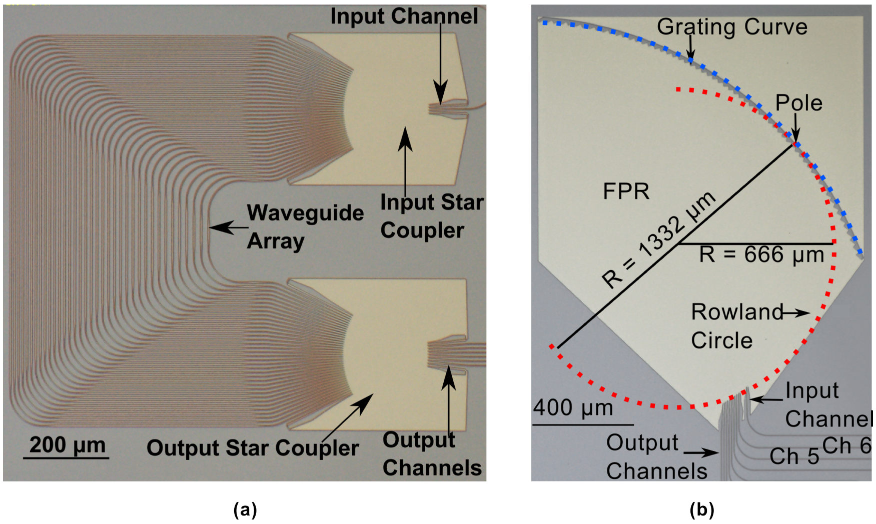

Figure 7: *Microscopic image of (a) fabricated 5×200 GHz AWG and (b) six channel PCG with 25 nm channel spacing.*

PCGs. The MZIs were realized using MMIs as splitters and combiners and showed an insertion loss of -0.5 dB and extinction ratio of -20 dB. A 5×200 GHz AWG was realized with an insertion loss of -2.5 (-3.1) dB for TE (TM) polarization and cross talk of 20 dB (16 dB). A six channel PCG with 25 nm channel spacing was realized using various gratings (flat facet, total internal reflection facet, DBR facet) and it was found that for a DBR facet, the insertion loss is -4.9 dB (-4.2 dB) for TE (TM) polarization and the cross talk is 22 dB (23 dB). A microscopic image of the fabricated AWG and PCG is shown in Fig. 7.

We also realized thermo-optic phase shifters which would make spectrum tuning of the wavelength filters possible. It was found that a regular phase shifter realized on germanium-on-silicon waveguides is very inefficient resulting in 700 mW power consumption for a 2π phase shift. To increase the efficiency, we performed an undercut using FIB which lowered the power consumption to 80 mW. There is another elegant way of lowering the power consumption by deliberately introducing a thermal insulator in the heat path. To achieve this, we performed epitaxial growth of germanium films on a SOI wafer. Although the waveguide losses of such waveguides were found to be higher (7 dB/cm), which means further optimization is needed on growth, the tuning power was found to be 105 mW for a $2\,\pi$ phase shift which was lowered to 16 mW for a phase shifter where the underlying oxide was removed. The behavior of tuning power as a function of length for a Ge-on-SOI thermo-optic phase shifter is shown in Fig. 8 (a) and (b) respectively with and without removal of the underlying silicon oxide.

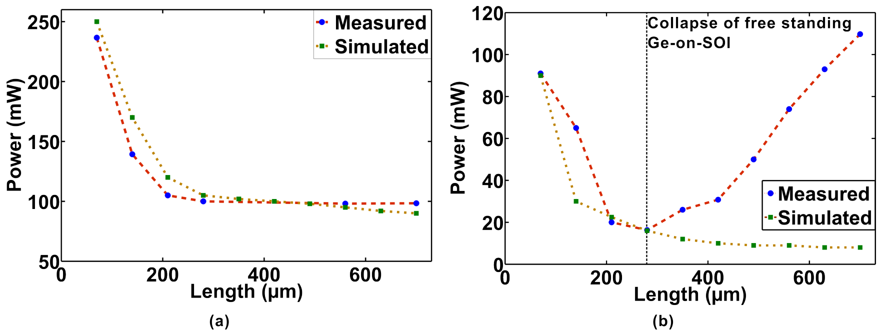

Figure 8: *Tuning power as a function of heater length for a Ge-on-SOI thermo-optic phase shifter (a) without undercut and (b) with undercut.*

Conclusion

One can deduct from the above discussion that germanium-on-silicon shows promise to play the same role in the mid-infrared wavelength range as SOI has played for the near-infrared wavelength range. The fabrication process is straight forward and can be transferred to a CMOS pilot line. Use of standard tools in a CMOS pilot line could potentially also improve waveguide loss and definitely improve the performance of passive waveguide filters. It would also allow the realization of devices which require a narrow feature size e.g. ring resonators, which couldn't be designed optimally in the course of this thesis because of lithographic limitations. Based on these devices one can then also envisage the realization of hand-held laser modules or complete spectroscopic systems operating in the mid-infrared wavelength range, which are integrated in germanium-on-silicon waveguide circuits.

1

Introduction

“The secret of getting ahead is getting started. ”

– Mark Twain

1.1 Mid-infrared Spectroscopy

Spectroscopy is the study of the interaction of electromagnetic waves with matter. There are different kinds of spectroscopic techniques associated with various parts of the electromagnetic spectrum as depicted in Fig. 1.1. One of the most interesting parts of the electromagnetic spectrum is the infrared region, and the associated vibrational spectroscopy. The vibration of atoms about their mean positions in a molecule can give rise to a change in the dipole moment, which is similar to the fluctuations in the electric field of incoming electromagnetic radiation. Thus an interaction can occur and energy can be absorbed or emitted by the molecule. This gives rise to a specific absorption/emission spectrum for each molecule. The vibration spectrum of each molecule is unique and hence serves as a fingerprint to identify it [1].

The infrared region is further divided in near (1-3 μm), mid (3-12 μm) and far (12-100 μm) infrared regions. The mid-infrared region is of particular interest because many atmospheric gases and liquids have fingerprint spectra in this wavelength range. This is shown in Fig. 1.2 which shows the absorption cross section in logarithmic units of various gases in the atmosphere as a function of wavelength. Also, it can be observed that the strength of the absorption lines increases exponentially as one migrates from the near-infrared to the mid-infrared wavelength range.

To demonstrate the fingerprinting nature of the absorption spectrum, the absorption strength of two isotopes of CO_2, namely $C^{12}O_2$ and $C^{13}O_2$, is shown in Fig. 1.3. It can be seen that although the shape of the spectrum of both molecules is quite identical, the spectrum is substantially shifted in wavelength.

Apart from atmospheric gases, many liquids which one would like to detect have a characteristic absorption spectrum in the mid-infrared. This is shown in the FTIR spectrum of cocaine and glucose in Fig. 1.4(a) and (b) respectively. We list some strong transitions in the mid-infrared wavelength range featuring some interesting functional groups in table 1.1.

It can be seen from table 1.1 that each functional group has characteristic absorption bands associated with it. These absorption bands differ in width (e.g. the =C-H stretch of the alkene group has a narrow feature while the C-O stretch of the alcohol group has a very wide feature). The same chemical bonds also can show a different fingerprint depending on which group they are associated with (e.g. the C-H stretch has a very sharp feature at 3.03 μm for alkynes while it has a broader feature between 3.33 and 3.51 μm for alkanes and 3.32 and 3.51 μm for aromatics).
It's clear from this discussion that mid-infrared spectroscopy allows not only the detection of specific molecules but also allows to clearly distinguish between

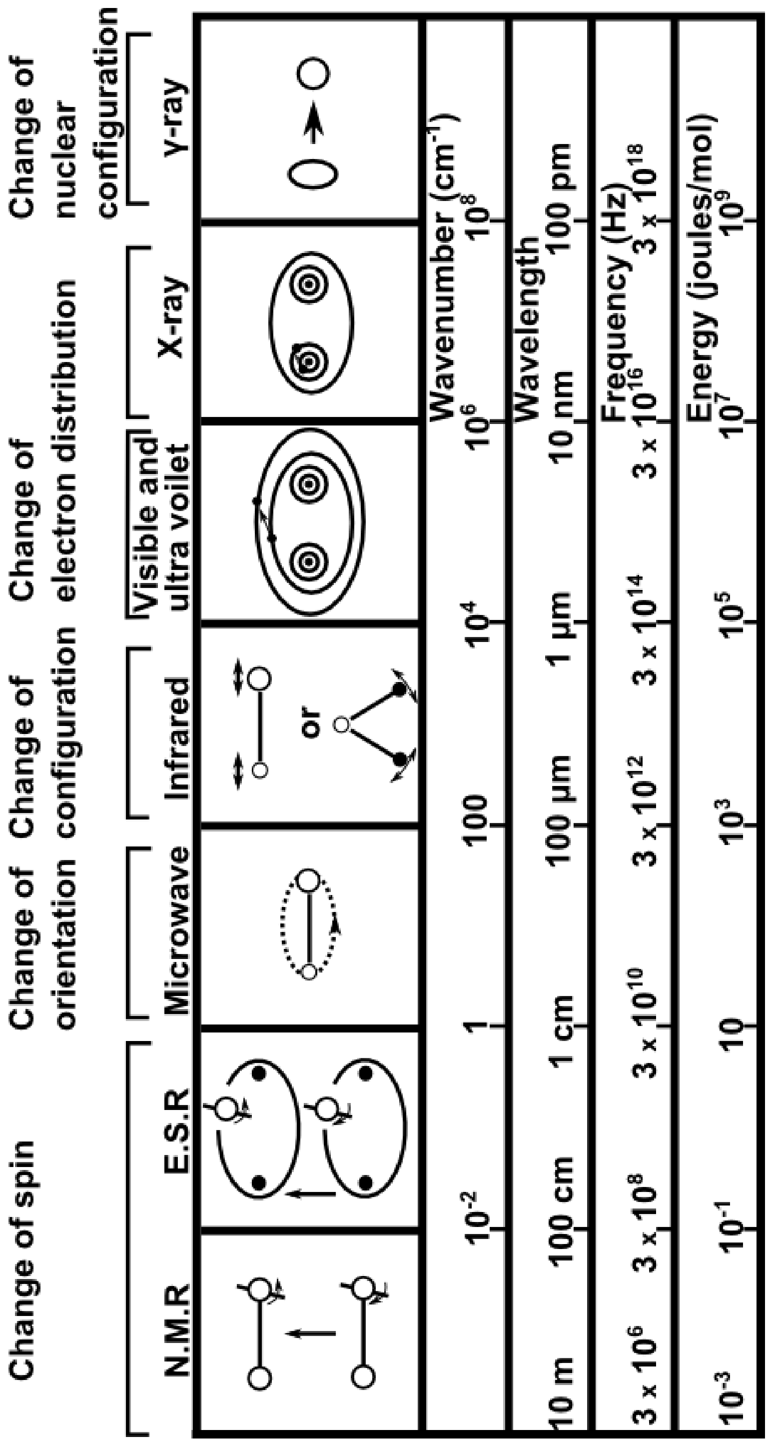

Figure 1.1: *The electromagnetic spectrum and the spectroscopic methods associated with different regions (from [1]).*

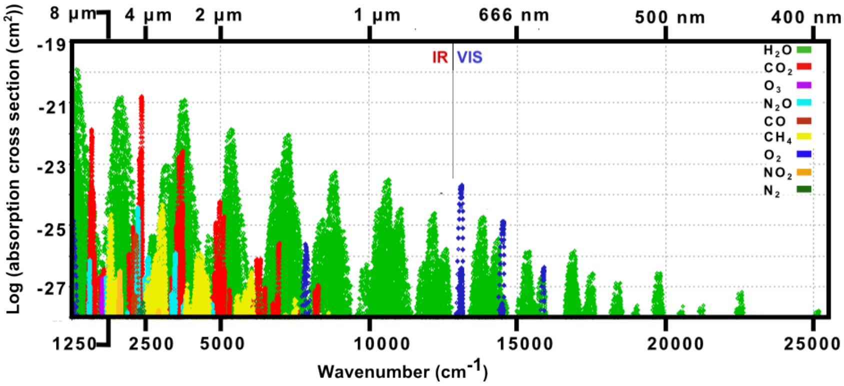

Figure 1.2: *Absorption cross section (in cm^2) of atmospheric gases (in logarithmic scale) as a function of wavelength (from [2]).*

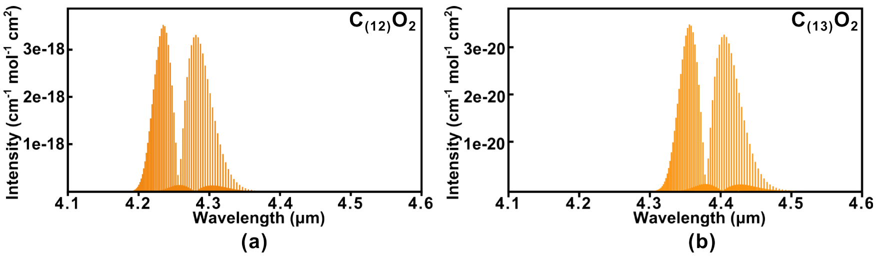

Figure 1.3: *Absorption spectrum of the two isotopes of CO_2 (from [3]).*

them using analytic sensing.

1.1.1 Mid-infrared light generation

Any spectroscopic system would need a light source to produce the electromagnetic wave at the desired wavelength. Lasers are coherent emitters of electromagnetic radiation and are used widely in various applications such as datacom, telecom, data storage etc.. A laser consists of a gain medium where population inversion is achieved that is sandwiched between mirrors which bounce light back and forth in an optical cavity. Traditionally, the gain medium consisted of crystals such as ruby, Nd-YAG or gas mediums such as He-Ne, Ar or CO_2. Advances in the semiconductor field however quickly introduced the III-V semiconductor gain media where light generation is realized by transitions of electrons from the conduction to the valence band. The principle of operation of these lasers is quite straight forward. An energy gap is created between the conduction and valence band and the electrons are excited from the valence

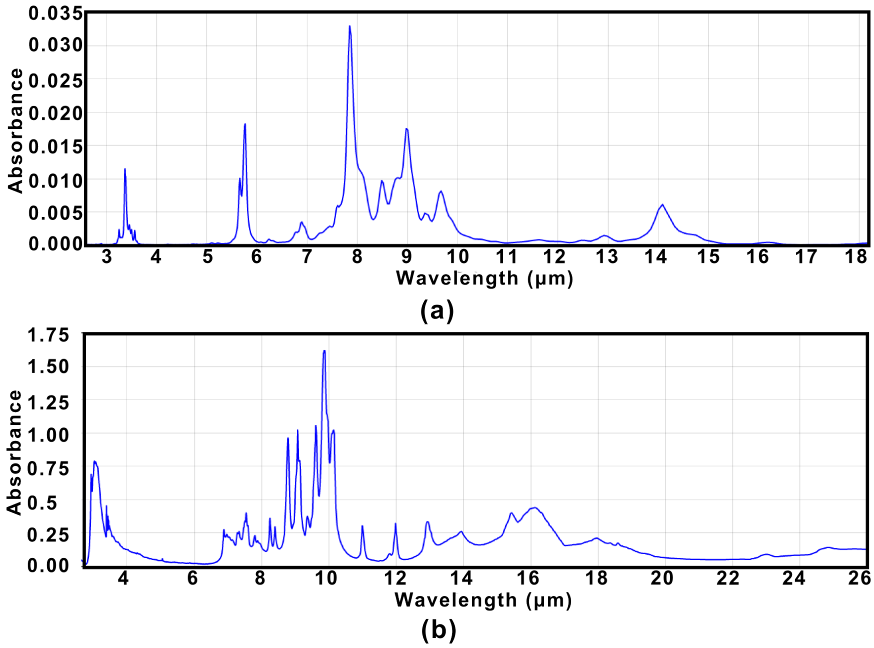

Figure 1.4: *FTIR absorption spectrum of (a) Cocaine and (b) Glucose (from [4]).*

band to conduction band. The transition of the electrons back in the valence band creates a photon as shown schematically in Fig. 1.5. The energy (and therefore the wavelength) of this created photon is determined by the bandgap. This method is utilized to generate light in the visible or near-infrared (up to 3 μm)wavelength region from InP & GaSb-based III-V materials. However one runs into several complications as the desired emission wavelength is increased. The performance of such diode lasers quickly degrades, mostly related to strong Auger recombination in narrow bandgap materials, as one increases the emission wavelength. Thus for many decades light generation in the mid-infrared wavelengths was done using bulky lasers (liquid nitrogen cooled) or incoherent broadband light sources such as globars and a novel idea was needed which allowed one to efficiently generate mid-infrared light on a semiconductor chip.

The solution to this can be found in one of the most basic problems of quantum mechanics - the particle in a box. It is known that the number of energy levels inside a potential well are defined by it's width. One could then think about generating light inside an energy band (conduction band or valence band) itself if its thickness could be adjusted such that the energy levels would split. If an electron relaxes from a higher energy level to the lower energy level within the band,

Functional Group	**Characteristic Absorption Band (cm^{-1})**	**Characteristic Absorption Band (μm)**
Alcohol		
O-H	3200-3600	2.77-3.125
O-H	3500-3799	2.63-2.85
C-O	1050-1150	8.69-9.52
Alkane		
C-H	2850-3000	3.33-3.51
Alkene		
=C-H	3010-3100	3.22-3.32
Alkyl Halide		
C-F	1000-1400	7.14-10
C-Cl	600-800	12.5-16.6
Alkyne		
C-H	3300	3.03
Amine		
N-H	1600	6.25
Aromatic		
C-H	3000-3100	3.32-3.51
Carbonyl		
C=O	1670-1820	5.49-5.98
Ether		
C-O	1070-1150	9.34-9.52
Nitro		
N-O	1515-1560 & 1345-1385	6.6-6.41 & 7.22-7.43

Table 1.1: *Table listing the characteristic absorption bands of various functional groups (from [5]).*

it would create a photon. The first idea of achieving light generation by these intersubband transitions was proposed by Kazarinov and Suris in 1971 utilizing a photon-assisted tunneling transition [7]. This idea resulted in the demonstration of quantum cascade lasers. In recent years another type of semiconductor mid-infrared laser also started gaining attention; the interband cascade laser. In the following section we will briefly introduce these laser types.

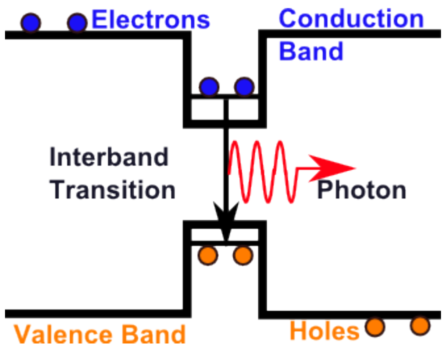

Figure 1.5: Schematic diagram explaining the working principle of a traditional semiconductor laser relying on band-to-band transitions [6].

1.1.1.1 Quantum Cascade Lasers

The idea of light generation by intersubband transitions was first verified by Faist *et. al.* in 1994 in Bell labs where they demonstrated the generation of coherent 4.3 μm radiation at cryogenic temperatures using intersubband transitions and called the device a Quantum Cascade Laser (QCL) [8]. The cascading principle of the intersubband transitions is shown in Fig. 1.6. A QCL consists of an quantum well active region and an n-type electron injector region typically grown using molecular beam epitaxy (MBE). The injector region consists of several wells and barriers which create minibands separated by minigaps. If an electrical bias is applied, the electrons are injected from the ground state of a miniband to the uppermost level of the active region (denoted by level 3). Stimulated emission can therefore be obtained by the intersubband transition from level 3 to level 2. The electron then decays via phonon scattering to the ground level (denoted by level 1) of the active region from where it enters the miniband in the next stage via resonant tunneling. This process is repeated (cascaded) and another photon is emitted. A QCL typically contains 20 - 100 stages such that a substantial number of photons are generated per electron. As can be seen, the level 3 of the active region is not aligned with the miniband of the next stage and hence has a reasonably large lifetime ($\tau \sim 10$ ps) and thus can accumulate electrons. Level 2 doesn't sustain population since decay to level 1 takes place via a fast non-radiative transition and subsequent tunneling in the succeeding miniband ($\tau \sim 1$ ps).
There has been significant progress in both the design and performance of QCLs in the last decades [9], [10]. Both the active and the injector regions can be designed as a superlattice containing their own minibands and minigaps or by using the so-called bound-to-continuum scheme where lasing is achieved via a transition from a discrete upper state to a superlattice miniband [11]. Another

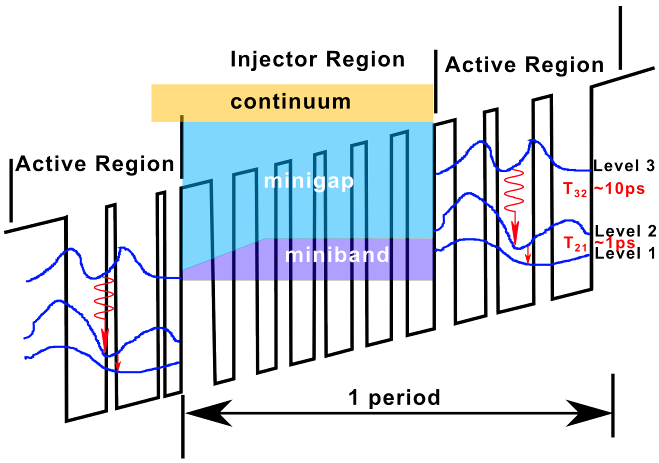

Figure 1.6: *Schematic diagram explaining the working principle of a quantum cascade laser relying on intersubband transitions [8].*

design replaces the injector regions altogether and works on the principle that the ground state of the active region gets aligned to the upper state of the next stage on application of suitable bias [12]. QCLs offer the following benefits as a light source for the mid-infrared wavelength range.

1. One can choose the peak wavelength of emission by tailoring the design of the active region.

2. QCLs are transparent on both sides of the central frequency (i.e they exhibit a lorentzian gain spectrum) unlike traditional band-to-band semiconductor lasers which absorb all photons with energy larger than the bandgap. Therefore many different types of active regions can be cascaded together allowing either muliwavelength lasing [13] or provide broad band gain [14].

3. Since QCLs are semiconductor lasers, arrays of integrated single wavelength lasers can be realized on a single chip [15].

It is also worth mentioning that due to the quantum mechanical selection rules, QCLs emit light with a polarization perpendicular to the layer structure which is usually referred as the transverse magnetic (TM) polarization. Another point worth noting is that the required electrical fields to align the injector and the active regions are of the order of 50 kV/cm^{-1} (~ 0.5 V per stage), which results in high power consumption. This in turn makes heat dissipation also an issue in QCLs and effective heat management is a key aspect of QCL design [16].

1.1.1.2 Interband Cascade Lasers

Another approach to mid-infrared light generation in semiconductor quantum wells was proposed by R.Q.Yang in 1995 which utilizes the transition between the electron state in the conduction band and the hole state in the valence band in a Sb-based type-II quantum well [17]. As the light is generated via a transition between the bands, this structure is called a Interband Cascade Laser (ICL). An ICL still retains the advantages of band gap engineering which allows for cascade injection and tailoring of the emission wavelength but since the transitions are interband, one can bypass the loss coming from fast phonon scattering. Moreover Auger recombination is reduced because of the type II nature of the transition. As a result of this, mid-infrared light generation is possible using ICLs at a much lower power budget. Roughly speaking, ICLs can operate at threshold power densities 30 times lower than that of QCLs [18] and light generation in the 3-6 μm wavelength range in CW operation at room temperature has been shown [19] and devices are commercially available.

1.1.2 Mid-ir light sources - state of the art

As discussed above, light generation in the mid-infrared wavelength range is possible on a chip scale using either QCLs or ICLs. In order to reach a wide tuning range, these lasers are typically assembled in two configurations as mentioned below

1. **External cavity feedback lasers:** This broadly tunable laser source consists of a semiconductor gain chip and a movable grating mounted in the Littrow configuration for providing feedback as depicted in Fig. 1.7 [20]. For mode hop free tuning, one not only has to rotate the grating but also has to adjust the cavity length. The rotational and longitudinal movement of the external grating needs to be controlled precisely for fine wavelength tuning and hence requires sensitive motion controllers. This in turn makes the entire package bulky and unsuitable for hand-held applications.

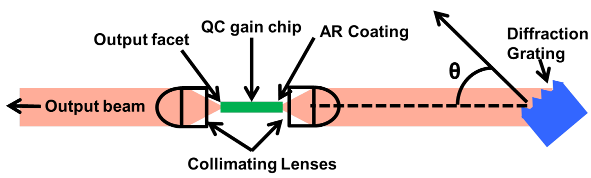

Figure 1.7: *A schematic diagram explaining the working principle of an external cavity quantum cascade laser.*

Such instruments are available today from companies such as DayLight Solutions Inc. [21] which provides modules covering a wide wavelength range from 3.25 μm to 12 μm.

2. **DFB array:** Another way of achieving single mode operation over a wide wavelength range is by realizing an array of DFB lasers. These DFB lasers can be typically tuned in a narrow wavelength range (0.1 - 0.3 μm) by changing the operating temperature. Depending on the application, one can either work with a single DFB laser or an array. However if one needs to collect the output of all the lasers at a single point then a setup requiring a lens and grating needs to be assembled [22] which again makes the overall package bulky. These DFB arrays are available from various companies such as ThorLabs (single DFB lasers) [23] or EOS photonics (DFB laser arrays) [24].

1.2 Applications of widely tunable mid-infrared lasers

1.2.1 Trace Gas Sensing

The present spectroscopic systems for mid-infrared trace gas sensing consist of a broadly tunable laser source and an interaction path as depicted in Fig. 1.8.

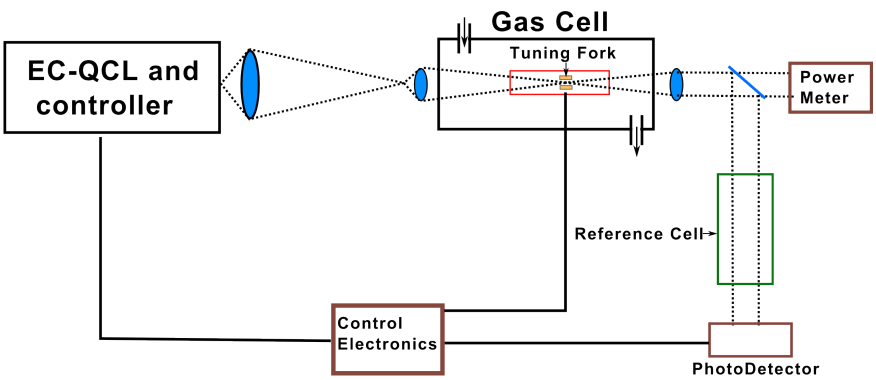

Figure 1.8: *A schematic diagram of the mid-infrared spectroscopic sensing system.*

Many detection techniques exist, an interesting approach being photo-acoustic spectroscopy (PAS). In this case, the interaction path is a multi-pass gas cell where the absorption of laser light creates a change in pressure which is then translated in sound. Ideally PAS is a background free detection technique as the signal only comes from the absorbing gas however there are other sources of noise such as absorption of the gas cell windows (coherent noise) and

Molecule	Detection Limit (SNR = 1)
NO[[25]]	15 ppb
CH_2O[[26]]	150 ppb
NO_2[[27]]	0.5 ppb
N_2O[[28]]	80 ppb
NH_3[[29]]	30 ppb
Hexamethyldisilazane[[30]]	200 ppb
O_3[[31]]	100 ppb

Table 1.2: *Table showing the amount of gas required to produce a signal to noise ratio of 1.*

external noise (incoherent noise). To get rid of these unwanted signals, one can introduce a sharply resonant acoustic transducer (such as a quartz tuning fork) in the gas cell. As the design of this sensing scheme is quite straight forward, it's becoming widely implemented for mid-infrared spectroscopy.
There are many other techniques mostly used for trace gas detection which involve a high finesse optical cavity. These techniques require a very precise alignment of the mid-infrared tunable lasers with the optical cavity in order to minimize the losses.
Using these techniques, it has been shown that detection of various trace gases at very low concentrations is possible as detailed in the table 1.2.

1.2.2 Liquid sensing

Detecting liquids in the mid-infrared wavelength range is relatively easier than detecting (trace) gases as one is typically looking for stronger and broader absorption features. However, one has to take into account the strong absorption of water in the mid-infrared. Therefore, the path lengths cannot be too long (~several tens of microns in water rich solutions). Here QCLs have an advantage over blackbody sources, due to their much higher power spectral density, allowing higher SNR in the measurements. Wide tunablity of the source is however a prerequisite. Such systems are being commercialized e.g. by QuantaRed [32] which utilize QCLs and a flow cell to detect oil in water. Another application to detect biological liquids such as glucose in human epidermis requires a similar scheme as for trace gas detection involving an externally tunable QCL and a PA cell. Glucose levels of 100 mg/dl have been sensed using this techniques [33].

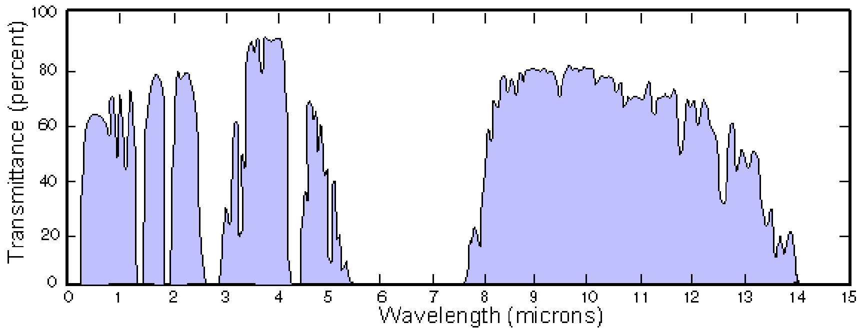

Figure 1.9: *Graph showing atmospheric transparency in the near and mid-infrared wavelength range.*

1.2.3 Remote Sensing

Remote sensing in the mid-infrared wavelength range is another attractive application. The earth's atmosphere is transparent in certain windows (3-5 μm and 8-12 μm) as shown in Fig. 1.9. In these wavelength windows trace molecules such as explosives (e.g. TNT) can be detected remotely [34].

1.2.4 QCL Microscopy

Another application based on EC-QCLs is microscopy in the mid-infrared wavelength range. In many applications such as tissue analysis, infrared microscopy can provide much more information than a simple visual microscopic inspection [35]. Traditionally this type of microscopy has been carried out using FTIR systems which consist of a broadband source, moving mirrors and cryogenic detectors. As a result, the entire system becomes bulky. Also given the low power spectral density of these sources the throughput is very low. The advent of QCLs paves a way to reduce the size of the system. As QCLs have higher power spectral densitiy, one can use microbolometers focal plane arrays operating at room temperatures for infrared microscopy [36]. As of today, there is a tabletop product called Spero from Daylight Solutions Inc which makes infrared microscopy possible with high spectral and spatial resolution at a higher throughput.
It's clear from this discussion that many attractive applications can be realized by using EC-QCLs. However the most expensive part in all these systems is still the EC-QCL itself. The remaining parts (e.g. the PA cell) are usually very cheap and thus at this point one needs a way to miniaturize the EC-QCL itself to make it low cost. If the system would moreover have no moving parts it would even allow for hand-held applications.

1.3 Photonic integration for the mid-infrared

Photonic integration has enabled the realization of complex optical functionalities on mm scale semiconductor chips. The major focus of photonic integration has been in the telecom wavelength range centered around wavelength of 1300 nm and 1550 nm. Various platforms exist to implement such PICs on: silica-on-silicon [37], III-V semiconductors [38], Lithium Niobate based [39] and polymer based [40].
The Silicon-on-Insulator (SOI) waveguide platform has emerged as an attractive candidate for realization of PICs operating at telecom wavelengths because it can be mass manufactured in the CMOS pilot lines used for manufacturing electronic ICs with minimal technological changes [41]. Moreover since the index contrast between waveguide core (Si, n = 3.42) and cladding (SiO_2, n = 1.42) is quite high, compact devices with very tight bends can be realized. For the telecom wavelength range, many components such as filters, interferometers, wavelength divison multiplexers have been realized in SOI PICs. Moreover SOI PICs have been used to realize compact laser and detector modules where III-V epitaxially grown layers have been integrated using bonding techniques or flip-chip integration.
This leads to the thought that photonic integration could also be used to miniaturize the mid-infrared spectroscopic systems or laser modules making them both low cost and compact. However none of the traditional waveguide platforms are suitable for mid-infrared photonics (except for III-V semiconductor technology) primarily because of being non-transparent beyond the near-ir (although SOI itself has an operational range till 4 μm wavelength and we will see in detail in the next chapter how it has been utilized to realize interesting functionalities in the mid-infrared wavelength range). Photonic integration can be envisaged to be used for the miniaturization and cost reduction of mid-infrared laser modules and spectrometers or for the miniaturization of complete mid-infrared spectroscopic systems, as will be discussed below.

1.3.1 Realization of widely tunable integrated lasers

As discussed in section 1.2 above, the present day widely tunable mid-infrared lasers are based on external feedback. One can think about providing the feedback to the semiconductor gain chip from another passive semiconductor chip containing wavelength selective devices. In order to do so, one would need to identify a passive waveguide platform and also the possible ways of integrating mid-infrared laser sources with passive PICs. The schematic diagram in Fig. 1.10 illustrates this principle showing a QCL gain chip integrated via flip chip bonding to a PIC which provides feedback using two tunable ring resonators.
As we will see in further chapters it was not possible to fabricate ring resonators

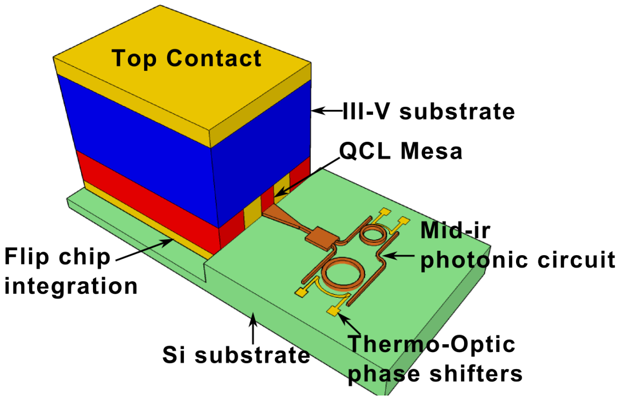

Figure 1.10: *Schematic diagram showing a possible way of realizing a widely tunable mid-infrared laser.*

in this thesis due to technological limitations. While ring resonators allow one to achieve strong spectral filtering, it's also possible to provide wavelength selective feedback based on cascaded MZIs as shown in Fig. 1.11. A standard FP QCL

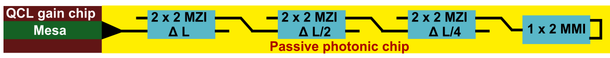

Figure 1.11: *A schematic diagram showing cascaded MZIs with different path length difference terminated by a 1×2 MMI whose outputs have been connected to each other. The circuit could be used to select only a desired part of the incoming wavelengths.*

laser has a reflectivity of ~30% at each of the facets. If a wavelength selective feedback from an external cavity present on a PIC is desired then the reflection from the facet of the FP cavity has to be reduced which could be done by using an AR coating and angling the facets. Adding a PIC in front of this facet would then dominate the reflection which is proportional to (a) the coupling loss introduced at the interface of the QCL FP laser and the PIC and (b) the insertion loss of the filter functions implemented on the PIC. For optimal performance, an overall reflectivity of at least 10% would be desirable.
Alternatively one can envisage the integration of an array of DFB lasers with an integrated optics multiplexer to reach a similar functionality as schematically shown in Fig. 1.12. In this scheme any light which is lost due to coupling and insertion loss of the multiplexer would result in lowering of the output power and hence the sensitivity of the sensing system in which the device will be used.

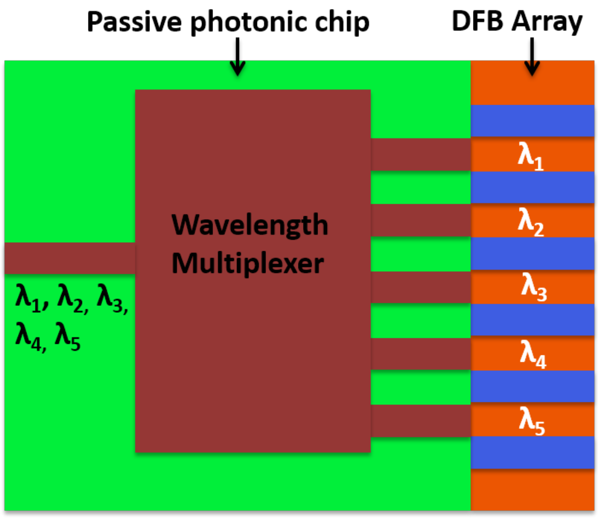

Figure 1.12: *A schematic diagram showing a wavelength (de)multiplexer integrated with an array of DFB QCLs.*

1.3.2 Realization of mid-infrared spectrometers

A true lab-on-a-chip spectroscopic system should essentially contain all the elements (light source, gas or liquid cell, detector or spectrometer) on a single chip. Two examples are given below in Fig. 1.13. In the first example, the output of an integrated mid-infrared LED is split in two arms one of which serves as reference while the other interacts with the desired gases or liquids. These arms are connected to spectrometers whose output is connected to photodetectors. The output of these photodetectors allow one to identify which species are present and at which concentration. Another example could be envisaged where the output of a tunable laser as realized in Fig. 1.10 is connected to an on-chip chopper (which could be realized using thermo-optic phase shifters). The output of the chopper is connected to two arms one of which acts as reference and another as the sensor. The output of these arms are connected to single photodetectors and a differential measurement of the output of these detectors would allow the detection of molecules again.

1.4 Scope of this thesis

This thesis details the results obtained for passive mid-infrared photonic integrated circuits in the Photonics Research Group at Ghent University. From the discussion above, we can deduce that PICs would pave way for compact and low

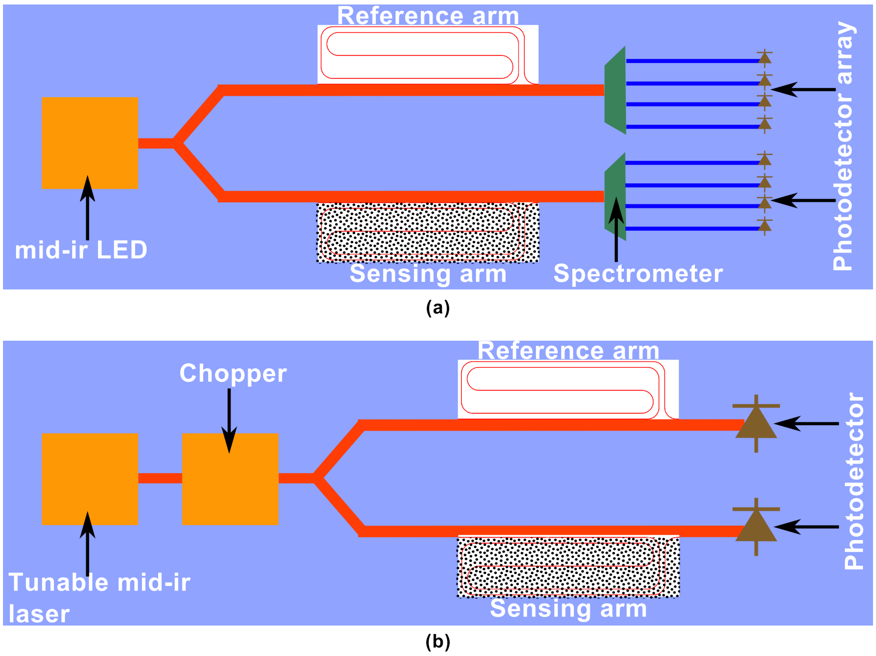

Figure 1.13: *Two examples to realize mid-infrared lab-on-a-chip systems.*

cost mid-infrared spectroscopic modules. This thesis focuses on the identification and demonstration of a suitable passive waveguide platform: germanium-on-silicon. The organization of the thesis is as follows: in chapter 2, we discuss various possible waveguide platforms for the mid-infrared wavelength range showing results obtained by various research groups worldwide. We discuss the associated pros and cons with each waveguide platform and conclude that germanium-on-silicon would be the most logical choice. In chapter 3, we discuss the fabrication flow for germanium-on-silicon waveguide circuits which is followed by a discussion on the design and experimental results of various passive waveguide devices in chapter 4. We also discuss the limitations in the performance of devices due to available fabrication tools. In chapter 5 we introduce the thermo-optic phase shifters and demonstrate that by clever design one can substantially lower the power consumption. Finally in chapter 6, we discuss the future prospects and provide some guidelines on what could be the next step towards the realization of widely tunable integrated mid-infrared light engines and spectroscopic systems.

References

[1] Colin N Banwell and Elaine M McCash. *Fundamentals of molecular spectroscopy.* McGraw-Hill London, 1994.

[2] *HITRAN on the Web, www.hitran.iao.ru.*

[3] *www.spectracalc.com.*

[4] *http://webbook.nist.gov/.*

[5] *http://www2.ups.edu/faculty/hanson/Spectroscopy/IR/IRfrequencies.html.*

[6] Weng W Chow, Stephan W Koch, and Murray Sargent III. *Semiconductor-laser physics.* Springer-Verlag New York, Inc., 1994.

[7] RF Kazarinov and RA Suris. *Possibility of the amplification of electromagnetic waves in a semiconductor with a supperlatice.* Soviet Physics-Semiconductors, 5(4), 1971.

[8] Jerome Faist, Federico Capasso, Deborah L Sivco, Carlo Sirtori, Albert L Hutchinson, and Alfred Y Cho. *Quantum cascade laser.* Science, 264(5158):553–556, 1994.

[9] Claire Gmachl, Federico Capasso, Deborah L Sivco, and Alfred Y Cho. *Recent progress in quantum cascade lasers and applications.* Reports on progress in physics, 64(11):1533, 2001.

[10] Mariano Troccoli, Laurent Diehl, David P Bour, Scott W Corzine, Nanfang Yu, Christine Y Wang, Mikhail A Belkin, Gloria Hofler, Rafal Lewicki, Gerard Wysocki, Frank K. Tittel, and Federico Capasso. *High-performance quantum cascade lasers grown by metal-organic vapor phase epitaxy and their applications to trace gas sensing.* Journal of Lightwave Technology,, 26(21):3534–3555, 2008.

[11] Jérôme Faist, Mattias Beck, Thierry Aellen, and Emilio Gini. *Quantum-cascade lasers based on a bound-to-continuum transition.* Applied Physics Letters, 78(2):147–149, 2001.

[12] Michael C Wanke, Federico Capasso, Claire Gmachl, Alessandro Tredicucci, Deborah L Sivco, Albert L Hutchinson, S-N George Chu, and Alfred Y Cho. *Injectorless quantum-cascade lasers.* Applied Physics Letters, 78(25):3950–3952, 2001.

[13] Claire Gmachl, Deborah L Sivco, James N Baillargeon, Albert L Hutchinson, Federico Capasso, and Alfred Y Cho. *Quantum cascade lasers with a heterogeneous cascade: Two-wavelength operation.* Applied Physics Letters, 79(5):572–574, 2001.

[14] Claire Gmachl, Deborah L Sivco, Raffaele Colombelli, Federico Capasso, and Alfred Y Cho. *Ultra-broadband semiconductor laser.* Nature, 415(6874):883–887, 2002.

[15] Benjamin G Lee, Mikhail A Belkin, C Pflugl, Laurent Diehl, Haifei A Zhang, Ross M Audet, Jim MacArthur, David P Bour, Scott W Corzine, GE Hufler, and Federico. Capasso. *DFB quantum cascade laser arrays.* IEEE Journal of Quantum Electronics,, 45(5):554–565, 2009.

[16] Vincenzo Spagnolo, Antonia Lops, Gaetano Scamarcio, Miriam S Vitiello, and Cinzia Di Franco. *Improved thermal management of mid-IR quantum cascade lasers.* Journal of Applied Physics, 103(4):043103–043103, 2008.

[17] Rui Q Yang. *Infrared laser based on intersubband transitions in quantum wells.* Superlattices and Microstructures, 17(1):77, 1995.

[18] RQ Yang, JD Bruno, JL Bradshaw, JT Pham, and DE Wortman. *High-power interband cascade lasers with quantum efficiency> 450%.* Electronics Letters, 35(15):1254–1255, 1999.

[19] William W Bewley, Chadwick L Canedy, Chul Soo Kim, Mijin Kim, Charles D Merritt, Joshua Abell, Igor Vurgaftman, and Jerry R Meyer. *Continuous-wave interband cascade lasers operating above room temperature at* λ*= 4.7-5.6* μm*.* Optics express, 20(3):3235–3240, 2012.

[20] Arun Mohan, Andreas Wittmann, Andreas Hugi, Stéphane Blaser, Marcella Giovannini, and Jérôme Faist. *Room-temperature continuous-wave operation of an external-cavity quantum cascade laser.* Optics letters, 32(19):2792–2794, 2007.

[21] *www.daylightsolutions.com.*

[22] Benjamin G Lee, Jan Kansky, Anish K Goyal, Christian Pflugl, Cgl, Laurent Diehl, Mikhail A Belkin, Antonio Sanchez, and Federico A Capasso. *Beam combining of quantum cascade laser arrays.* Optics express, 17(18):16216–16224, 2009.

[23] *www.thorlabs.com.*

[24] *www.eosphotonics.com.*

[25] V Spagnolo, AA Kosterev, L Dong, R Lewicki, and FK Tittel. *NO trace gas sensor based on quartz-enhanced photoacoustic spectroscopy and external cavity quantum cascade laser.* Applied Physics B, 100(1):125–130, 2010.

[26] Angela Elia, Cinzia Di Franco, Vincenzo Spagnolo, Pietro Mario Lugarà, and Gaetano Scamarcio. *Quantum cascade laser-based photoacoustic sensor for trace detection of formaldehyde gas.* Sensors, 9(4):2697–2705, 2009.

[27] Michael Pushkarsky, Alexei Tsekoun, Ilya G Dunayevskiy, Rowel Go, and C Kumar N Patel. *Sub-parts-per-billion level detection of NO2 using room-temperature quantum cascade lasers.* Proceedings of the National Academy of Sciences, 103(29):10846–10849, 2006.

[28] JP Lima, H Vargas, A Miklos, M Angelmahr, and P Hess. *Photoacoustic detection of NO2 and N2O using quantum cascade lasers.* Applied Physics B, 85(2-3):279–284, 2006.

[29] Marcelo G da Silva, Marcelo S Sthel, Delson U Schramm, Helion Vargas, Andras Miklós, Peter Hess, et al. *Ammonia detection by using quantum-cascade laser photoacoustic spectroscopy.* Applied optics, 45(20):4966–4971, 2006.

[30] A Elia, F Rizzi, C Di Franco, PM Lugarà, and G Scamarcio. *Quantum cascade laser-based photoacoustic spectroscopy of volatile chemicals: application to hexamethyldisilazane.* Spectrochimica Acta Part A: Molecular and Biomolecular Spectroscopy, 64(2):426–429, 2006.

[31] M Gomes da Silva, H Vargas, A Miklos, and P Hess. *Photoacoustic detection of ozone using a quantum cascade laser.* Applied Physics B, 78(6):677–680, 2004.

[32] *www.quantared.com.*

[33] Jonas Kottmann, Julien M Rey, Joachim Luginbühl, Ernst Reichmann, and Markus W Sigrist. *Glucose sensing in human epidermis using mid-infrared photoacoustic detection.* Biomedical optics express, 3(4):667–680, 2012.

[34] C Bauer, AK Sharma, U Willer, J Burgmeier, B Braunschweig, W Schade, S Blaser, L Hvozdara, A Mueller, and G Holl. *Potentials and limits of mid-infrared laser spectroscopy for the detection of explosives.* Applied Physics B, 92(3):327–333, 2008.

[35] M Diem, M Romeo, S Boydston-White, M Miljković, and C Matthäus. *A decade of vibrational micro-spectroscopy of human cells and tissue (1994–2004).* Analyst, 129(10):880–885, 2004.

[36] Miles J Weida and Brandon Yee. *Quantum cascade laser-based replacement for FTIR microscopy.* In SPIE BiOS, pages 79021C–79021C, 2011.

[37] Tetsuo Miya. *Silica-based planar lightwave circuits: passive and thermally active devices.* IEEE Journal of Selected Topics in Quantum Electronics,, 6(1):38–45, 2000.

[38] Radhakrishnan Nagarajan, Masaki Kato, Jacco Pleumeekers, Peter Evans, Scott Corzine, Sheila Hurtt, Andrew Dentai, Sanjeev Murthy, Mark Missey, Ranjani Muthiah, et al. *InP photonic integrated circuits.* IEEE Journal of Selected Topics in Quantum Electronics,, 16(5):1113–1125, 2010.

[39] Ed L Wooten, Karl M Kissa, Alfredo Yi-Yan, Edmond J Murphy, Donald A Lafaw, Peter F Hallemeier, David Maack, Daniel V Attanasio, Daniel J Fritz, Gregory J McBrien, et al. *A review of lithium niobate modulators for fiber-optic communications systems.* IEEE Journal of Selected Topics in Quantum Electronics,, 6(1):69–82, 2000.

[40] Louay Eldada and Lawrence W Shacklette. *Advances in polymer integrated optics.* IEEE Journal of Selected Topics in Quantum Electronics, 6(1):54–68, 2000.

[41] Richard Soref. *The past, present, and future of silicon photonics.* IEEE Journal of Selected Topics in Quantum Electronics, 12(6):1678–1687, 2006.

2

Waveguide platforms for the mid-infrared

“You have to learn the rules of the game. And then you have to play better than anyone else."

– Albert Einstein

2.1 Introduction

As we described briefly in the previous chapter, the established and traditional waveguide platforms for integrated photonics will not be suitable for mid-infrared photonics. Although material transparency is the first criterion for constructing a waveguide platform, there are other important requirements which must be explored before zeroing in on a particular waveguide platform. The very first consideration which must be kept in mind is that the materials are physically stable and can be handled easily (e.g. KBr is known to have a wide transparency from visible to mid-infrared wavelengths however it absorbs water vapor present in the atmosphere and thus becomes unusable after certain time [1]). Another boundary condition which can be put for choosing the appropriate waveguide platform is that the materials can be processed in a standard CMOS line. CMOS lines are primarily used for producing large scale electronic circuits based on silicon. The large scale manufacturing capabilities make the overall cost of an electronic chip (and hence also a photonic chip)affordable. Another important consideration is that the fabrication process should be straight forward such that high yield can be obtained. In this chapter, we will first begin by having a look at the limitations of the SOI waveguide platform and then we shall have a look at the possible waveguide platforms for the mid-infrared wavelength range and discuss pros and cons associated with each one of them.

2.2 SOI waveguide platform

As explained briefly in the first chapter, SOI has now emerged as an important platform for operation in the telecom wavelength range around 1.3 μm and 1.55 μm. There are several reasons listed below why this material platform has become so attractive.

1. **CMOS compatibility:** The electronic industry uses SOI to manufacture integrated circuits on a full wafer scale. The tools which are used to process these electronic chips can be utilized to manufacture photonic circuits requiring little additional technology development. This also makes these photonic chips cost efficient, when produced in large volumes.

2. **Material transparency:** Both silicon and silicon dioxide are fully transparent for operation in the telecom wavelength range which implies that the losses in the photonic circuits are determined by scattering loss due to waveguide roughness (fabrication dependent) and free carrier absorption loss due to doping.

3. **Large index contrast:** The refractive index contrast between silicon (n = 3.42) and silicon dioxide (1.42) insures that circuits can be made with very tight bends (5 μm bending radius). This results in compact circuits meaning a large number of photonic devices can be packed in a very small area.

Because of the above mentioned points, significant amount of research has taken place on the SOI waveguide platform and many optical functionalities (low loss waveguides, WDM devices, resonators) [2] along with high speed modulators [3] and germanium photodetectors [4] have been realized on a photonic chip. Also, the integration of active devices such as lasers and photodetectors using adhesive or molecular bonding on SOI chips [5] has resulted in small scale tunable lasers and complete lab-on-a-chip systems. The standard photonic SOI waveguide platform consists of a device silicon layer of thickness between 220 nm and 400 nm and a buried oxide of thickness 2 μm.
If we could utilize the SOI waveguide platform in the mid-infrared wavelength range, it would require little further technology development and we can tap all the above mentioned advantages.

2.2.1 Mid-infrared SOI waveguide platform

The advantages offered by the SOI waveguide platform has caused researchers to investigate the use of the SOI waveguide platform for the mid-infrared wavelength range. Various photonic components like grating couplers,ring resonators, MZIs, AWGs, PCGs have been demonstrated up to a wavelength of 3.8 μm [6], [7], [8], [9]. However beyond 3.8 μm, the very first problem one encounters is that the buried oxide starts absorbing heavily. The absorption loss as a function of wavelength for SiO_2, Si and Ge is shown in Fig. 2.1(a), (b) and (c) respectively [10]. It can be seen that while silicon and germanium are transparent in the mid-infrared wavelength range, SiO_2 absorbs heavily. This means that the waveguide losses will start going up considerably as the wavelength of operation is increased. Another source of loss in integrated waveguides is the leakage of the waveguide mode to the substrate. As the substrate is the same material as the guiding core in SOI waveguides, the mode propagating in the waveguide core can leak in the substrate. A thick buried oxide layer therefore is required to prevent this leakage. As described above standard SOI waveguides contain a layer of 220 nm to 400 nm Si and a 2 μm buried oxide. A simulation of the leakage loss has been performed using Fimmwave [11] as shown in Fig. 2.1(d) for a fully etched 400 nm Si waveguide on a 2 μm BOX as a function of wavelength. The width of the waveguide was adjusted to be single mode for TE polarization at each wavelength. It can be seen that after 4μm wavelength, the leakage loss becomes substantial. Another possible challenge which can arise in using the SOI waveguide platform for the mid-infrared is the efficient

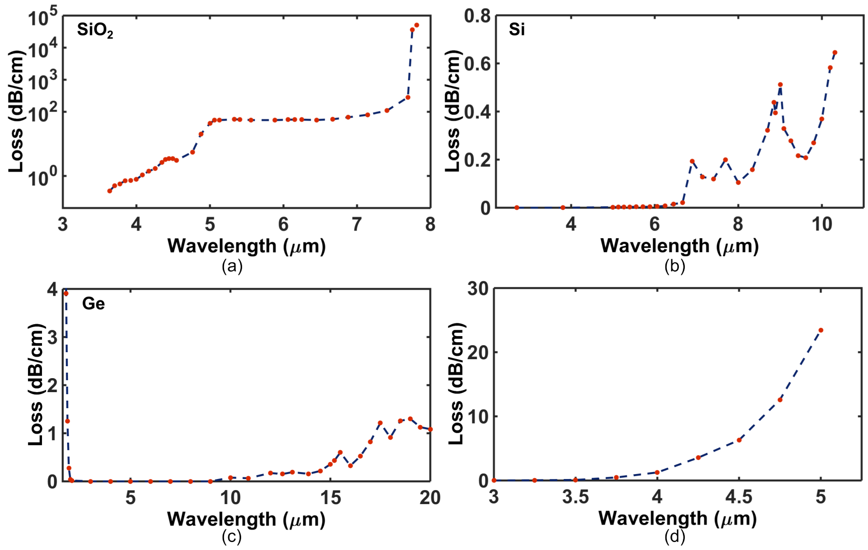

Figure 2.1: *Absorption loss of (a) thermal SiO_2, (b) crystalline silicon, (c) crystalline germanium as a function of wavelength and (d) substrate leakage loss of a fully etched 400 nm thick Si waveguide as a function of wavelength.*

coupling of an on-chip light source to the waveguide. As described above, lasers can be integrated with SOI chips using bonding techniques or by flip chip integration. Given the high power dissipation of mid-infrared laser sources, flip chip integration is preferred and requires butt coupling between the silicon passive waveguide structure and the III-V laser waveguide. However, the mode mismatch between the light source and the standard SOI waveguide becomes significant resulting in a poor coupling. This is discussed later in chapter 6.

2.3 Search for alternate waveguide platforms

The discussion in the previous paragraphs confirms that a novel waveguide platform needs to be identified for the mid-infrared wavelength range. Let's begin by having a look at the conditions this new waveguide platform needs to fulfill.

1. **Transparency in the wide mid-infrared:** The materials which constitute the waveguide platform must be transparent in a wide wavelength range such that they can be utilized at the wavelength of choice.

2. **CMOS compatibility:** It should be possible to fabricate the waveguide cir-

cuits in a standard CMOS pilot line. CMOS compatibility will enable mass manufacturing and the overall cost of the photonic chip will be reduced significantly.

3. **Simple fabrication scheme:** The fabrication scheme of the waveguide platform should be straightforward. Preferably the fabrication scheme should not contain a critical failure step.

Let's now have a look at possible alternate waveguide platforms based on the above mentioned points. A very nice review of the possible waveguide platforms for the mid-infrared wavelength range has been given by Richard Soref in [12] and [13]. Silicon itself has a large transparency window from 1.1 μm to 8 μm and therefore it would be appealing to build a waveguide platform which is based on silicon provided it satisfies the last two points as well. Table 2.1 describes various materials with their transparency windows.

Material	**Transparency Window** (μm)	**Refractive Index**
Silicon	1.2 - 8.0	3.45
Germanium	1.7-14.0	4
Silicon Nitride	0.4 - 5.0	1.8
Chalcogenides	1.0 - 14.0	2.0
Sapphire	0.4 - 5.5	1.6
Silicon Dioxide	0.4 - 3.8	1.4

Table 2.1: *Table describing the transparency windows and refractive indices of various materials [10], [12], [13]*

There has been quite some work on waveguide platforms based on these materials around the world. We discuss below each of the cases and highlight the pros and cons for each one of them.

2.3.1 Free standing Silicon

The free standing silicon waveguide platform takes advantage of the fact that silicon itself has a very wide transparency window. If the underlying oxide in the SOI waveguide platform can be removed then the resulting waveguide platform will allow operation over a broad wavelength range (in principle till about 8 μm).

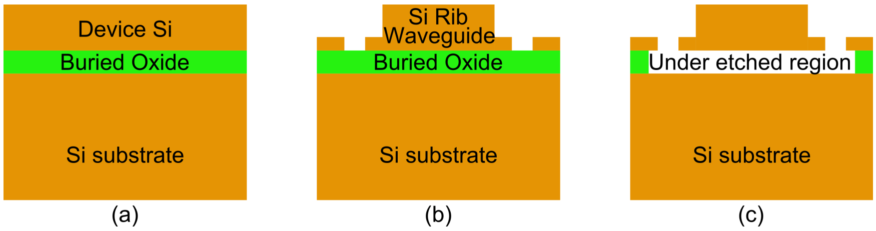

Figure 2.2: *Schematic diagram showing the fabrication process for Free standing Si waveguides. (a) A SOI wafer, (b) Rib waveguide definition and etching of holes around the waveguide and (c) under etching the buried oxide with HF.*

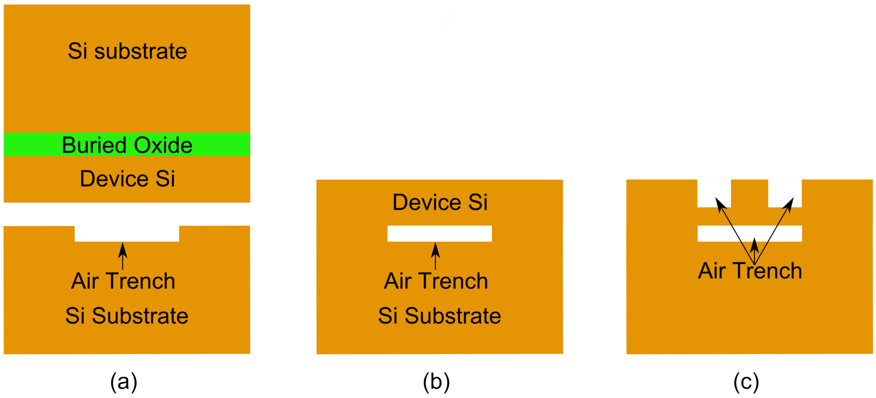

Figure 2.3: *Schematic diagram showing the fabrication process of free standing silicon waveguides using molecular bonding. (a) Trench etching in the silicon wafer, (b) molecular bonding of the SOI wafer with Si wafer and substrate removal and (c) waveguide etching on top of trench (from [14])*

2.3.1.1 Fabrication Scheme

There are two fabrication schemes for this waveguide platform as schematically depicted in Fig. 2.2. In the first scheme, rib type waveguides are defined on a SOI wafer and then holes are etched around the waveguides to access the underlying oxide. An exposure to hydrofluoric (HF) acid then etches away this underlying oxide without attacking the silicon layer [15], [16]. A SEM image of such a free standing waveguide fabricated by the author can be seen in Fig. 2.4(a). The top silicon was 1.5μm thick of which 1 μm was etched to form rib type waveguides. A slightly different version of this fabrication scheme requiring only one etch step using a sub-wavelength grating as cladding has been developed in [17] as seen in Fig. 2.5(a). This scheme makes the structure a bit more mechanically stable. In the second scheme as shown schematically in Fig. 2.3, a bulk Si wafer with trenches is directly bonded with the device Si layer of a SOI wafer. The substrate of the SOI wafer and the buried oxide are then removed from the SOI wafer and waveguides are fabricated on the Si device layer. A SEM image of a fabricated waveguide can be seen in Fig. 2.4(b) [14].

2.3.1.2 Realized Devices

Free standing waveguides in principle can be made very low loss as silicon etching is a very well studied process in both electronics and photonics. A waveguide loss of 3 dB/cm was reported in [15] where an all pass ring resonator with a Q-factor of 8100 was also demonstrated along with a grating coupler operating at a wavelength of 2.75 μm. Similar waveguide loss (2.8 dB/cm at 3.39 μm) was also reported in [14]. In [16] a waveguide loss of 27 dB/cm at 3.39 μm and 36 dB/cm at 5.2 μm and the Q-factor of all pass ring resonators was reported to be 11000 and 6800 respectively.

2.3.1.3 Limitations

The limitations of this waveguide platform are related to both fabrication and the type of devices which could be realized. From a fabrication point of view, in the first scheme, the free standing waveguides are prone to collapsing during oxide removal using wet HF etching. This happens because when the liquid is being dried, the contact angle between silicon and water becomes less than 90° which results in an attractive force between the device layer and the substrate. A possible solution could be to use vapor phase HF or critical point drying. At critical point, the transition from liquid to gas phase can be done without a change in surface tension and hence there are no issues with stiction. In the second scheme the waveguides are required to be defined only on the top of etched trenches in the handle silicon wafer. From the design point of view, a common disadvantage associated with both these schemes is that this waveguide platform makes it very difficult to realize devices like MMIs, AWGs, PCGs etc. which contain a larger multimode slab region that is difficult to make free standing. Also, this waveguide platform will be transparent only up to a wavelength of 8 μm.

2.3.2 Silicon-on-Sapphire

Silicon-on-Sapphire (SOS) is another silicon based waveguide platform which can be used in the mid-infrared wavelength range. SOS is in fact used as alternative for SOI wafers by electronics industry for specific applications like radio frequency circuits.

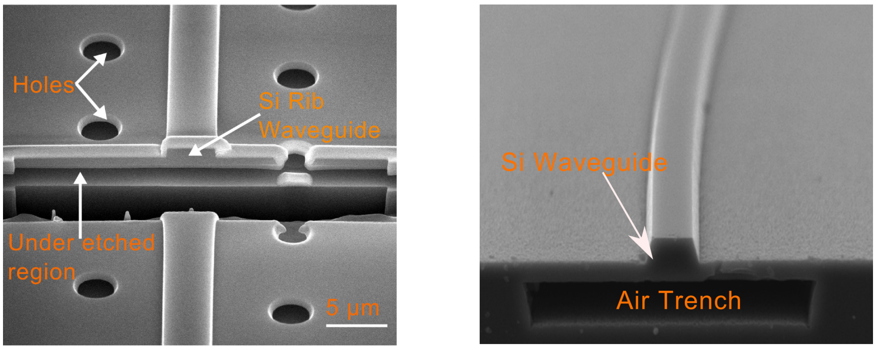

(a) (b)

Figure 2.4: *SEM images showing a free standing Si waveguide fabricated using (a) oxide undercut and (b) molecular bonding (from [14]).*

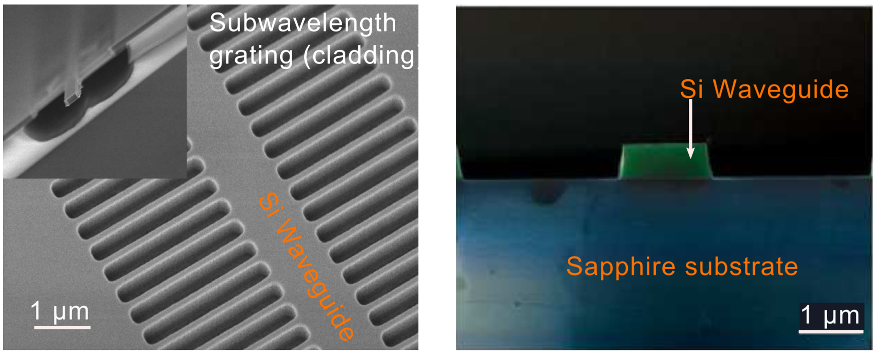

(a) (b)

Figure 2.5: *(a) SEM image showing the free stading waveguide with a subwavelength grating as cladding (from [17]). The inset shows the cleaved facet. (b) A false colored SEM image of a silicon on sapphire waveguide (from [18])*

2.3.2.1 Fabrication scheme

The fabrication of SOS waveguide circuits looks straightforward. A layer of silicon is grown epitaxially on a sapphire substrate and then waveguide patterns are defined in this top silicon layer using dry etching techniques [18], [19]. The difficulty however lies in the annealing of the Si films to reduce the threading dislocation density to sufficiently low levels. A false colored SEM image of such a fabricated waveguide can be seen in Fig. 2.5(b).

2.3.2.2 Realized devices

This waveguide platform can also be considered as CMOS compatible and there is an added advantage that there is no light leakage to the substrate. However apart from side wall roughness and absorption by surface states, another source of loss is the material quality of epitaxially grown silicon. The reported waveguide losses range from 2 dB/cm at 5.18 μm [20] to 4.3 dB/cm at 4.5 μm [18]. All pass rings with Q-factors as high as 151000 and photonic crystal cavities with Q-factor of 13600 were demonstrated in [21] and [22].

2.3.2.3 Limitations

The biggest limitation of the SOS waveguide platform is its operational wavelength range which is limited by the transparency of the sapphire substrate as it starts absorbing beyond 5 μm. Moreover it would be difficult to realize efficient thermo-optic modulators in this waveguide platform as sapphire has a thermal conductivity of 34 W/(m.K) which would mean that the heat is efficiently sunk in the substrate. As the SOI waveguide platform is suitable till about 4 μm and realization of efficient thermo-optic modulators is possible, this waveguide platform extends the operational wavelength range marginally.

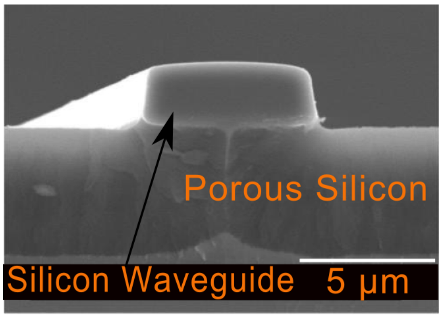

Figure 2.6: *A SEM image of silicon on porous silicon waveguide from [23]*

2.3.3 Silicon-on-Porous Silicon

Porous silicon is an interesting material which is formed by electrochemical partial dissolution of silicon. Depending on the preparation conditions, the refractive index of porous silicon can be tuned from a value of 1.4 to 3 [24]. Therefore waveguides can be fabricated using a layer of silicon and porous silicon. An approach to fabricate such waveguides has been discussed in [23] where proton irradiation, etching in a solution of HF, water and ethanol and annealing was performed to make the silicon porous underneath the waveguide with a refractive index of 1.4. A major issue with this waveguide platform is the damage which is introduced in the silicon crystal during ion implantation which is responsible for higher waveguide losses. A SEM image is shown in Fig 2.6. The waveguide loss was found to be 3.9 dB/cm at 3.39 μm which is attributed to surface roughness. There have been no reports to our knowledge on any devices based on this waveguide platform.

2.3.4 Silicon Pedestal Waveguides

Silicon pedestal waveguides are based on a novel fabrication technique and are fully composed of silicon.

2.3.4.1 Fabrication Scheme

As schematically shown in Fig. 2.7, the fabrication begins by depositing a thermal oxide on top of a silicon wafer. The thermal oxide and silicon are patterned using dry etching, following which a thin PECVD conformal oxide is deposited. The PECVD oxide is then etched anisotropically using dry etching and an undercut is then performed using SF_6 plasma [25]. If proper undercut parameters are chosen then the structure will support a guided mode in the top silicon.

2.3.4.2 Realized devices

The only contributing source of loss in silicon pedestal is silicon etching. As a result, low loss waveguides (2.7 dB/cm at 3.7 μm) have been demonstrated along with a Y branch splitter [25].

2.3.4.3 Limitations

The major limitation of this waveguide platform comes from the complicated fabrication scheme. Moreover slab based devices can't be realized as the wider slabs which are supported by a thin pillar would be mechanically unstable and also require larger undercut than single mode waveguides.

2.3.5 Silicon nitride based waveguide platforms

There have been reports on silicon-nitride based waveguides in past years as high quality silicon nitride is transparent till 5.5 μm. There have been two approaches to utilize silicon nitride for mid-infrared photonic integrated circuits. In the first approach, SiN is used as a cladding layer while in the second it's used as the waveguide core.

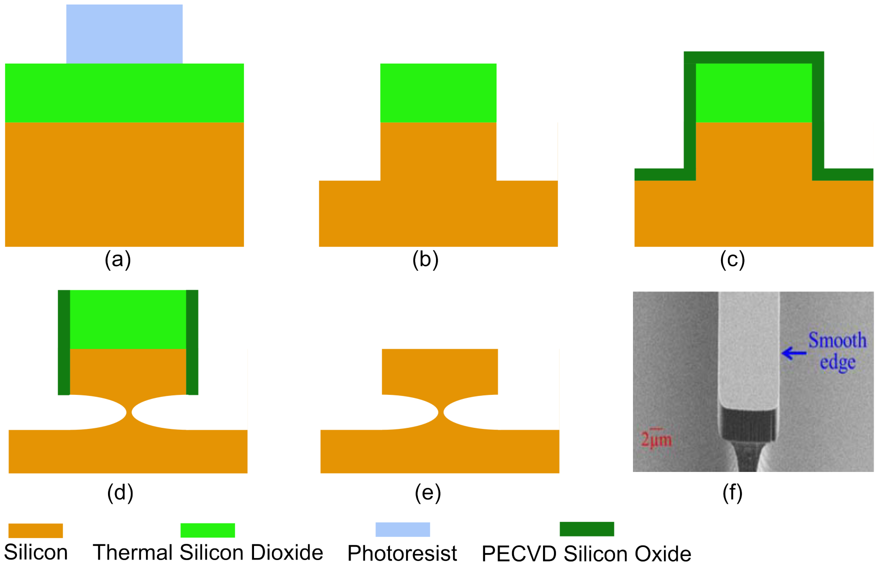

Figure 2.7: *Schematic diagram for the fabrication of pedestal waveguides. (a) Patterned photoresist on a silicon wafer with thermal oxide, (b) anisotropic etching of silicon oxide and silicon, (c) PECVD oxide deposition, (d) Anisotropic PECVD oxide removal and undercut using SF_6, (e) Removal of silicon oxide by HF dip and (f) a SEM image showing such a waveguide from [25]*

2.3.5.1 Fabrication scheme

As shown schematically in Fig. 2.8, the first approach requires the growth of a thick SiN layer on a SOI wafer which is then adhesively bonded to a Si substrate. The SiN surface is coated with a spin-on-glass (SOG) layer while the Si substrate contains layers of PECVD oxide and SOG. The SOI substrate and the buried oxide is then removed using grinding and etching [26]. Waveguides are patterned on this transferred silicon film as can be seen in a SEM image in Fig. 2.9(a). The second approach requires the deposition of a thick LPCVD silicon nitride film on silicon dioxide [27] which is then patterned into waveguide circuits.

2.3.5.2 Realized Devices

There have been demonstrations of low loss waveguides in both fabrication schemes with losses of 5.2 dB/cm at 3.39 μm in the first fabrication scheme [26] and 2.1 dB/cm at 3.7 μm [27]. Although directional couplers have been demonstrated using SiN as waveguide core [27], their implementation in devices like ring resonators or MZIs to our knowledge has not been realized.

2.3.5.3 Limitations

The first waveguide platform faces the problem that the silicon nitride quality is always an issue using PECVD. The incorporation of hydrogen in the films causes strong absorption in the mid-infrared [28], [29]. While better quality fims can be obtained using LPCVD as done in [27], the high strain in the material prevents the growth of thick layers beyond a few microns which is typically required for mid-infrared waveguides. Although claims have been made that the nitride films are transparent up till 8 μm, the longest demonstrated wavelength of operation to our knowledge is 3.75 μm on silicon nitride based waveguides. Also, in the scheme where SiN serves as waveguide core, it would be difficult to realize efficient thermo-optic phase shifters as the thermo-optic coefficient of SiN is one order of magnitude less as compared to silicon.

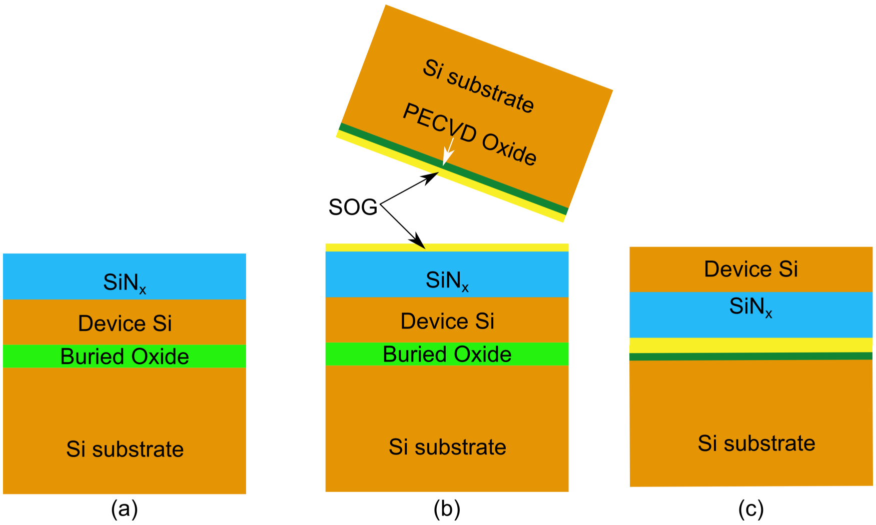

Figure 2.8: *Schematic diagram showing the fabrication scheme for silicon on silicon nitride waveguides. (a) Deposition of a thick silicon nitride film on SOI wafer, (b) bonding after spin coating adhesive SOG layer and (c) substrate removal from the SOI wafer (from [26]).*

2.3.6 Hollow Core Waveguides

Hollow core waveguides contain an air filled core which is surrounded by a series of coatings which confine the light within the core. Light is guided either by having a Bragg cladding or with an anti-resonance reflecting optical waveguide (ARROW) structure [30]. The Bragg cladding comprises of two layers of different materials (called a bilayer) which reflect incident light for any angle or polarization. To increase reflection, the number of bilayers can be increased. ARROW claddings confine light in the core by interferometric effects where the thickness of the two cladding layers is chosen in such fashion that the reflected light is at the antiresonance of the Fabry-Perot cavity formed in the layer stack. Although these hollow core waveguides do make an interesting case as an alternative waveguide platform, they have a very challenging fabrication scheme. It begins with deposition of dielectric layers on a substrate and then a sacrificial layer of aluminium is deposited and patterned which is followed by growth of dielectric layers. The aluminium layer is then removed using selective wet etching as can be seen in Fig. 2.9(b) [31]. Waveguide losses for telecom wavelength range were found out to be 2.6 dB/cm [32]. To our knowledge, there has been no experimental demonstration for the mid-infrared wavelength range however it has been shown by using 3-D beam propagation simulation in [30] that losses as low as 0.06 dB/cm can be achieved at a wavelength of 3.39 μm.

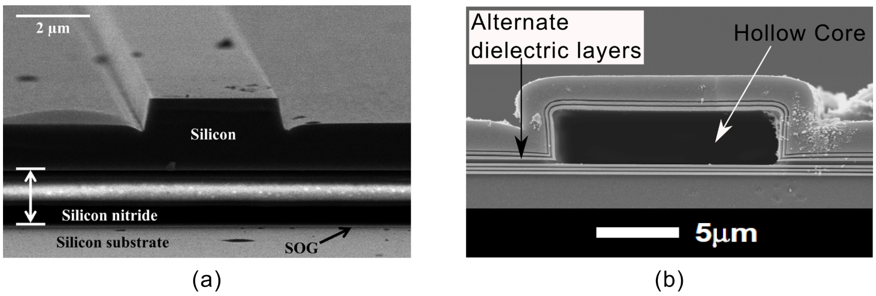

Figure 2.9: *SEM image of (a) Silicon on silicon nitride waveguide fabricated by wafer bonding (from [26])and (b) hollow core waveguide(from [31])*

2.3.7 Chalcogenide based waveguide platforms

Chalcogenides are glasses containing elements like S,Se and Te which can be transparent in a very wide wavelength range [33]. Also, their refractive indices can be tailored by changing the composition. There have been several waveguide platforms reported based on chalcogenide glasses.

2.3.7.1 Fabrication Scheme

As shown in Fig. 2.10, As_2S_3 waveguides have been prepared by using a micromolding technique using PDMS [34]. A PDMS mold is prepared on SU-8 waveguides and then transferred to a GaAs substrate. As_2S_3 solution is filled in the hollow channels and baking results in solid waveguides. Also, as depicted in Fig. 2.11, As_2Se_3 waveguides have been prepared by evaporation and lift off on a $Ge_{23}Sb_7S_{70}$ cladding [35]. Another way to fabricating As_2S_3 waveguides is spin coating a layer in SiO_2 channels [36].

2.3.7.2 Realized Devices

As chalcogenides can be made widely transparent, waveguides with losses as low as 0.7 dB/cm at 5.2 μm are reported [35] along with an all pass ring resonator with Q factor 200000.

2.3.7.3 Limitations

The biggest limitation of chalcogenide based waveguides is that the overall fabrication process remains quite complicated and moreover is not CMOS compatible. Therefore this waveguide platform won't be able to tap the full advantage of CMOS pilot lines.

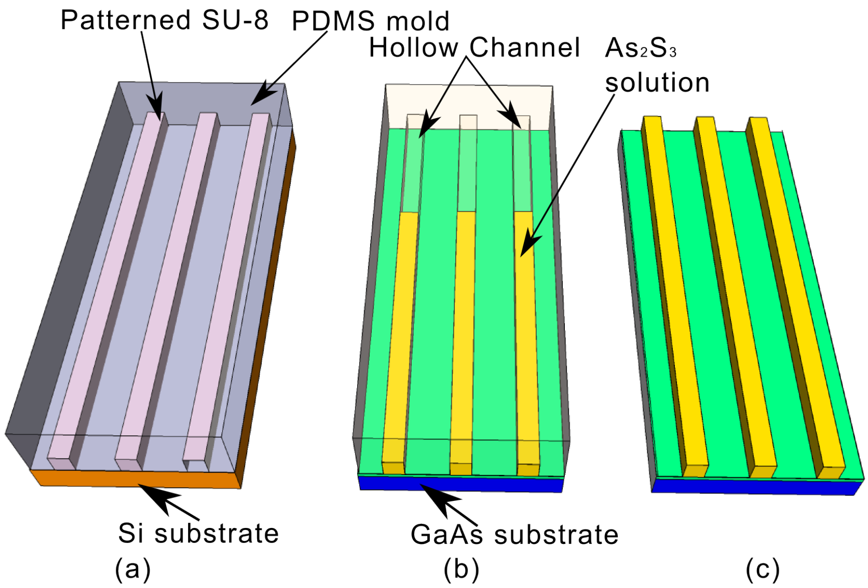

Figure 2.10: *Fabrication scheme for As_2S_3 waveguides on a GaAs substrate. (a) SU-8 is patterned using lithography on a silicon substrate and a PDMS mold is spin coated on top, (b) the PDMS mold is stamped on a GaAs substrate and the As_2S_3 solution is filled in the channels by capillary action and (c) hard baking results in solid waveguides after which PDMS mold is peeled away (from [34]).*

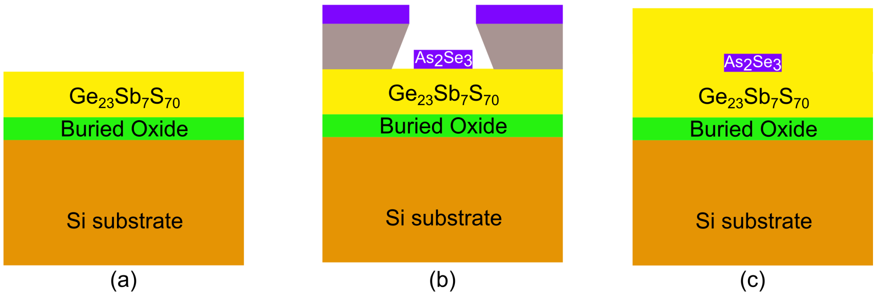

Figure 2.11: *Schematic fabrication scheme for As_2Se_3 on $Ge_{23}Sb_7S_{70}$ waveguides. (a) A $Ge_{23}Sb_7S_{70}$ film is deposited on thermal oxide grown on a silicon wafer, (b) image reversal lithography is performed and As_2Se_3 films are evaporated and (c) an over-cladding of $Ge_{23}Sb_7S_{70}$ is deposited to prevent surface oxidation (from [35]).*

2.3.8 Silicon on CaF_2 Waveguides

Transfer printing technology [38] allows one to achieve the desired combination of thin films on top of each other. Usually this technique is employed for realizing flexible electronic circuits [38] but can also be utilized to chose the desired core and cladding in an optical waveguide [39]. Mid-infrared Si waveguides have been created using this technique as described in [37].

2.3.8.1 Fabrication Scheme

The fabrication flow is depicted in Fig 2.12. A pattern of holes is defined on a SOI die using lithography and dry etching. These holes provide access to the buried oxide where an undercut region is created by partial etching in HF solution. A photoresist layer is then spin coated on top which fills the holes and the undercut region. Flood exposure of resist causes development all across the die except for the areas where the resist is beneath silicon. A complete removal of the buried oxide is then done using HF etching after which the underlying resist acts as pedestal support for the silicon film. A PDMS film is then laminated to the silicon device layer and when it's peeled, the silicon layer is removed with it. The silicon film is then pressed to a CaF_2 substrate (transparent in a wavelength range of 400 nm to 9 μm) completing the transfer. Desired patterns can be then defined on this transferred silicon film.

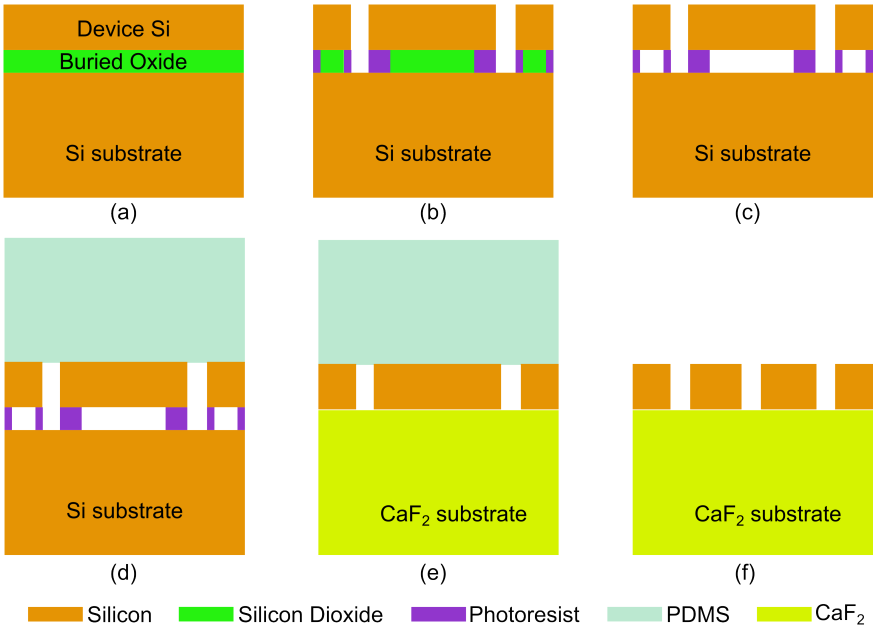

Figure 2.12: *Fabrication flow for silicon on CaF_2 waveguides. (a) SOI die, (b) complete etching of silicon layer, partial undercut and photoresist filling in undercut region, (c) complete removal of oxide, (d) lamination of PDMS film, (e) peeling of PDMS and placing the silicon layer on CaF_2 substrate and (f) removal of PDMS film. Desired waveguide patterns can be etched on this silicon film (from [37])*

2.3.8.2 Realized Devices

As is the case with all silicon based waveguide platforms, optimal silicon etching would allow one to achieve low loss waveguides. Waveguide losses of 3.8 dB/cm at 5.2 μm were reported along with an all pass ring resonator of Q factor 37000.

2.3.8.3 Limitations

Although this method allows one to transfer silicon to any substrate with wide transparency range, the fabrication scheme of these waveguides remains quite complicated rendering mass manufacturing difficult. Moreover these waveguides require the definition of holes to lift the silicon meaning that slab type devices can't be lifted easily.

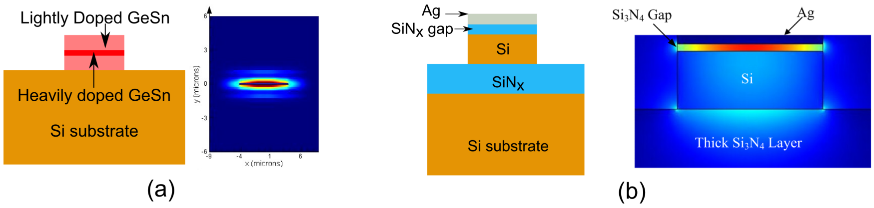

Figure 2.13: *(a) Schematic diagram of a GeSn plasmonic waveguide and (b) a multi-layer plasmonic waveguide along with the simulated mode profiles (from [40] and [41])*

2.3.9 Surface Plasmon Waveguides

Surface plasmons (or surface plasmon polaritons, SPP, to be precise) are electromagnetic excitations that propagate along the interface of a metal and a dielectric. Using Maxwell's equations it can be proved that surface plasmons can exist at the boundary of two materials if their dielectric constants (ϵ) have opposite signs which is the case at the interface of a metal ($\epsilon < 0$) and a dielectric ($\epsilon > 0$). In this configuration, an electro-magnetic wave is generated in the dielectric and an electron plasma is generated in the metal; both of which are exponentially decaying [42]. Several potential candidates have been proposed in the literature.

As discussed above, CMOS compatibility will be a key aspect to the waveguide platform as it will enable mass manufacturing. However most metals which are typically used in plasmonics (such as silver and gold) are not allowed in CMOS pilot lines because of contamination issues. In an all silicon platform, there can be two ways of achieving a negative dielectric constant namely by heavily doping the silicon or other CMOS compatible materials selectively and by using silicides such as $PtSi_2$,NiSi,Pd_2Si,WSi_2. It has been shown in [43] that these SPP waveguides can operate in the mid-infrared wavelength regime.

Fig 2.13(a) shows the schematic diagram of the proposed GeSn plasmonic waveguide along with the simulated mode profile at 8 μm [40] where a heavily doped strip of GeSn is sandwiched between lightly doped GeSn strips. It has been shown that for doping values greater than 10^{20}cm^{-3} the waveguide will operate in the 1 - 5 μm wavelength range while for lower doping levels it can work in the 7 - 15 μm wavelength range.

Another approach to realize SPP waveguides has been proposed in [41] where a SiN insulating layer is sandwiched between a metallic layer (Ag) and a high index dielectric substrate (Si). The fundamental transverse magnetic mode is confined in the insulating material. To increase the confinement and avoid substrate leakage at longer wavelengths, this structure is made five layered consisting of Ag,SiN gap, Si, SiN and then the thick dielectric Si substrate. A

schematic diagram of such a waveguide is shown in Fig. 2.13(b) along with the electric field distribution of the TM_{00} mode at a wavelength of 4.0 μm.
Although plasmonic waveguides do offer some interesting capabilities, the difficulty to fabricate (because of very high doping levels and CMOS incompatible metals) and relatively high losses makes them less attractive than dielectric waveguide structures.

2.3.10 Germanium-on-Silicon

Ge-on-Si is quite an interesting waveguide platform for the mid-infrared wavelength range. It's fully CMOS compatible as both germanium and silicon are used heavily by the CMOS industry. The fabrication process as described in the next chapter is quite straightforward. The first work on Ge-on-Si waveguides was done by EPFL and they reported a waveguide loss of 2.5 dB/cm at a wavelength of 5.8 μm [44], in which case epitaxially grown germanium films were etched in desired patterns. The results for waveguide losses and the realized photonic components obtained in this work are detailed in the forthcoming chapters. There are two slightly different versions of this waveguide platform. In the first version, germanium films are grown in the trenches etched in SiO_2 matrix on a silicon wafer as schematically shown in Fig. 2.14. This requires a CMP step to polish the germanium facets [45]. Although waveguides have been made using this technology [46], to our knowledge no loss values have been reported. A major issue in following this type of approach is that integrated photonic circuits require waveguides of different widths which can result in difficult control on the growth and CMP. A SEM image of such a waveguide can be seen in Fig. 2.15(a). The second version of this waveguide platform has been developed by CEA-LETI. In their approach, instead of growing an epitaxial layer of germanium directly on silicon, a graded layer of SiGe is grown with silicon percentage decreasing towards the middle of the waveguide [47]. Also, a silicon top cladding is used. A SEM image can be seen in Fig. 2.15 (b) showing the composition profile of the waveguide. Although the waveguide losses are quite low (1 dB/cm at 4.5 μm), the index contrast becomes low, resulting in waveguide bends on the order of 500 μm meaning that the waveguide circuits will consume a lot of space if complicated circuits are designed.

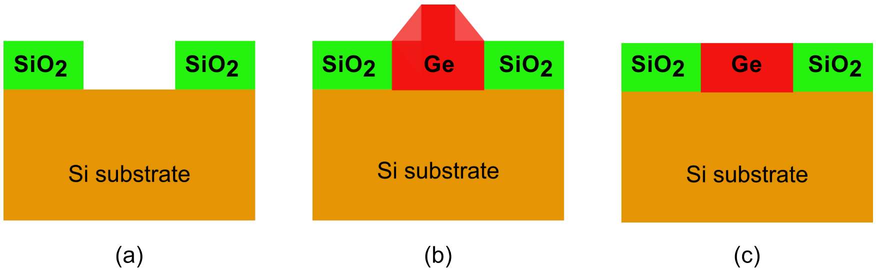

Figure 2.14: *Schematic fabrication diagram of Ge-on-Si waveguide circuits in Si trenches. (a) Trenches are defined in a SiO_2 layer, (b) germanium is overgrown resulting in facets and (c) CMP is performed to polish the waveguide top. The oxide can be removed afterwards if desired (from [46].)*

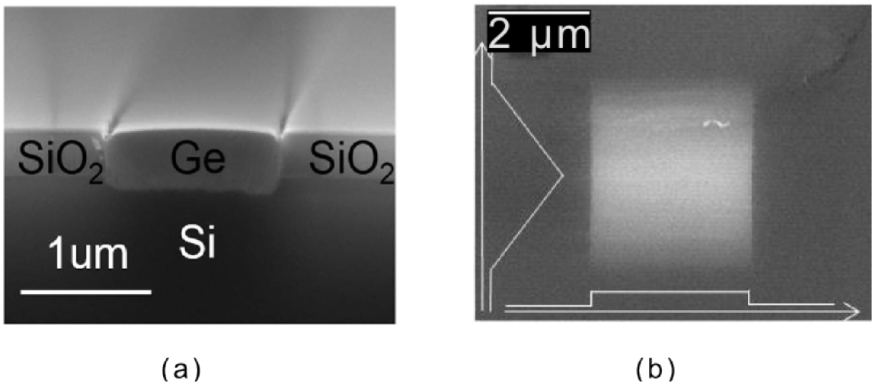

Figure 2.15: *SEM image of (a) germanium film after CMP in SiO_2 trenches (from [46]) and (b) a graded SiGe waveguide along with a composition profile (from [47]).*

Table 2.2 describes the various waveguide platforms discussed above along with the wavelength window of operation, reported waveguide losses and the photonic devices which have been realized on them.

Waveguide Platform	**Operation Window (μm)**	**Reported Waveguide Loss**	**Realized Devices**
SOI	1.2 - 3.8	0.6 dB/cm @ 2.1 μm [6], 0.6 dB/cm @ 3.39 μm [23], 1.8 dB/cm @ 3.8 μm [8], 1.5 dB/cm @ 3.8 μm [48], 2.8 dB/cm @ 3.39 μm [14]	Grating Couplers [6],MMIs,Ring Resonators [8], Cascaded ring resonators [49] , Thermo-optic phase shifters [50], Photonic Crystal Waveguides [51], Angled MMI [52], AWG, PCG [9]
Free Standing Si	1.2 - 8.0	3 dB/cm @ 2.75 μm [15], 27 dB/cm @ 3.39 μm, 36 dB/cm @ 5.2 μm [16], 2.8 dB/cm @ 3.39 μm [14]	Grating Couplers,Ring Resonators [15], [16]
Silicon-on-Sapphire	1.2 - 5.5	4.3 dB/cm @ 4.5 μm [18], 2 dB/cm @ 5.18 μm [19], 4 dB/cm @ 5.5 μm [20]	Grating Couplers [53], Ring Resonators [54], [21], [20], Photonic Crystals [22]
Silicon on porous silicon	1.2 - 8.0	3.9 dB/cm @ 3.39 μm [23]	No realized devices
Silicon Pedestal Waveguide	1.2 - 8.0	2.7 dB/cm @ 3.7 μm [25]	Y Branch Splitters [25]
Silicon Nitride Waveguide	1.2 - 5.0	5.2 dB/cm @ 3.39 μm [26], 2.1 dB/cm @ 3.7 μm [27]	Directional Coupler [27]
Hollow Waveguides	Very wide transmission window	NA	No fabricated devices for mid-infrared wavelengths

Continued on next page

Continued from previous page

Waveguide Platform	**Operation Window (μm)**	**Reported Waveguide Loss**	**Realized Devices**
Chalcogenide based Waveguides	1.0 - 14.0	1.8 dB/cm @ 2.8 μm [36],9.5 dB/cm @ 4.8 μm [34], 0.7 dB/cm @ 5.2 μm [35]	Ring Resonators [35]
Si on CaF_2	1.0 - 8.0	3.8 dB/cm @ 5.2 μm [37]	Ring Resonators [37]
Germanium on Silicon	1.7 - 8.0	6 dB/cm @ 1.9 μm, 2.5 dB/cm @ 3.8 μm [55], 0.6 dB/cm @ 3.8 μm [56], 2.5 dB/cm @ 5.8 μm [44],1 dB/cm @ 4.5 μm, 2 dB/cm @ 7.4 μm [47], 3 dB/cm @ 5.3 μm (this work)	Y junctions, crossings, couplers [47]. MZIs, AWGs, PCGs, Thermo Optic Phase Shifters (this work)

Table 2.2: *Table describing the various waveguide platforms, their transparency windows, reported losses and the realized devices for the mid-infrared wavelength regime.*

2.4 Conclusion

In this chapter, we began by discussing the reasons why SOI has become the preferred waveguide platform for telecom wavelength range applications. We then looked into the possibility of using the SOI waveguide platform in the mid-ir wavelength range and concluded that due to the underlying oxide absorption, it would be challenging to extend the operational wavelength beyond 4 μm. The criteria for alternative waveguide platforms for the mid-ir wavelength range were then defined and it was concluded that while CMOS compatibility of the waveguide platform would enable mass manufacturing, it's equally important to have a simple fabrication flow. Various mid-infrared waveguide platforms along with their fabrication flow, results obtained till date and the limitations associated with them were then discussed. From this discussion because of it's ease of fabrication, wide transparency in the mid-infrared and most importantly CMOS compatibility, Ge-on-Si emerges as a very promising candidate which can take over from the SOI waveguide platform for operation beyond 4 μm wavelength.

References

[1] Laszlo Borka. *Hygroscopic properties of potassium bromide in infrared spectrophotometry.* Analytical Chemistry, 47(7):1212–1213, 1975.

[2] W. Bogaerts G. Roelkens, L. Liu. *Technologies and Building Blocks for On-Chip Optical Interconnects in Integrated Optical Interconnect Architectures for Embedded Systems*, volume XII. Springer New York, 2013.

[3] Graham T Reed, G Mashanovich, FY Gardes, and DJ Thomson. *Silicon optical modulators.* Nature photonics, 4(8):518–526, 2010.

[4] Laurent Vivien, Johann Osmond, Jean-Marc Fédéli, Delphine Marris-Morini, Paul Crozat, Jean-François Damlencourt, Eric Cassan, Y. Lecunff, and Suzanne Laval. *42 GHz p.i.n Germanium photodetector integrated in a silicon-on-insulator waveguide.* Optics Express, 17(8):6252–6257, Apr 2009.

[5] G. Roelkens, J. Van Campenhout, J. Brouckaert, D. Van Thourhout, R. Baets, P. Rojo Romeo, P. Regreny, A. Kazmierczak, C. Seassal, X. Letartre, G. Hollinger, J.M. Fedeli, L. Di Cioccio, and C. Lagahe-Blanchard. *III-V/Si photonics by die-to-wafer bonding.* Materials Today, 10(7-8):36 – 43, 2007.

[6] N. Hattasan, B. Kuyken, F. Leo, E.M.P. Ryckeboer, D. Vermeulen, and G. Roelkens. *High-Efficiency SOI Fiber-to-Chip Grating Couplers and Low-Loss Waveguides for the Short-Wave Infrared.* IEEE Photonics Technology Letters,, 24(17):1536–1538, Sept 2012.

[7] E. Ryckeboer, A. Gassenq, M. Muneeb, N. Hattasan, S. Pathak, L. Cerutti, J.B. Rodriguez, E. Tournié, W. Bogaerts, R. Baets, and G. Roelkens. *Silicon-on-insulator spectrometers with integrated GaInAsSb photodiodes for wide-band spectroscopy from 1510 to 2300 nm.* Optics Express, 21(5):6101–6108, Mar 2013.

[8] Milan M. Milosevic, Milos Nedeljkovic, Taha M. Ben Masaud, Ehsan Jaber-ansary, Harold M. H. Chong, Neil G. Emerson, Graham T. Reed, and Goran Z. Mashanovich. *Silicon waveguides and devices for the mid-infrared.* Applied Physics Letters, 101(12):121105, 2012.

[9] M. Muneeb, X. Chen, P. Verheyen, G. Lepage, S. Pathak, E. Ryckeboer, A. Malik, B. Kuyken, M. Nedeljkovic, J. Van Campenhout, G. Z. Mashanovich, and G. Roelkens. *Demonstration of Silicon-on-insulator mid-infrared spectrometers operating at 3.8 um.* Optics Express, 21(10):11659–11669, May 2013.

[10] Edward D Palik. *Handbook of optical constants of solids*, volume 2. Academic press, 1998.

[11] *http://www.photond.com/products/fimmwave.htm.*

[12] Richard A Soref, Stephen J Emelett, and Walter R Buchwald. *Silicon waveguided components for the long-wave infrared region.* Journal of Optics A: Pure and Applied Optics, 8(10):840, 2006.

[13] Richard Soref. *Mid-infrared photonics in silicon and germanium.* Nature Photonics, 4(8):495–497, 2010.

[14] Jeff Chiles, Saeed Khan, Jichi Ma, and Sasan Fathpour. *High-contrast, all-silicon waveguiding platform for ultra-broadband mid-infrared photonics.* Applied Physics Letters, 103(15):151106, 2013.

[15] Z. Cheng, X. Chen, C. Y. Wong, K. Xu, and H. K. Tsang. *Mid-infrared Suspended Membrane Waveguide and Ring Resonator on Silicon-on-Insulator.* IEEE Photonics Journal, 4(5):1510–1519, Oct 2012.

[16] Y. Xia, C. Qiu, X. Zhang, W. Gao, J. Shu, and Q. Xu. *Suspended Si ring resonator for mid-IR application.* Optics Letters,, 38(7):1122–1124, Apr 2013.

[17] J Soler Penades, C Alonso-Ramos, AZ Khokhar, M Nedeljkovic, LA Boodhoo, A Ortega-Monux, I Molina-Fernandez, P Cheben, and GZ Mashanovich. *Suspended SOI waveguide with sub-wavelength grating cladding for mid-infrared.* Optics letters, 39(19):5661–5664, 2014.

[18] Tom Baehr-Jones, Alexander Spott, Rob Ilic, Andrew Spott, Boyan Penkov, William Asher, and Michael Hochberg. *Silicon-on-sapphire integrated waveguides for the mid-infrared.* Optics Express, 18(12):12127–12135, Jun 2010.

[19] Fangxin Li, Stuart D. Jackson, Christian Grillet, Eric Magi, Darren Hudson, Steven J. Madden, Yashodhan Moghe, Christopher O'Brien, Andrew Read, Steven G. Duvall, Peter Atanackovic, Benjamin J. Eggleton, and David J. Moss. *Low propagation loss silicon-on-sapphire waveguides for the mid-infrared.* Optics Express, 19(16):15212–15220, Aug 2011.

[20] Alexander Spott, Yang Liu, Tom Baehr-Jones, Rob Ilic, and Michael Hochberg. *Silicon waveguides and ring resonators at 5.5 um.* Applied Physics Letters, 97(21):213501, 2010.

[21] Raji Shankar, Irfan Bulu, and Marko Loncar. *Integrated high-quality factor silicon-on-sapphire ring resonators for the mid-infrared.* Applied Physics Letters, 102(5):051108, 2013.

[22] Raji Shankar and Marko Lončar. *Silicon photonic devices for mid-infrared applications.* Nanophotonics, 3(4-5):329–341.

[23] Goran Z. Mashanovich, Milan M. Milošević, Milos Nedeljkovic, Nathan Owens, Boqian Xiong, Ee Jin Teo, and Youfang Hu. *Low loss silicon waveguides for the mid-infrared.* Optics Express, 19(8):7112–7119, Apr 2011.

[24] L. Pavesi. *Porous silicon dielectric multilayers and microcavities.* La Rivista del Nuovo Cimento, 20(10):1–76, 1997.

[25] Pao Tai Lin, Vivek Singh, Yan Cai, Lionel C. Kimerling, and Anu Agarwal. *Air-clad silicon pedestal structures for broadband mid-infrared microphotonics.* Optics Letters, 38(7):1031–1033, Apr 2013.

[26] Saeed Khan, Jeff Chiles, Jichi Ma, and Sasan Fathpour. *Silicon-on-nitride waveguides for mid- and near-infrared integrated photonics.* Applied Physics Letters, 102(12):121104, 2013.

[27] Pao Tai Lin, Vivek Singh, Lionel Kimerling, and Anuradha Murthy Agarwal. *Planar silicon nitride mid-infrared devices.* Applied Physics Letters, 102(25):–, 2013.

[28] E. A. Taft. *Characterization of Silicon Nitride Films.* Journal of Electrochemical Society, 118(8):1341–1346, 1971.

[29] W. A. Lanford and M. J. Rand. *The hydrogen content of plasma deposited silicon nitride.* Journal of Applied Physics, 49(4):2473–2477, 1978.

[30] PengYuan Yang, Stevan Stankovic, Jasna Crnjanski, EeJin Teo, David Thomson, AndrewA. Bettiol, MarkB.H. Breese, William Headley, Cristina Giusca, GrahamT. Reed, and GoranZ. Mashanovich. *Silicon photonic waveguides for mid- and long-wave infrared region.* Journal of Materials Science: Materials in Electronics, 20(1):159–163, 2009.

[31] John P Barber, Donald B Conkey, Jeffrey Ryan Lee, Neal B Hubbard, Larry L Howell, Dongliang Yin, Holger Schmidt, and Aaron R Hawkins. *Fabrication of hollow waveguides with sacrificial aluminum cores.* IEEE Photonics Technology Letters, 17(2):363–365, 2005.

[32] Dongliang Yin, John Barber, Aaron Hawkins, and Holger Schmidt. *Waveguide loss optimization in hollow-core ARROW waveguides.* Optics express, 13(23):9331–9336, 2005.

[33] Benjamin J Eggleton, Barry Luther-Davies, and Kathleen Richardson. *Chalcogenide photonics.* Nature Photonics, 5(3):141–148, 2011.

[34] Candice Tsay, Elvis Mujagić, Christi K. Madsen, Claire F. Gmachl, and Craig B. Arnold. *Mid-infrared characterization of solution-processed As2S3 chalcogenide glass waveguides.* Optics Express, 18(15):15523–15530, Jul 2010.

[35] Hongtao Lin, Lan Li, Yi Zou, Sylvain Danto, J. David Musgraves, Kathleen Richardson, Stephen Kozacik, Maciej Murakowski, Dennis Prather, Pao T. Lin, Vivek Singh, Anu Agarwal, Lionel C. Kimerling, and Juejun Hu. *Demonstration of high-Q mid-infrared chalcogenide glass-on-silicon resonators.* Optics Letters, 38(9):1470–1472, May 2013.

[36] Yunlai Zha, Pao Tai Lin, Lionel Kimerling, Anu Agarwal, and Craig B. Arnold. *Inverted-Rib Chalcogenide Waveguides by Solution Process.* ACS Photonics, 1(3):153–157, 2014.

[37] Yu Chen, Hongtao Lin, Juejun Hu, and Mo Li. *Heterogeneously integrated silicon photonics for the mid-infrared and spectroscopic sensing.* ACS nano, 8(7):6955–6961, 2014.

[38] Matthew A. Meitl, Zheng-Tao Zhu, Vipan Kumar, Keon Jae Lee, Xue Feng, Yonggang Y. Huang, Ilesanmi Adesida, Ralph G. Nuzzo, and John A. Rogers. *Transfer printing by kinetic control of adhesion to an elastomeric stamp.* Nature Materials, 5(1):33–38, 2006.

[39] Afshin Ghaffari, Amir Hosseini, Xiaochuan Xu, David Kwong, Harish Subbaraman, and Ray T. Chen. *Transfer of micro and nano-photonic silicon nanomembrane waveguide devices on flexible substrates.* Optics Express, 18(19):20086–20095, Sep 2010.

[40] Richard Soref, Joshua Hendrickson, and Justin W. Cleary. *Mid- to long-wavelength infrared plasmonic-photonics using heavily doped n-Ge/Ge and n-GeSn/GeSn heterostructures.* Optics Express, 20(4):3814–3824, Feb 2012.

[41] Jianwei Mu, Richard Soref, Lionel C. Kimerling, and Jurgen Michel. *Silicon-on-nitride structures for mid-infrared gap-plasmon waveguiding.* Applied Physics Letters, 104(3):031115, Jan 2014.

[42] Stefan Alexander Maier. *Plasmonics: Fundamentals and Applications*, volume XXV. Springer, 2007.

[43] Richard Soref, Robert E. Peale, and Walter Buchwald. *Longwave plasmonics on doped silicon and silicides.* Optics Express, 16(9):6507–6514, Apr 2008.

[44] Yu-Chi Chang, Vincent Paeder, Lubos Hvozdara, Jean-Michel Hartmann, and Hans Peter Herzig. *Low-loss germanium strip waveguides on silicon for the mid-infrared.* Optics Letters, 37(14):2883–2885, Jul 2012.

[45] Roger Loo, Gang Wang, Laurent Souriau, JC Lin, Shotaro Takeuchi, Guy Brammertz, and Matty Caymax. *High quality Ge virtual substrates on Si wafers with standard STI patterning.* Journal of The Electrochemical Society, 157(1):H13–H21, 2010.

[46] Yan Cai, Wei Yu, Lionel C Kimerling, and Jurgen Michel. *Chemical Mechanical Polishing of Selective Epitaxial Grown Germanium on Silicon.* ECS Journal of Solid State Science and Technology, 3(2):P5–P9, 2014.

[47] Mickael Brun, Pierre Labeye, Gilles Grand, Jean-Michel Hartmann, Fahem Boulila, Mathieu Carras, and Sergio Nicoletti. *Low loss SiGe graded index waveguides for mid-IR applications.* Optics Express, 22(1):508–518, Jan 2014.

[48] M. Nedeljkovic, A. Z. Khokhar, Y. Hu, X. Chen, J. Soler Penades, S. Stankovic, H. M. H. Chong, D. J. Thomson, F. Y. Gardes, G. T. Reed, and G. Z. Mashanovich. *Silicon photonic devices and platforms for the mid-infrared.* Opt. Mater. Express, 3(9):1205–1214, Sep 2013.

[49] Benedetto Troia, Ali Z Khokhar, Milos Nedeljkovic, Jordi Soler Penades, Vittorio Passaro, and Goran Z Mashanovich. *Cascade-coupled racetrack resonators based on the Vernier effect in the mid-infrared.* Optics express, 22(20):23990–24003, 2014.

[50] Milos Nedeljkovic, Stevan Stankovic, Colin J Mitchell, Ali Z Khokhar, Scott A Reynolds, David J Thomson, Frederic Y Gardes, Callum G Littlejohns, Graham T Reed, and Goran Z Mashanovich. *Mid-infrared thermo-optic modulators in SoI.* IEEE Photonics Technology Letters, 26(13):1352–1355, 2014.

[51] Christian Reimer, Milos Nedeljkovic, David J. M. Stothard, Matthieu O. S. Esnault, Christopher Reardon, Liam O'Faolain, Malcolm Dunn, Goran Z. Mashanovich, and Thomas F. Krauss. *Mid-infrared photonic crystal waveguides in silicon.* Optics Express, 20(28):29361–29368, Dec 2012.

[52] Y Hu, T Li, DJ Thomson, X Chen, J Soler Penades, AZ Khokhar, CJ Mitchell, GT Reed, and GZ Mashanovich. *Mid-infrared wavelength division (de) multiplexer using an interleaved angled multimode interferometer on the silicon-on-insulator platform.* Optics letters, 39(6):1406–1409, 2014.

[53] Zhenzhou Cheng, Xia Chen, C.Y. Wong, Ke Xu, C.K.Y. Fung, Y.M. Chen, and Hon-Ki Tsang. *Mid-Infrared Grating Couplers for Silicon-on-Sapphire Waveguides.* IEEE Photonics Journal, 4(1):104–113, Feb 2012.

[54] C. Y. Wong, Z. Cheng, X. Chen, K. Xu, C. K. Y. Fung, Y. M. Chen, and H. K. Tsang. *Characterization of Mid-Infrared Silicon-on-Sapphire Microring Resonators With Thermal Tuning.* IEEE Photonics Journal, 4(4):1095–1102, Aug 2012.

[55] Li Shen, Noel Healy, Colin J. Mitchell, Jordi Soler Penades, Milos Nedeljkovic, Goran Z. Mashanovich, and Anna C. Peacock. *Mid-infrared*

all-optical modulation in low-loss germanium-on-silicon waveguides. Opt. Lett., 40(2):268–271, Jan 2015.

[56] M. Nedeljkovic, J. Soler Penades, C. Mitchell, A. Khokhar, S. Stankovic, T. Dominguez Bucio, C. Littlejohns, F. Gardes, and G. Mashanovich. *Surface Grating Coupled Low Loss Ge-on-Si Rib Waveguides and Multimode Interferometers.* Photonics Technology Letters, IEEE, PP(99):1–1, 2015.

3

Ge-on-Si Waveguide Platform

“When it is obvious that the goals cannot be reached, don’t adjust the goals, adjust the action steps."

– Confucius

3.1 Introduction

We saw in the previous chapter that the Ge-on-Si waveguide platform has interesting properties which makes it very attractive for application in the mid-infrared wavelength range. In this chapter, we will begin by having a look at the optical characteristics of the Ge-on-Si platform and then discuss in detail the fabrication flow which was developed in this thesis.

3.2 Silicon & Germanium optical characteristics

Both silicon and germanium are chemical elements found in the fourth group of the periodic table with atomic numbers 14 and 32 respectively and have four valence electrons in their outer shell. Silicon was first prepared by Berzelius in 1823 and is the second most abundant element in the earth's crust. The existence of germanium was first predicted by Dmitri Ivanovich Mendeleev to fill in the gap between silicon and tin. Mendeleev called it ekasilicon. Germanium was finally discovered in 1885 by Clemens Winkler who named the element in the honor of his homeland, Germany. Isolated silicon and germanium are semiconductors and are heavily used in electronic industry. The very first transistors were built on germanium. However silicon soon took over semiconductor industry because of the excellent and stable oxide it possesses. Another major reason for switching from germanium to silicon was that since germanium has a lower bandgap (0.67 eV as compared to 1.12 eV of silicon) the leakage currents are much higher. Today however germanium transistors are being pursued again because of the higher mobility of carriers and a major area of focus is SiGe devices which provide best of both materials.

We will keep our focus on the optical characteristics of germanium and silicon. We first begin by having a look at the refractive indices of these materials as a function of wavelength at different temperatures. This is shown in Fig 3.1 (a) and (b) [5]. It can be seen that germanium has a higher refractive index than that of silicon and thus a waveguide can be constructed using these two materials using germanium as the waveguide core. As mentioned above, both of these materials are semiconductors. Semiconductors are usually doped with atoms of other materials having either fewer or extra electrons in their outer shell in order to change the electrical properties of the semiconductor. These atoms create carriers which are free to move within the band. A free carrier (electron or hole) can absorb light and be excited to a higher state within the same band. This phenomenon is called free carrier absorption (FCA) and is an important source of loss especially in the mid-infrared. The free carrier absorption for both n and p doped silicon and germanium is shown in Fig 3.1 (c) [1],(d) [2],(e) [3] and (f) [4]. FCA is directly proportional to the level of doping and scales roughly quadrati-

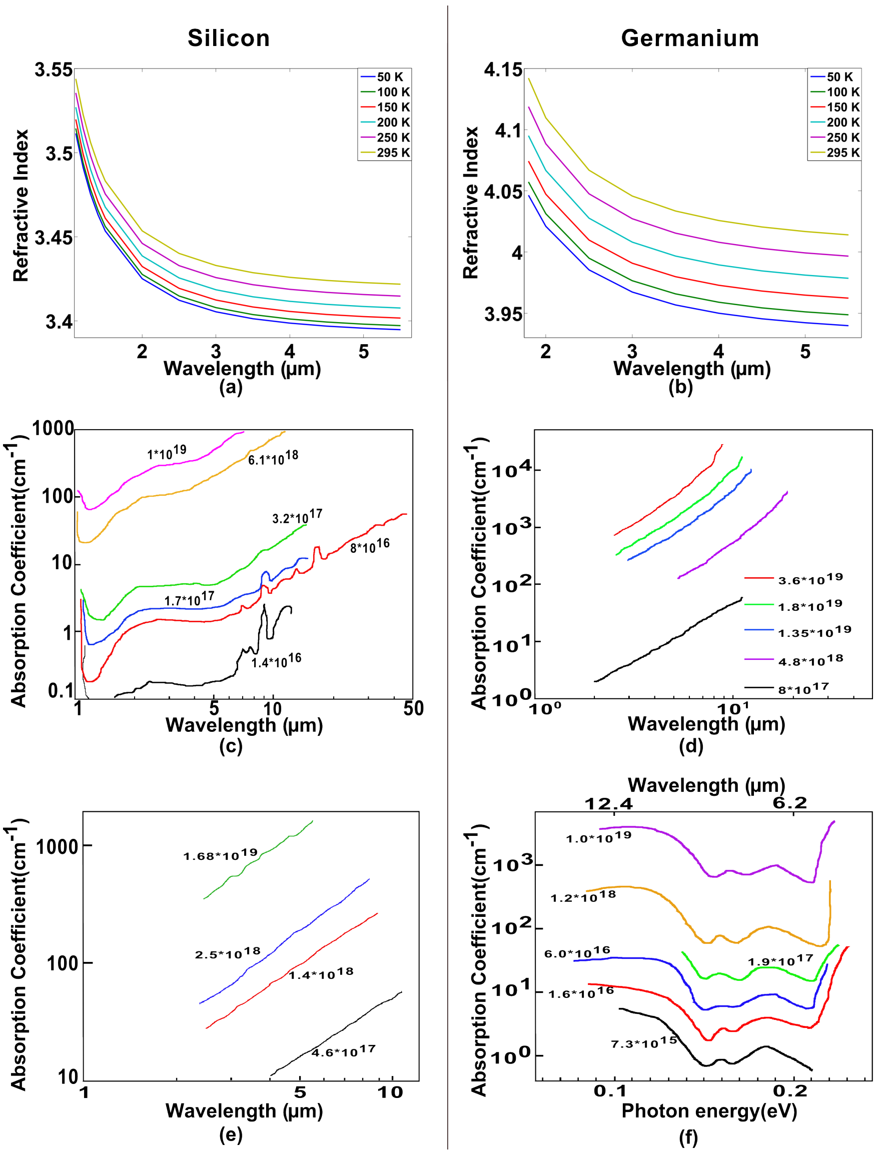

Figure 3.1: Refractive index of (a) silicon and (b) germanium as a function of wavelength at different temperatures. FCA absorption for (c) n doped silicon [1], (d) n doped germanium [2], (e) p doped silicon [3], (f) p doped germanium [4]

cally with wavelength. This means that for low loss waveguides, we should keep the doping levels as low as possible. Since the goal of this thesis was to evaluate the Ge-on-Si waveguide platform for the mid-infrared wavelength range, we didn't carry out any intentional doping. However to realize devices which can operate at high speed (such as switches, modulators), dopants could be introduced in a standard CMOS pilot line as per the requirements.

3.3 Fabrication flow for Ge-on-Si waveguides

The fabrication flow of the Ge-on-Si waveguides is schematically described in Fig 3.2. We will analyze each of the steps in detail below.

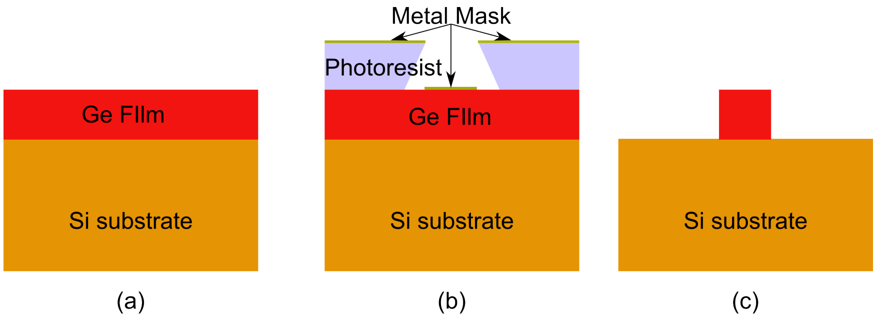

Figure 3.2: *Fabrication flow for Ge-on-Si integrated photonic circuits. (a) Epitaxial growth of germanium film on a Si (100) 200 mm substrate, (b) metal mask definition using i-line contact lithography and lift-off and (c) dry etching of germanium film and removal of metal mask.*

3.3.1 Epitaxial Growth

The first step in the fabrication flow is the epitaxial growth of germanium on a 200 mm silicon wafer which is carried out in a 200 mm CMOS pilot line in imec. There is a difference of 4.2% between the lattice constants of silicon and germanium. The epitaxial growth of films with lattice constants different than that of the substrate is classified in three categories (a) island growth (Volmer - Weber) (b) layer growth (Frank - Van der Merwe) and (c) a combination of island and layer (Stranski-Krastanov) [6]. Island growth happens when the atoms of the deposited film are more strongly bound to each other than to the substrate while for layer growth it's vice-versa. The Stranski-Krastanov (SK) mechanism is a mixture of island and layer growth and in this case after forming a couple of monolayers the subsequent layer growth becomes unfavorable because of the overall surface tension and islands form. Germanium epitaxial growth on silicon substrates has been widely studied in microelectronics industry and it has been known that it occurs because of the SK mechanism. As described above, free carrier absorption is directly proportional to the doping. Therefore to keep the free carrier absorption losses to minimum, we chose the wafers with lowest possible doping available. The silicon wafers had a background n-type doping of 5×10^{14} cm^{-3}. Germanium growth is carried out on this low doped silicon substrate at 450°C by atmospheric chemical vapor deposition. GeH_4 (1 % in H_2) is used as a Ge precursor. No additional dopant is introduced at the time of germanium film growth. The temperature of 450°C is chosen because it suppresses the islands which are formed during the germanium layer growth. This grown germanium film has a major issue associated with it. The lattice mismatch between silicon and germanium introduces threading dislocations (TD) at the silicon-germanium interface which will cause absorption of light and hence increase waveguide loss. To reduce the number of defects, the wafers are annealed at 850°C in N_2 for three minutes. This annealing is a thermally activated process following an Arrhenius law and increases the glide speed of the TD. The grown germanium film has a threading dislocation density (TDD) of 2×10^{10} cm^{-2} while the annealed film has TDD of 4×10^7 cm^{-2} [7]. Since we are working in the mid-infrared wavelength range, a minimum thickness of germanium has to be grown in order to support an optical mode. We chose a thickness of 2 μm (the details behind this choice will be explained in the next chapter).

3.3.2 Lithography and Dry etching

Lithography and dry etching are used to realize desired patterns with precision on the semiconductor substrates. The concept of lithography is simple enough; a light sensitive organic polymer (called photoresist) is spin coated on the surface forming a thin layer. This resist is then exposed selectively by shining light through a mask which contains the desired pattern. The exposed resist is developed in a basic solution diluted with water. After development the pattern from the mask is transferred to the photoresist on top of the semiconductor substrate. To realize an optical waveguide, we now desire to transfer this pattern on the thin film itself. This can be achieved by selectively removing the thin film by etching it using a mask. There are two important aspects of etching. The first is the selectivity towards the mask. A good etchant will etch the material at a rapid rate as compared with the mask. Failure to do so will result in a situation where all the mask has been etched and the material has not been etched completely. The second is the directionality of the etch which is decided by the type of environment used for etching. Etching can be done in either a "wet" or a "dry" environment. Wet etching involves the use of liquid etchants which work through chemical processes and therefore result mostly in smooth side walls. These etchants can also be made very selective however a major issue associated with them is that the etching profile is typically isotropic i.e. there is no directionality (although there are some etchants e.g. KOH which etches Si only along a particular crystal plane). This isotropic etching means that the areas below the mask will also get etched and therefore the final pattern will have a much smaller width as compared to that of the mask. This can create serious issues in case of (photonic) integrated circuits as the final structures will be further apart from each other than intended, downgrading the device performance. To avoid these problems, plasma etching systems are used in modern day CMOS pilot lines. A plasma etching system consists of two electrodes across which high electric field generated by a RF generator operating at 13.56 MHz is applied. A mixture of gases is filled between these electrodes and some of the gas ions are ionized producing free ions and electrons, thus creating a plasma. Due to the difference in the mobilities of electrons and ions, during the first few cycles more electrons are collected near the electrodes and hence a voltage bias develops between the plasma and the electrodes. If both the electrodes have the same area then the voltage drop on the electrode itself would be zero meaning no etching would occur. Therefore, one of the electrodes is made smaller in area which results in a large voltage drop across it (because the current density must be higher at smaller electrode to maintain continuity throughout the system).

There are two etching mechanisms in a plasma system. The free radicals present in the gas mixture contribute to the chemical etching of materials. Free radicals are electrically neutral species that have incomplete bonds which makes them highly chemically reactive. The free radicals in the plasma react with the material to be etched and the byproduct is a volatile species that leaves the surface. The chemical processes as described above produce an isotropic profile which is undesired. The ions present in the plasma cause physical etching of the material. Due to the voltage difference between electrodes as described above, the positive ions are accelerated towards the wafer surface causing etching by physical sputtering resulting in an anisotropic etch profile.

In practice what happens is that the ions and the free radicals which are present in the plasma do not act independently from each other. The chemical components and the physical components work complimentary to each other to etch the material. It has been proposed that the ion bombardment enhances one of the steps (surface adsorption, removal of byproduct etc.) of the chemical process. As a result of this, both good selectivity with respect to the mask and directionality are obtained. As explained above, the ions are accelerated in between the electrodes hence a large voltage bias is desired to achieve sufficient acceleration which results in directional profiles. Another very important parameter to achieve directionality is the pressure of the gases in the chamber. A lower pressure means ions undergo less collisions among themselves and are directed towards the surface to be etched. A rule of thumb which can therefore be applied to achieve highly anisotropic profiles is to operate the etching sys-

tem at high power and low pressure.
After presenting a brief overview of the basics associated with lithography and the dry etching, let's have a closer look at the strategies undertaken for realizing Ge-on-Si photonic integrated circuits. Due to the reasons explained above, we will be carrying out dry etching of the 2 μm thick germanium film in a reactive ion etching (RIE) system. Therefore we begin by doing a literature review of the dry etching conditions needed to produce an anisotropic profile for germanium films. A review of selective etching of germanium over silicon is presented in [8] where various gases like a mixture of CF_4 and O_2, CF_2Cl_2 and CF_3Br were used at different pressure and power to etch germanium films. The RIE power used in [8] was kept at 200 W and it was observed that although fluorine based plasma can etch germanium selectively over silicon, it can't achieve directional etching. Cl_2 has been used to pattern a film of 310 nm thick germanium film highly anisotropically using a metal Ti mask [9]. Another approach to achieve an anisotropic etch profile using HBr has been discussed in [10] where an ICP system was used at a power of 800 W. A 40:10 mixture of CF_4 and O_2 was used also in [11] to pattern 100 nm germanium films.
As can be deducted from the discussion above, the studies on germanium etching limit themselves to films of thicknesses of the order of hundreds of nanometers. A new etch recipe therefore needed to be developed for etching of 2 μm germanium films. Since we only had access to a RIE system with fluorine based gases (CF_4 and SF_6), they were the main focus of study. For SF_6, it was found that the selectivity between germanium and silicon is close to one and hence both the materials get etched. Moreover as can be seen in Fig. 3.3(a), there is a large amount of undercut below the mask while using a SF_6 plasma at a power of 200 W and pressure of 30 mtorr. Adjustments in power and pressure didn't improve this undercut and hence SF_6 etching was not pursued further. As discussed in [8] and [11], germanium can be etched selectively with respect to silicon in a CF_4:O_2 plasma. The reason behind this is that the activation energy for the Ge-Fluorine etching reaction is lower than that of the Si-Fluorine etching reaction. The addition of O_2 to the plasma helps in oxidizing the germanium surface. Germanium is more easily oxidized than silicon and the GeO_xF_y layer is more reactive than a SiO_xF_y layer, resulting in higher selectivity.

We started to optimize the etching recipe by choosing a mixture of 40:20 of the CF_4:O_2 plasma at a pressure of 50 mtorr and a power of 100 W as described in [11]. Although the side walls were smooth, it was found that there is huge undercut below the mask (the mask was 1.75 μm wide and has been removed) as can be seen in Fig 3.3(b). As discussed in the beginning of this section that lower pressure and higher powers result in anisotropic profiles, we optimized the pressure of the RIE chamber to be 10 mtorr and the power to be 600 W (which is the limit of our RIE system) and the etching rate of germanium was

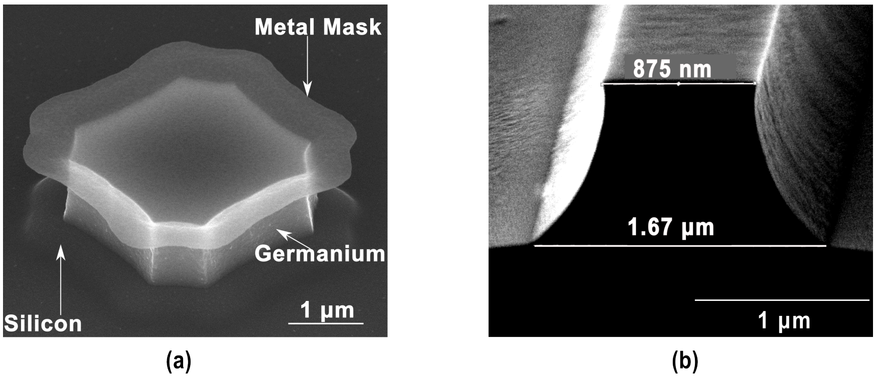

Figure 3.3: *SEM image showing germanium etching profile in (a) SF_6 plasma at a power of 200 W and pressure 30 mtorr and (b) CF_4:O_2 plasma of 40:20 composition at a power of 100 W and pressure of 50 mtorr.*

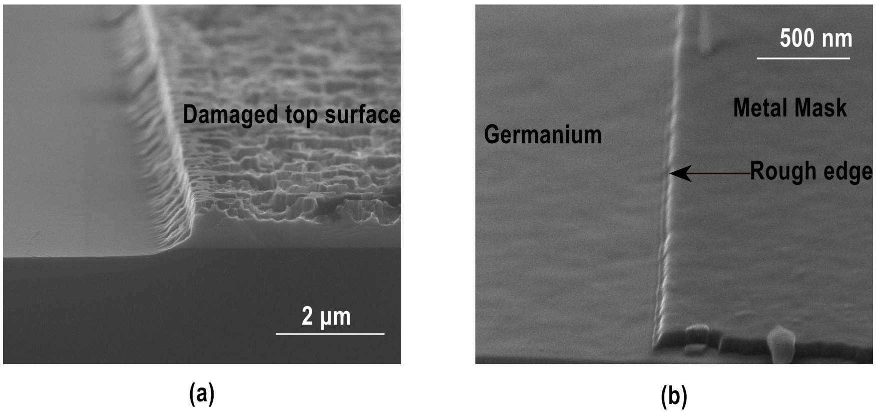

Figure 3.4: *SEM image showing (a) damaged top surface of a germanium waveguide patterned using a photoresist mask and (b) the side wall roughness which is introduced in the metal mask while doing lift-off.*

found to be 130 nm/min while that of underlying silicon substrate was found to be 30 nm/min. In the beginning, we were using a photoresist mask. However as seen in Fig. 3.4(a), it was found that this photoresist mask eroded completely before fully etching the germanium film in the plasma at such high powers and therefore the top of the waveguide was also etched. A usual option is to utilize a hard mask consisting of either PECVD SiO_x or SiN_x. The etching rates of these dielectric masks is about 300 nm/min in the developed etching recipe which means that we will need a very thick masking layer, patterning which in itself would be a big challenge. We therefore decided to opt for a Ti/Cr mask

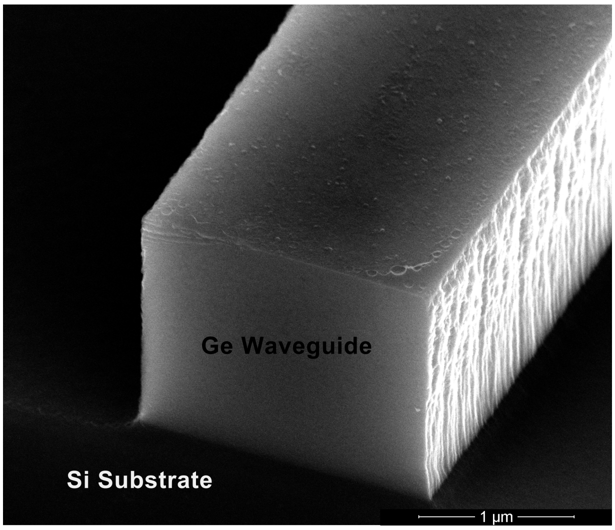

Figure 3.5: *Cleaved facet of a Ge-on-Si waveguide etched in a CF_4:O_2 plasma in 40:10 ratio at a power of 600 W and pressure 10 mtorr. The metal mask has been removed using HF.*

which was patterned using a lift-off technique. A disadvantage of this technique was that the liftoff introduced a roughness on the metal film which can be seen in Fig 3.4(b). This roughness was then transferred to the waveguide circuits as can be seen in Fig 3.5. However we will see in next chapter that this side wall roughness doesn't affect our device operation considerably. After dry etching, the metal mask was removed by putting it in an HF solution which dissolves Ti and removes the top Cr layer as well. The samples were then thinned down and cleaved at the desired location.

3.3.2.1 Routes to improve dry etching

There are many strategies which could be used to improve dry etching such that the side wall roughness of the waveguides is reduced. As discussed previously, the roughness from the metal mask defined via lift-off is transferred to the waveguides and hence replacing the metal mask by either a photoresist or a dielectric mask would be desirable. The first way could be to reduce the amount of O_2 in the CF_4 plasma which would reduce the removal rate of a photoresist mask and introduce a side wall passivator like H_2. Another possibility would be to use a CHF_3:O_2 plasma where H atoms would be produced during ionization. Third possibility is to use a CF_4 plasma to break through the native oxide formed on the germanium surface and then use a Cl_2:N_2 plasma in ICP. The Cl_2 plasma etches the germanium while N_2 increases the side wall passivation by polymer formation [12].

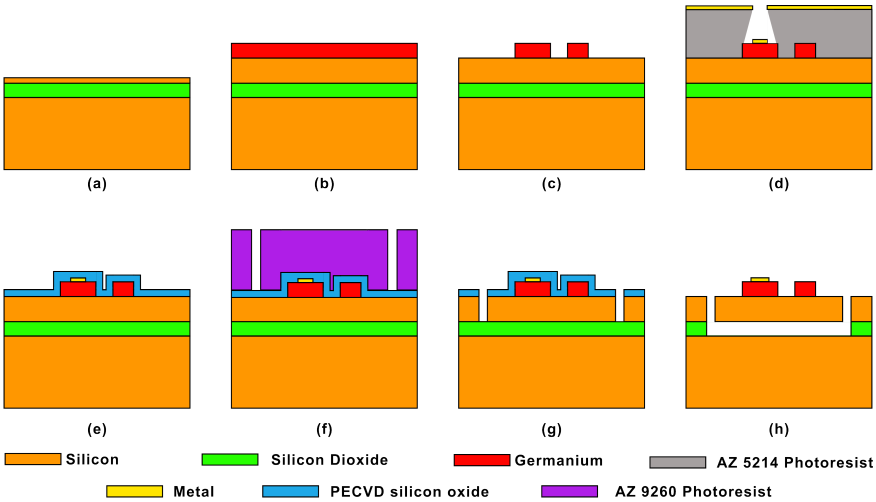

Figure 3.6: *Schematic fabrication scheme of Ge-on-SOI phase shifters (a) 200 mm SOI wafer with 220 nm silicon layer, (b) epitaxial growth of 3 μm thick silicon and 2 μm thick germanium layers, (c) waveguide definition by lift-off and dry etching, (d) lithography and metal deposition, (e) PECVD oxide deposition, (f) lithography for defining trenches, (g) dry etching of PECVD silicon oxide and silicon and (h) removal of PECVD oxide and buried oxide by HF dip*

3.4 Ge-on-SOI

As we will see later in chapter 5, instead of growing germanium films on a silicon substrate, we also grew them on SOI for realizing efficient thermo-optic phase shifters. The fabrication scheme of the Ge-on-SOI phase shifters is described schematically in Fig. 3.6. We began with a 200 mm SOI wafer with 220 nm silicon thickness which received an IMEC-clean [13]. 3 μm of silicon was then grown epitaxially in a horizontal, cold wall, load lock reactor (ASM Epsilon 2000). The in-situ bake at 1050°C removed all traces of oxygen. The silicon layer was grown at a temperature of 1050°C using dichlorosilane as silicon precursor and H_2 as carrier gas. The germanium layer was grown at 450°C using germane as precursor and H_2 as carrier gas. The wafer was then annealed at 800° C for three minutes to reduce threading dislocation density. The germanium waveguide and heater were defined using a metal mask which was patterned using i-line lithography and lift-off as described for Ge-on-Si waveguides. Germanium etching was carried out in CF_4:O_2 plasma and the metal was removed by a HF dip. Metal lines on top of the germanium heaters were defined using a second lithography step and liftoff. Trenches were then defined in the silicon substrate using lithography and dry etching in a SF_6:O_2 plasma. The samples were then thinned and cleaved. To achieve even better thermal isolation samples were put in HF to remove the underlying SiO_2. SEM images showing a Ge-on-SOI heater waveguide and heater can be seen in Fig. 3.7.

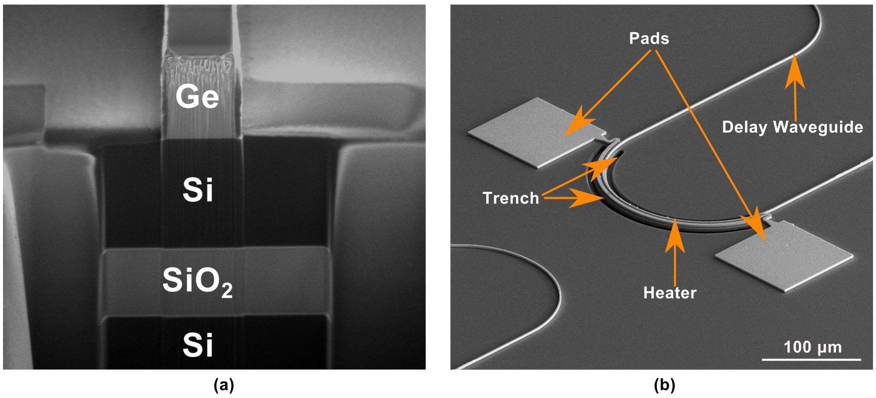

Figure 3.7: *SEM image showing the (a) cross section of a Ge-on-SOI waveguide and (b) the top view of an undercut heater implemented in one arm of a MZI.*

3.5 Conclusion

In this chapter, we started by having a look at the optical characteristics i.e. the refractive index and FCA absorption in Si and Ge. As Ge has a higher index than silicon, an optical waveguide can thus be constructed using a germanium core. We then discussed briefly the germanium growth carried out in imec and followed it with a discussion on the possible routes to define germanium-on-silicon waveguide circuits in our cleanroom. It was found that although one desires a dielectric or a photoresist mask to define waveguide circuits, in order to reduce side wall roughness, it's not possible to do so with the current dry etching recipe. Few guidelines are provided how this issue can be tackled in the future. In conclusion, the fabrication scheme can still be optimized in terms of minimum feature size and side wall roughness, doing which would be straight forward in a standard CMOS fab with access to Deep UV lithography tools and dedicated ICP etching systems. Finally we introduced a slightly modified version of this waveguide platform namely germanium-on-silicon-on-insulator. This waveguide platform required the additional growth of a silicon layer in the current fabrication scheme but this can also be avoided by using a SOI with thicker silicon device layer. The fabrication scheme for such waveguides can also be transfered to a CMOS fab for higher quality.

References

[1] W. Spitzer and H. Y. Fan. *Infrared Absorption in n-Type Silicon.* Physical Review, 108:268–271, Oct 1957.

[2] V.I Fistul. *Heavy Doped Semiconductors.* Nauka (In Russian), 1967.

[3] H. Hara and Y. Nishi. *Free Carrier Absorption in p-Type Silicon.* Journal of the Physical Society of Japan, 21:1222, June 1966.

[4] Ju I. Ukhanov. *Optical Properties of Semiconductors.* Nauka (In Russian), 1977.

[5] Edward D Palik. *Handbook of optical constants of solids*, volume 2. Academic press, 1998.

[6] E. Schulz. *Nucleation and growth of thin films. Von B. LEWIS und J. C. ANDERSON. London/New York/San Francisco: Academic Press 1978. 506 S.* Acta Polymerica, 31(3):216–216, 1980.

[7] Roger Loo, Gang Wang, Laurent Souriau, JC Lin, Shotaro Takeuchi, Guy Brammertz, and Matty Caymax. *High quality Ge virtual substrates on Si wafers with standard STI patterning.* Journal of The Electrochemical Society, 157(1):H13–H21, 2010.

[8] GS Oehrlein, TD Bestwick, PL Jones, MA Jaso, and JL Lindström. *Selective dry etching of germanium with respect to silicon and vice versa.* Journal of The Electrochemical Society, 138(5):1443–1452, 1991.

[9] Magnus Lindblom, Julia Reinspach, Olov von Hofsten, Michael Bertilson, Hans M. Hertz, and Anders Holmberg. *High-aspect-ratio germanium zone plates fabricated by reactive ion etching in chlorine.* Journal of Vacuum Science & Technology B, 27(2):L1–L3, 2009.

[10] G Woehl, M Oehme, C Parry, E Kasper, M Jutzi, M Berroth, and E Voorneman. *Special etch technologies for Ge/Si devices.* In Proceedings of the third international conference on SiGe (C) epitaxy and heterostructures, pages 77–9, 2003.

[11] B. Ramanamurthy, N. Balasubramanian, S. Balakumar, M. Mukherjeeroy, A. Trigg, R. Kumar, and D. Kwong. *Localized germanium-on-insulator patterns on Si by novel etching scheme in CF4/O2 plasma.* Thin Solid Films, 504:77–80, May 2006.

[12] Marcelo SB Castro, Sebastien Barnola, and Barbara Glück. *Selective and Anisotropic Dry Etching of Ge over Si.* Journal of Integrated Circuits and Systems, 8(2):104–109, 2013.

[13] M. Meuris, S. Arnauts, I Cornelissen, K. Kenis, M. Lux, S. DeGendt, P. Mertens, I Teerlinck, R. Vos, L. Loewenstein, M.M. Heyns, and K. Wolke. *Implementation of the IMEC-Clean in advanced CMOS manufacturing*. In 1999 IEEE International Symposium on Semiconductor Manufacturing Conference Proceedings,, pages 157–160, 1999.

4

Ge-on-Si Passive Photonic Integrated Circuits

“Strength does not come from winning. Your struggles develop your strengths. When you go through hardships and decide not to surrender, that is strength."

– Arnold Schwarzenegger

4.1 Introduction

In this chapter we will describe the passive photonic integrated circuits which were simulated and measured in this thesis. The simulations were performed using both in-house written and commercially available tools. The fabricated PICs were characterized on a measurement system which was assembled during the course of this thesis and we will begin by discussing the challenges faced and the specifications of the measurement system.

4.2 Measurement System

Measurement systems to characterize near-infrared PICs consist usually of a source and a detector with the PIC in between. The source can be either a broad-band LED or a tunable laser and is connected to silica fibers. The silica fiber can either be polarization maintaining or the desired polarization can be chosen by applying torque to the fiber. For coupling light in the PIC, either a vertical or a horizontal coupling scheme is used [1]. In vertical coupling, the fiber is positioned above a grating coupler on the PIC and light in the fundamental mode of the fiber couples into the fundamental mode of the waveguide circuit. A one dimensional grating coupler typically is polarization selective. In the horizontal coupling scheme, light is coupled from the fiber to the facet of the waveguide. To ensure good coupling, the mode field diameters in the waveguide and in the fiber are made similar in size. This is achieved by using a lensed fiber and by tapering the waveguide.
The well developed field of telecom photonics has enabled the realization of plug and play sources and detectors in addition to the availability of cheap and robust fibers. However as mid-infrared photonics is still a young field, one faces the following challenges in assembling a measurement system for the mid-infrared wavelength range.

- **Optical fibers:** Silica fibers provide an economical, widely transparent and robust solution for the needs of telecommunication networks. However they are not transparent for wavelengths beyond 2.4 μm and hence alternate solutions are required. There are fibers transparent in the mid-infrared wavelength range which are either made of chalcogenide [2] or fluoride glasses [3]. In addition to being expensive, these fibers are fragile when compared to silica fibers and are difficult to cleave requiring an ultrasonic cleaver to produce a flat facet. Moreover these fibers contain protective coatings whose removal is involved and typically requires the use of solvents such as dichloromethane.

- **Polarization Control:** The technique of applying torque and rotating the fibers can't be applied on non-silica fibers as they are typically very fragile. Instead a free-space Babinet-Soleil compensator (or a combination of wire grid polarizers) has to be used to control the polarization.

- **Detector sensitivity:** As we migrate from near-infrared to mid-infrared wavelengths, the sensitivity of the detectors decreases. As a result of this the signal to noise ratio degrades and thus techniques such as lock-in detection need to be employed. Another issue with the detectors in the mid-infrared wavelength range is that they are typically uncalibrated and hence the measured powers are always relative.

The measurement system which was realized in the course of this thesis can be seen in Fig. 4.1. We coupled light from a commercially available tunable QCL(Daylight solutions) in an Indium Fluoride patchcord(IRPhotonics, now ThorLabs) using a black diamond aspheric lens(ThorLabs). The coupling was achieved by putting the FC-PC connectorized end of the patchcord in a fiber coupler (Newport) which is not only able to move the fiber along the three axes but also allows rotation along y and z axes. The QCL was emitting 65 mW of power out of which 7.5 mW was coupled in the fiber. The patchcord is connected to an Indium Fluoride pigtail the cleaved end of which is mounted on a piezo-controlled xyz stage. To align this cleaved facet of the fiber with the waveguide, ideally one would like to use a mid-infrared camera. However such cameras are very expensive and hence we use a fiber connected red alignment laser connected to the input InF pigtail. The output was collected again using a cleaved fiber mounted on a piezo stage. In order to ensure maximal coupling of the light from the fiber in the waveguides, the Ge-on-Si waveguide is tapered to a width of 15 μm in order to match the mode field diameter (MFD) of the InF fiber (16 μm at 5.3 μm wavelength). The output of the fiber was coupled to an InSb detector placed inside a FTIR using an 90° off axis parabolic mirror. To increase the signal to noise ratio, the output of the detector was coupled to a lock-in amplifier. The reference to the lock-in amplifier was provided by the TTL signal generated by the QCL controller. The TTL signal (100 KHz pulse repetition rate) and the QCL pulses have a width of 0.5 μsec and a duty cycle of 5 % The QCL and the lock-in amplifier are addressed by an in-house written software which allows sweeping the laser in desired steps and simultaneous recording of the lock-in amplifier signal.

As the fibers are not polarization maintaining, it becomes essential to set the Babinet-Soleil compensator to choose the desired polarization. To control the polarization in our measurements, we first obtained the signal from the lock-in amplifier as a function of wavelength without putting any polarizer in the path. When characterizing passive filters, usually one would observe two separate peaks for TE and TM polarizations as seen in Fig. 4.2(a) due to the birefrin-

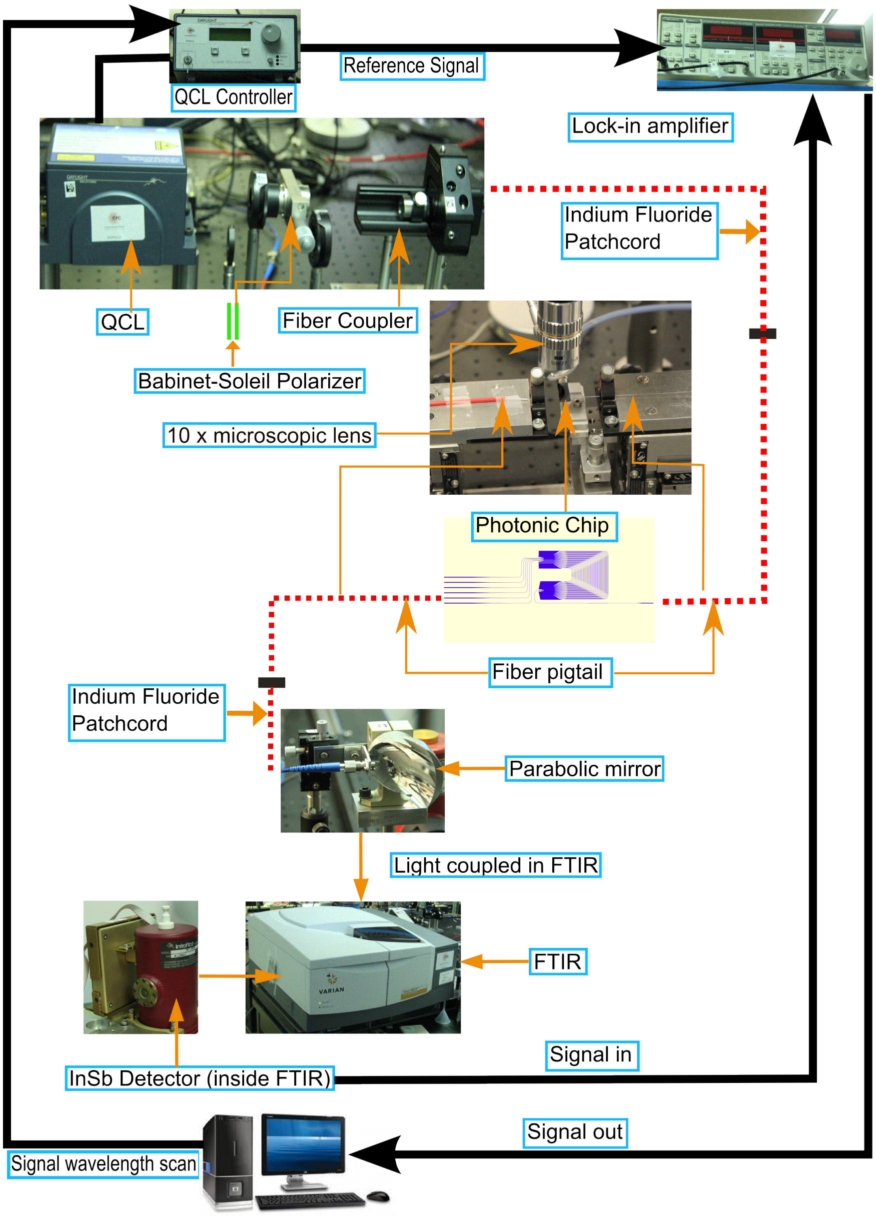

Figure 4.1: *Schematic representation of the measurement setup.*

gence of the Ge on Si waveguides used. The Babinet-Soleil compensator is then introduced in the beam path as shown in Fig. 4.1 and is adjusted in such a way that one of the peaks disappears as seen in Fig. 4.2(b). A measurement is then

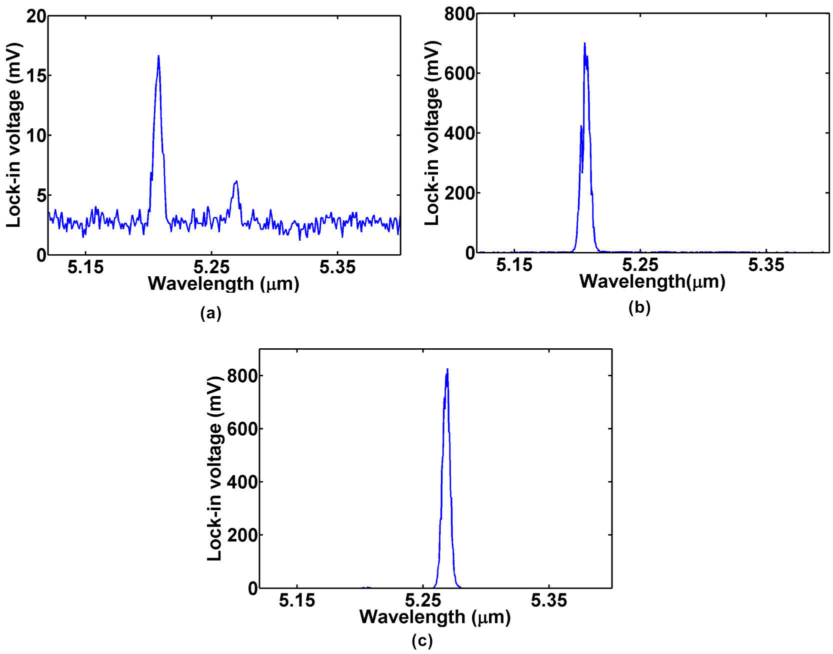

Figure 4.2: *Polarization control during the measurement of the PICs.*

done by scanning the wavelength and recording the output signal. The polarization of light at the tip of the input fiber is determined by placing a wire-grid polarizer and a thermopile. The same procedure is then repeated for the other polarization.

As we don't have access to a calibrated detector in the mid-infrared wavelength range, the transmission curves from the photonic devices are always normalized with respect to the transmission from a straight waveguide present on the same chip.From repeated measurements on the same waveguide, the variation in the lock-in signal measured over a wavelength range from 5.2um to 5.325um is estimated to be 0.5dB. This results in an uncertainty of +/- 1dB on the insertion loss of the measured optical filters.

4.3 Selection of the waveguide platform parameters

4.3.1 Thickness of the germanium layer

As discussed before in chapter 2, we have selected the Ge-on-Si waveguide platform for the realization of mid-infrared passive waveguide circuits. The thickness of the germanium layer was chosen such that the fundamental TM mode

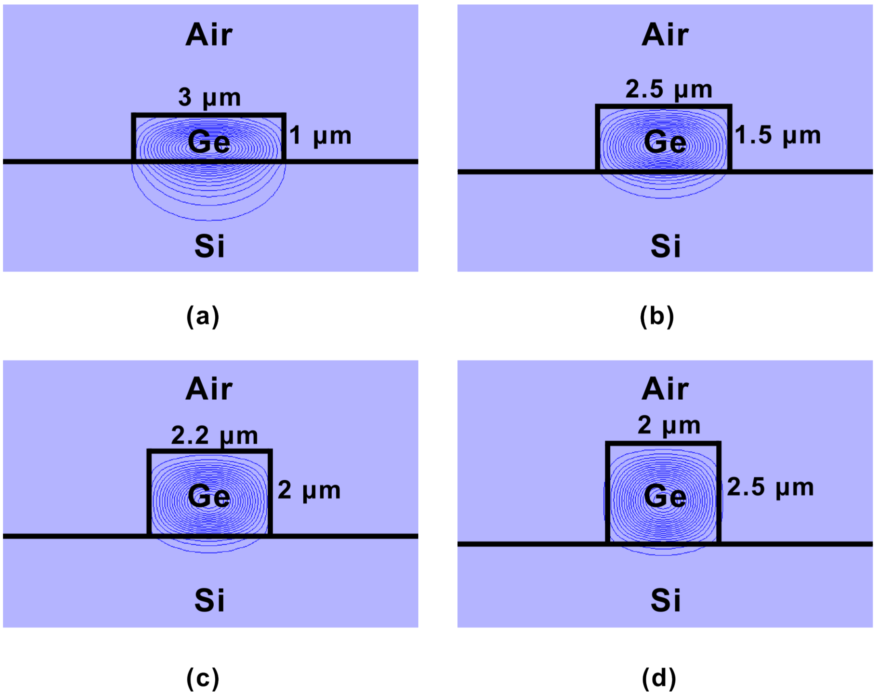

Figure 4.3: *Contour plot of the intensity of the fundamental TM mode confined in a single mode Ge waveguide core for (a) 1 μm, (b) 1.5 μm, (c) 2 μm and (d) 2.5 μm thick Ge layer at a wavelength of 5.3 μm.*

is tightly confined inside the layer and feels the germanium-silicon interface as little as possible in order to avoid losses coming from the defects at the interface. TM mode operation is selected in order to be compatible with the integration of QCLs which emit TM polarized light. A FIMMWAVE simulation showing the contour plot of the intensity of the fundamental TM mode for different germanium thickness and single mode width can be seen in Fig. 4.3. It can be observed that as the thickness increases, the overlap with the germanium-silicon interface decreases. For a thickness greater than 2 μm, the aspect ratio of the waveguide will become too large and the fabrication would become challenging. We thus fixed the germanium thickness to be 2 μm as that provides us with minimal overlap with silicon-germanium interface along with fabrication simplicity.

4.3.2 Single mode waveguide condition

Single mode operation condition is desirable in optical waveguides definitely when optical filters need to be implemented. The geometry of a waveguide determines the number of modes which are guided in it. In the previous section, we have fixed the germanium layer thickness to be 2 μm. We now have two parameters namely waveguide width and etch depth, which determine the single mode condition of the waveguide. We performed FIMMWAVE simulations in order to find out the combinations of waveguide width and etch depth which would result in a single mode TM waveguide as shown in Fig. 4.4(a). Too shallow etching leads to additional problems: the TM mode can couple to the TE guided slab mode in the cladding resulting in slab leakage loss. Therefore, a deep etch is preferred. It can be seen that the single mode width is directly proportional to the etch depth and results in a value of 2.2 μm for a 2 μm fully etched waveguide. An analysis on the design guidelines for germanium-on-silicon waveguides for different waveguide geometries at different wavelengths was carried out in [4] a graph from which showing various regions such as the TE and TM fundamental mode regions and zero-birefringence curve at a wavelength of 5.8 μm is shown in Fig. 4.4(b).

4.3.3 Bend radius

Integrated photonic circuits require waveguide bends. The bend radius however must be chosen carefully because tight bends give rise to radiation losses and hence the light confined in the fundamental mode leaks away. We simulated the bend losses as a function of radius using FIMMWAVE for a fully etched Ge-on-Si waveguide and the result can be seen in Fig. 4.5(a). It can be seen that in order to realize low loss bends we will have to increase the bend radius. We therefore chose the bend radius to be 100 μm in order to minimize the radiation losses. Such a large bend radius makes the device footprint large in comparison to SOI circuits which allow for a bend of the order of 5 μm at telecom wavelengths. In order to realize a smaller bend radius, one can consider deeply etching the silicon substrate which would make the light to be confined tightly in the waveguide core. As seen in Fig. 4.5(b), an etch depth of 3 μm into the silicon would result in virtually no loss for a 20 μm bend radius. However as our etching recipe results in etch rate of 30 nm/min for silicon we didn't carry out the deep etching of the silicon substrate.

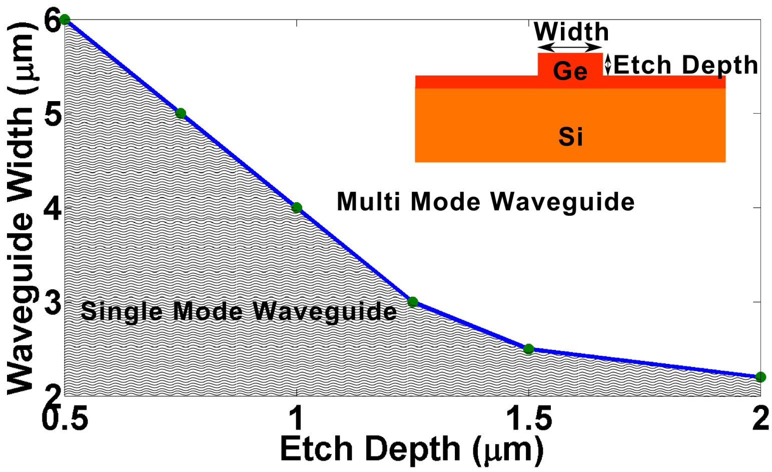

(a)

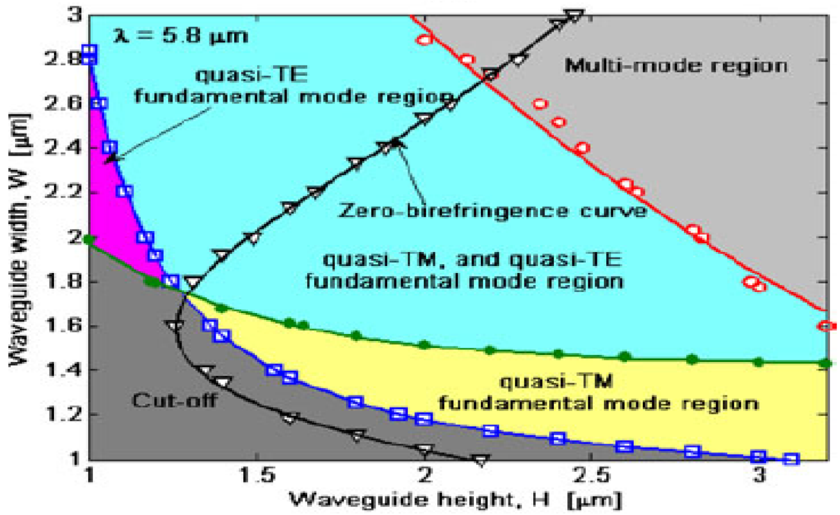

(b)

Figure 4.4: *(a) Graph showing the single mode waveguide width as a function of the etch depth of a 2 μm high Ge-on-Si waveguide at 5.3 μm for the fundamental TM mode. The shaded region represents the single mode region. (b) Graph showing various modal regions in a germanium-on-silicon waveguide as a function of waveguide geometry (from [4]).*

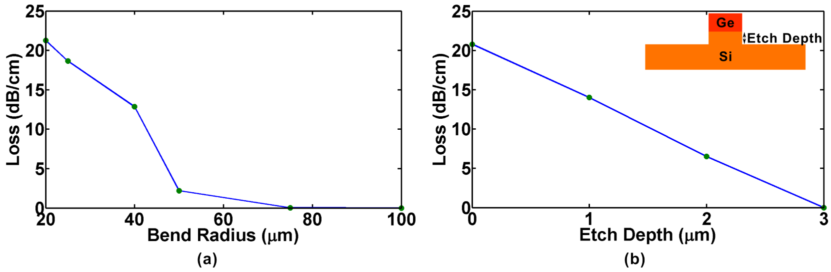

Figure 4.5: *Bend loss of the fundamental TM mode at 5.3 μm as a function of the (a) bend radius for a fully etched Ge-on-Si waveguide and (b) etch depth of silicon substrate at a bend radius of 20 μm.*

4.4 Waveguide Loss

The waveguide loss for single mode germanium-on-silicon waveguides was measured using a cut back method for both fully (2.2 μm wide and 2 μm high) and partially etched (2.2 μm wide, 2 μm high, 1.5 μm etched) waveguides. Three spirals of length 1 cm, 2 cm and 3 cm having the same number of bends of radius 100 μm were fabricated and the transmission from them was measured as a function of wavelength for both TE and TM polarization. A straight 0.5 cm waveguide was also measured. The waveguide loss for both fully and partially etched waveguides was calculated as seen in Fig. 4.6 and an example showing the cut back measurement is shown in Fig. 4.7 for a fully etched waveguide for TE and TM polarizations at 5.4 μm.

The waveguide losses are sufficiently low for cm scale photonic integrated circuits and are comparable to the values obtained in [5]. Both fully and partially etched waveguides have propagation losses in the range of 3-4 dB/cm. However for partially etched waveguides, the control of the etch depth from die to die is difficult in our RIE system. Also it was observed that within a single chip itself the etch depth has a variation of roughly 100 nm over a distance of 1 cm. Therefore we decided to focus on fully etched Ge-on-Si waveguides.

4.4.1 Origin of the waveguide loss

The losses in Ge-on-Si waveguides come from two sources namely (a) the defects located at the Ge-Si interface and (b) the side wall roughness. In order to estimate the defect density in Ge-on-Si films, a 2 μm thick Ge film was etched without any mask to various depths in RIE. Afterwards wet etching in a CrO_3:HF solution [6] for 5 minutes was carried out, the results of which are shown in Fig. 4.8. It can be seen that a 2 μm Ge film doesn't have any defects while as we go closer to the Ge-Si interface the number of defects increase and at the

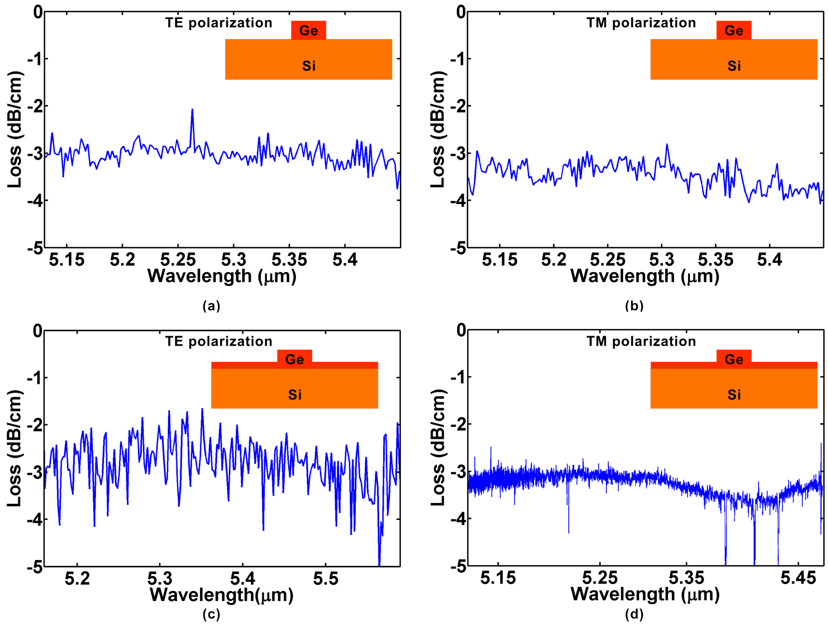

Figure 4.6: *Waveguide loss calculated using cut back method for a (a) fully etched Ge waveguide for TE polarization, (b) fully etched Ge waveguide for TM polarization, (c) partially etched waveguide for TE polarization and (d) partially etched waveguide for TM polarization.*

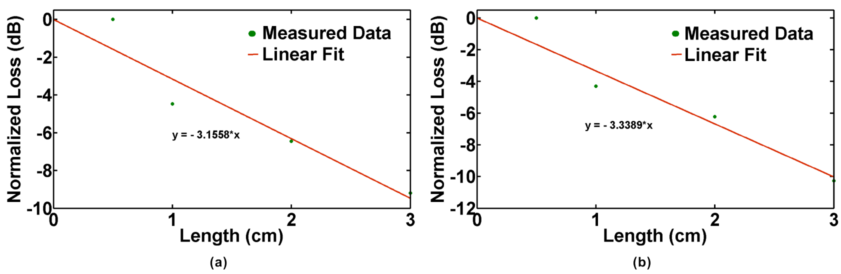

Figure 4.7: *Calculation of loss using cut back method at a fixed wavelength of 5.4 μm for (a) TE polarization and (b) TM polarization.*

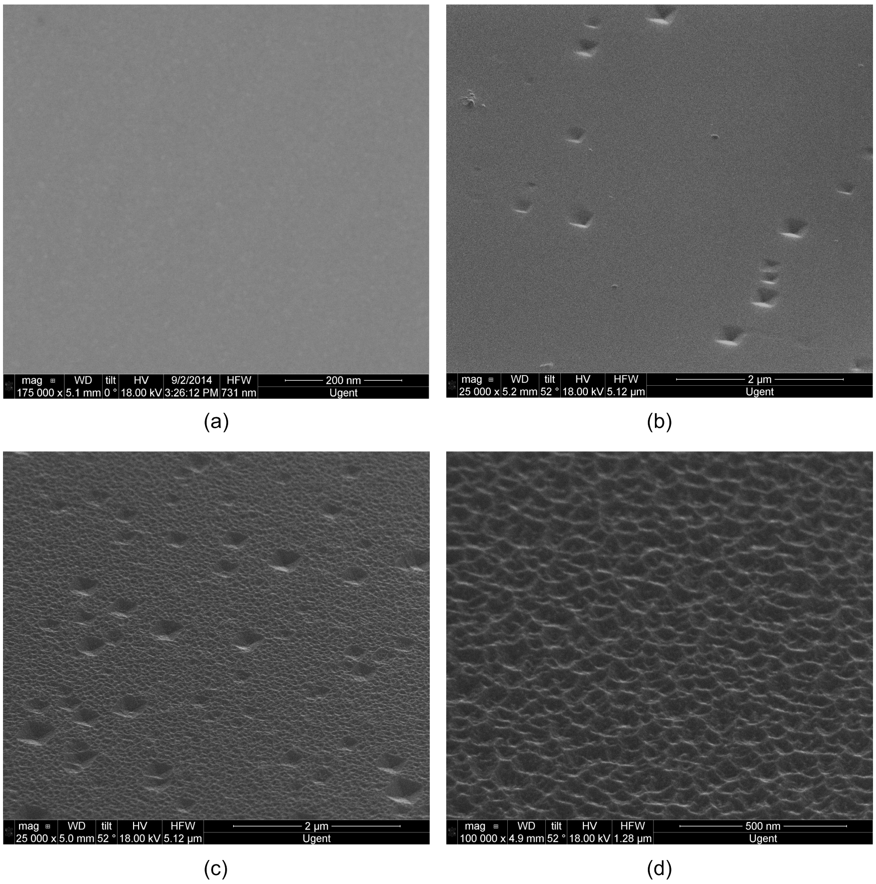

Figure 4.8: *Defects revealed in the 2 μm thick Ge film after wet etching. The Ge film was etched in RIE for (a) 0 minutes, (b) 5 minutes, (c) 10 minutes and (d) 14 minutes.*

interface the film becomes completely rough. In [7], a Ge-on-Si waveguide was designed in a 2.9 μm thick germanium film which was etched 1.7 μm. The simulated TE mode profile can be seen in Fig. 4.9(a) which shows that the mode has almost no overlap with the Ge-Si interface. Moreover, the side wall roughness of the fabricated waveguides was comparatively lower than that of waveguides fabricated in this thesis as seen in Fig. 4.9(b) and hence the reported waveguide losses were 0.6 dB/cm at 3.8 μm wavelength.

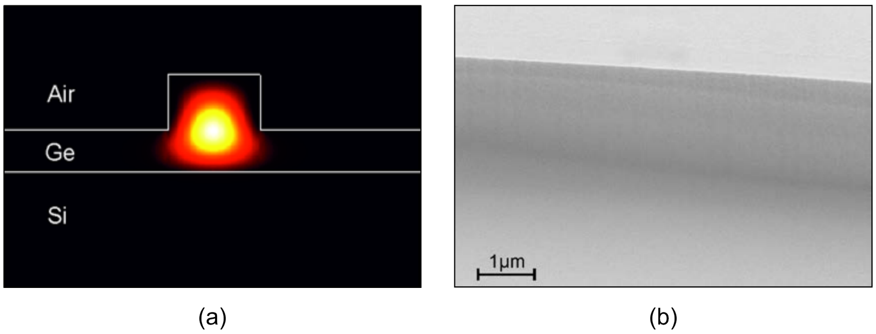

Figure 4.9: (a) Waveguide cross section and the TE mode profile at 3.8 μm and (b) sidewall roughness of the fabricated waveguide (from [7]).

4.5 Passive waveguide components

4.5.1 Mach Zehnder Interferometers

A MZI consists of an input splitter, delay lines and an output combiner. The input splitter is a m×n splitter, where m is the number of input channels and n is the number of delay lines, which splits the incoming light in the desired ratio in the delay waveguides. The difference in length between the delay waveguides is chosen to achieve a desired free spectral range (FSR). The delay waveguides are connected to a n×p MMI, where p is the number of desired output channels. Usually the number of input channels is kept to one as light from a single source needs to be divided in several channels (or vice-versa multiplexed).

4.5.1.1 Design of the MZI

The most challenging aspect of MZI design is the choice of splitter and combiner components. There are a variety of splitters and combiners one can choose from namely y-junction splitters, directional couplers and multi-mode interferometers (MMIs). Both y-junctions and directional couplers allow one to achieve any desired splitting ratio however the control on fabrication is extremely difficult especially in our processing scheme which requires metal hard mask lift-off. In Fig. 4.10(a) we plot the length for 50% coupling of light as a function of gap between two waveguides (2.2 μm wide waveguides, TM operation at 5.3 μm) and it can be inferred easily that realizing splitters of small sizes using directional couplers require sub-micron gap which is challenging using 320 nm UV contact lithography. Another issue with directional couplers is that they are narrow band. In Fig. 4.10(b), the variation in coupling power has been plotted as a function of wavelength. The waveguides were assumed to have a width of 2.2 μm and the gap between them was kept 1 μm.

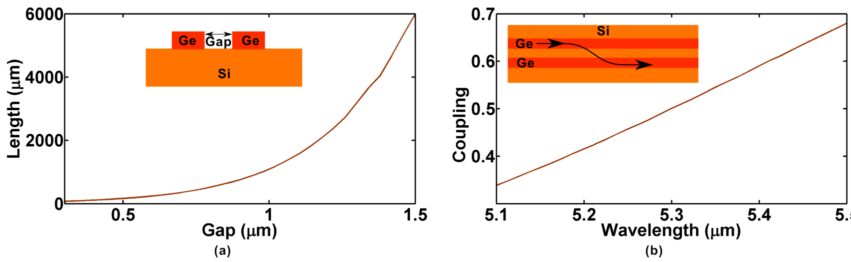

__Figure 4.10:__ (a) Length required to couple 50% of light from one fully etched 2.2 µm wide Ge waveguide to another as a function of gap and (b) coupling variation as a function of wavelength for a directional coupler with 2.2 µm wide Ge waveguides with 1 µm gap.

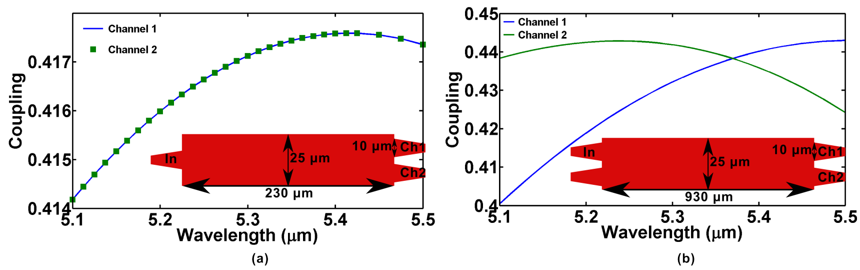

__Figure 4.11:__ Phase difference and power splitting ratio between two output arms of a 1×2 MMI of width 25 µm.

We designed 1×2 and 2×2 MMIs to achieve the desired 3 dB splitting/combining. MMIs work on the principle of self imaging and can either work on the principle of general interference or restricted interference [8]. We simulated the behavior of the 1×2 and 2×2 MMIs of different widths using FIMMWAVE and optimized the design parameters of the MMI to provide broadband 3 dB splitting of power with a constant phase relation between both output ports. The broadband power splitting of the 1×2 and 2×2 MMI can be seen in Fig. 4.11(a) and (b) respectively showing the variation in power between the input and output ports as a function of wavelength. There are two important aspects of MMI design namely power splitting ratio and the corresponding phase difference between the output at the two arms. Usually one would like to keep the footprint of the device to be as small as possible and thus choose the MMI width to be as small as possible. However the performance of the MMI is affected greatly by width variations of the MMI slab. We therefore took these imperfections in account in our simulations as seen in Fig. 4.12. For a 1×2 MMI, it can be seen in Fig. 4.12 (a) and (b) that the phase difference and the power splitting between the two output arms remains equal even when the width is changed due to the symmetry of the device and its excitation. For a 2×2 MMI, the power splitting and the phase difference becomes a bigger issue in case of fabrication imperfections. This is shown in Fig. 4.12 (c)-(h) where the power splitting and the phase difference are plotted as a function of width for a 2×2 MMI. The MMI design parameters are mentioned in the schematics for each configuration. It can be observed that the wider MMIs are more tolerant to MMI slab width variations in terms of both phase difference between the output channels and power splitting. To choose a combination which provides reasonable tolerance while keeping the overall footprint to mm scale, we chose 25 μm as the width of our MMIs which required a length of 230 μm for a 1×2 MMI and 930 μm for a 2×2 MMI. The MMIs were then cascaded in appropriate configuration to realize 1×1 and 1×2 MZIs. Both the waveguide arms had similar number of bends in order to equalize the effect coming from bending the waveguide and the upper arm had an extra straight section of 260 μm as seen in Fig. 4.13. The bend radius is kept at 100 μm to avoid any radiation losses and the total length of the lower arm is ~ 628 μm while that of the upper arm is ~ 888 μm. The MZIs in this configuration would have a FSR of 25 nm.

4.5.1.2 MZI measurement results

We measured the 1×1 and 1×2 MZIs, the normalized transmission spectra of which is shown in Fig. 4.14 (a) and (b) respectively. The FSR is found to be 24 nm which agrees well with the design parameters. It can be seen that for both MZIs, the insertion loss is 0.5 dB and the extinction ratio reaches 20 dB. For both devices, the extinction ratio varies as a function of wavelength. This variation comes from the fact that the minimum sweeping step in the laser is 1 nm which doesn't let us measure the points of destructive interference with enough precision.

4.5.2 Arrayed Waveguide Gratings

An arrayed waveguide grating (AWG) is a device used for wavelength (de) multiplexing. It can be described as an integrated version of a prism which separates incoming light in different colors. An AWG consists of input and output aperture waveguides, two wide slab regions called free propagation regions (FPR) or star couplers and an array of waveguides [9]. Light is launched in the input star coupler from an input aperture. When the beam enters the star coupler, it is no longer confined in the lateral direction and thus diverges. After arriving on the waveguide array, the divergent beam couples in the individual array waveguides and then travels to the output aperture. The length difference ΔL between two consecutive arms of the array is chosen to be constant. Therefore, for a wavelength $\lambda_c = n_{eff}\Delta L/m$ (where n_{eff} is the effective index of the mode in

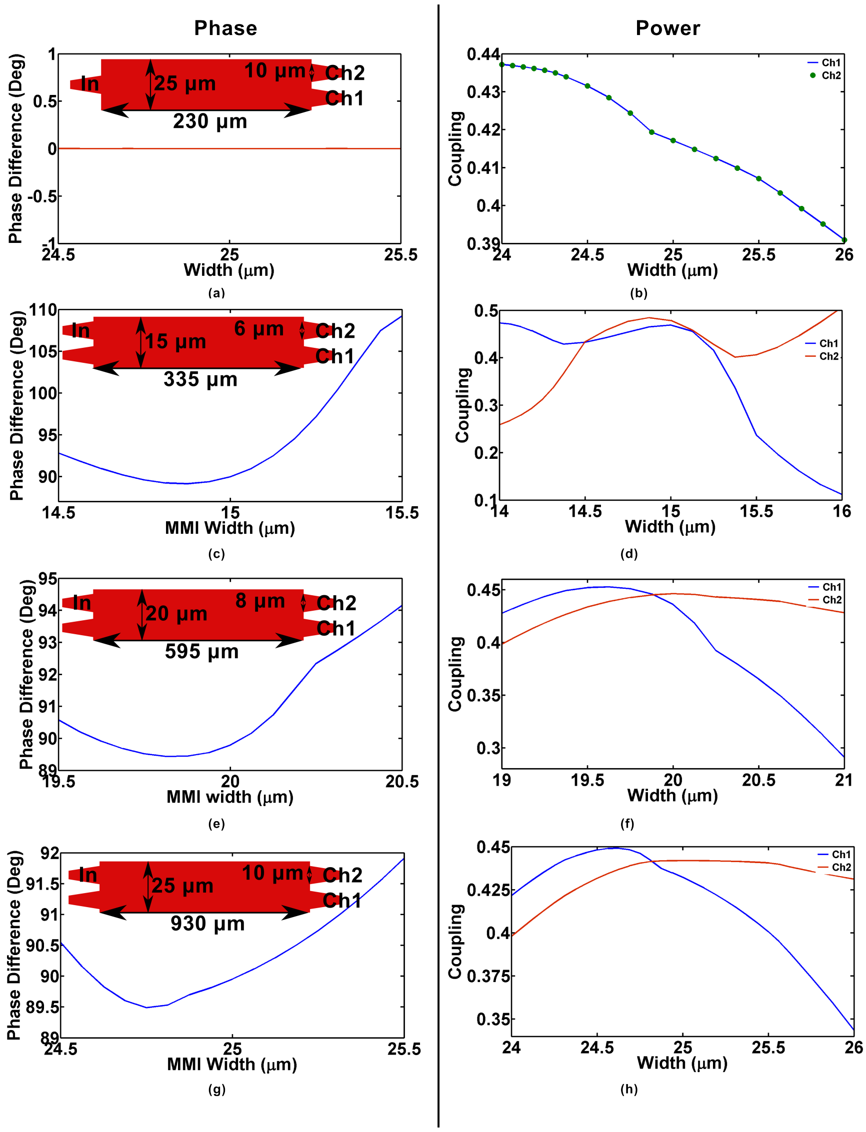

Figure 4.12: *Simulations depicting the fabrication tolerances in terms of phase difference and power splitting ratio of 1×2 and 2×2 MMIs as a function of MMI slab width. Various design parameters can be seen in the schematic diagram. The devices were simulated at a wavelength of 5.3 μm and the fundamental TM mode was launched in the MMI slab waveguide.*

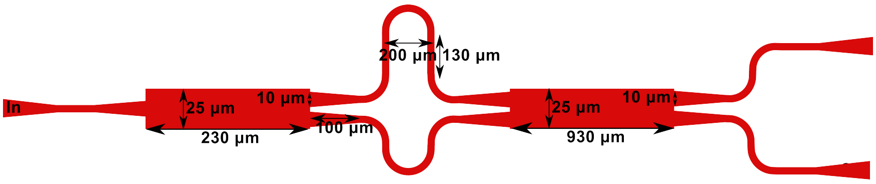

Figure 4.13: *Schematic diagram of a 1×2 MZI made by cascading a 1×2 MMI and a 2×2 MMI. Drawing is not upto scale!.*

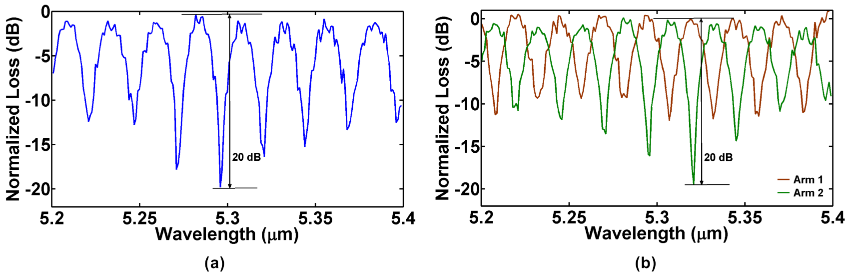

Figure 4.14: *Normalized transmission spectra of (a) 1×1 MZI and (b) 1×2 MZI*

the waveguide, ΔL is the path difference between consecutive waveguides and m is the diffraction order), after arrival at the output star coupler, the field in the individual waveguides has the same phase and thus the field at the input aperture is replicated on the output aperture. For other wavelengths, the increasing length of the array waveguides will introduce a linear phase change at the output star coupler. As a result of this the output beam will be tilted and the focus point will shift along the image plane. If we now put the output waveguides at proper positions, we can achieve spatial filtering of different wavelengths.

4.5.2.1 AWG Design

AWG design and mask layout generation can be carried out using the in house python written code in the framework of Ipkiss. An overview of the design strategy undertaken in this work is shown schematically in Fig. 4.15. The specific design strategy for simulating and designing the AWG can be found in the PhD thesis of Shibnath Pathak [10] where a rigorous model has been developed for AWGs operating at telecom wavelengths. The model is capable of not only generating a gds file but also allows one to simulate the transmission of the device. As the simulated and measured transmission spectra match reasonably and as the code is not yet adapted for other material systems at other wavelengths, we only generated the gds by supplying the specifications of our AWG. We begin by fixing the desired channel spacing ($\Delta\lambda_{channel}$), number of channels and the free

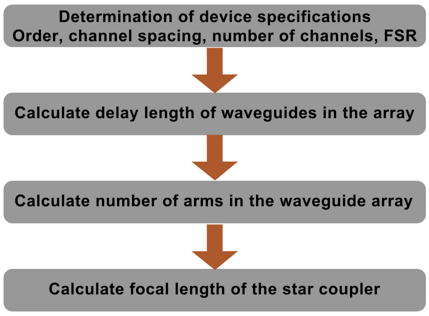

Figure 4.15: *Diagram showing the schematic diagram to obtain the parameters for AWG design.*

spectral range (FSR) of the device. We chose the channel spacing to be 200 GHz (18nm at a wavelength of 5.3 μm), five channels and a FSR of 146 nm. The delay length (ΔL) between the consecutive arms can then be calculated as,

$$\Delta L = \frac{\lambda_c^2}{n_g \lambda_{FSR}} \tag{4.1}$$

where λ_c is the center wavelength, n_g is the group index of the mode in the waveguide and λ_{FSR} is the free spectral range. This expression would result in a delay length of 46 μm if λ_c = 5.3 μm and n_g = 4.12. The next step in the calculation is the number of arms. The quality of the image formed at the output star coupler is directly proportional to the number of arms and usually one would desire a number as high as possible. However a higher number of arms means more cross talk because of the phase errors coming from side wall roughness and waveguide dimension variation. As a design rule this number is calculated as [10],

$$N \approx 3.5 \frac{FSR}{\Delta\lambda_{channel}} \tag{4.2}$$

We chose the number of arms to be 36. Next important design parameter is the focal length of the star coupler. The formula to calculate the focal length (f) is given as [9],

$$f = \frac{d_a N_{arms}}{\theta_a} \tag{4.3}$$

where d_a is the waveguide pitch in the waveguide array and θ_a is the numerical aperture of the star coupler which captures the light being diffracted from the input aperture waveguide. A narrow aperture means a large diffraction angle which would mean a shorter focal length. However, it would also require widening of the star coupler in order to capture all the light. Fig. 4.16(a) shows the far field plot of the intensity of the fundamental TE and TM mode of a 4

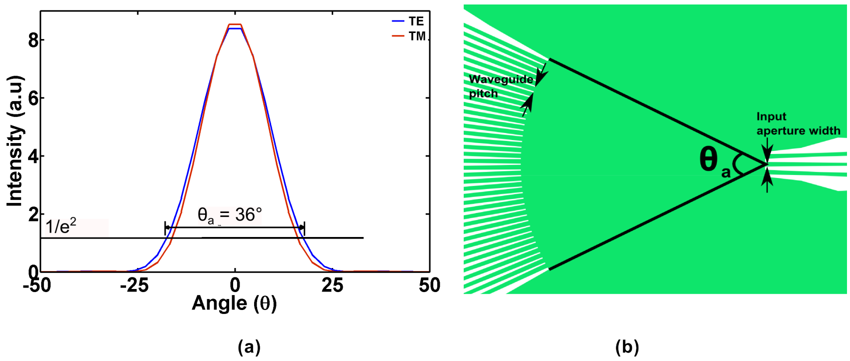

Figure 4.16: *(a) Far field diffraction pattern of the intensity of the TE and TM mode of a 4 µm wide fully etched Ge-on-Si waveguide at 5.3 µm, (b) schematic diagram of the input star coupler showing the input aperture and the diffraction angle of the beam in the free space region.*

μm wide waveguide at 5.3 μm wavelength. The diffraction angle is found to be 36°. The simulation and measurements results at 1550 nm show that the device performance is optimal when the numerical aperture of the star coupler is ~ 1.4 times the diffraction angle from the aperture (calculated using FIMMWAVE). Thus the diffraction angle is kept at 51°. In order to realize an exact image of the input field, the waveguide width at the waveguide array aperture is kept at 4 μm while the waveguide pitch is kept at 5 μm. The 1 μm gap between waveguides is limited by our lithography tool. After inserting these numbers in equation 4.3, the focal length is found to be 200 μm. The 4 μm wide aperture waveguides

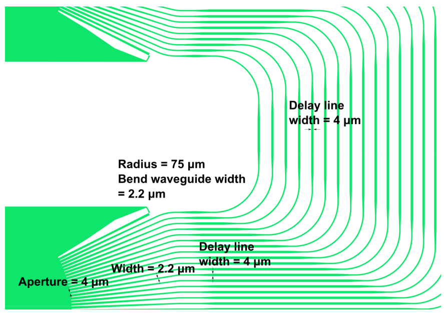

Figure 4.17: *Schematic diagram showing the various waveguide widths used in the design of the AWG.*

are then tapered to the single mode width (2.2 μm) such that the optical mode inside individual waveguides is not coupled. The waveguides are then again tapered to a width of 4 μm in the waveguide array such that the phase errors

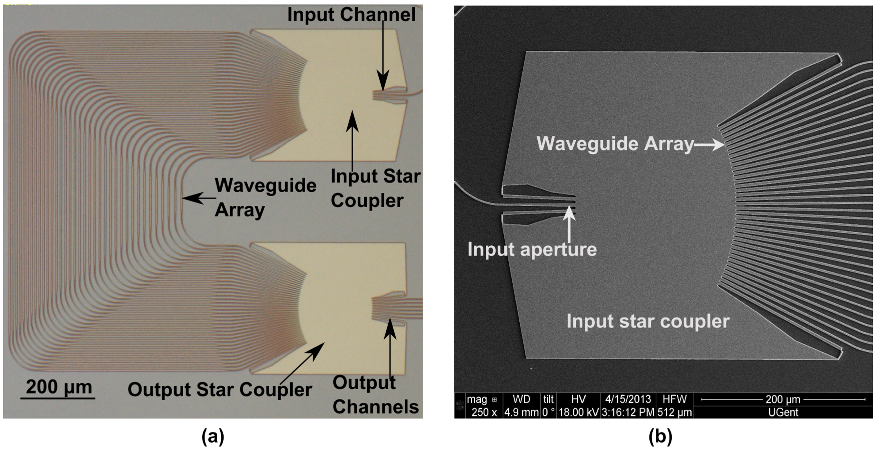

Figure 4.18: (a) A microscopic image showing the fabricated AWG showing the input channel, input star coupler, array waveguides, output star coupler and output channels and (b) a SEM image showing the input star coupler.

coming from the side wall roughness and width variations are minimized. The path length difference is achieved only by changing the length of the 4 μm wide arms and the 2.2 μm wide sections have equal length in all the arms. The bends in the AWG are kept at a radius of 75 μm which give almost no loss as seen in Fig. 4.5 (a). The schematic of the designed AWG is shown in Fig. 4.17 depicting the various waveguide widths and the bend radius.

4.5.2.2 AWG measurement results

A microscopic image of the fabricated AWG can be seen in Fig. 4.18(a) while Fig. 4.18(b) shows the input star coupler along with the input aperture and array waveguides. The footprint of the device is 1 mm × 1 mm. The normalized transmission spectra of the 5 × 200 GHz AWG can be seen in Fig. 4.19 (a) and (b) for TE and TM polarization respectively. It can be seen that the side lobe cross talk is around 20 dB for TE polarization and is around 16 dB for TM polarization. The polarization dependent peak shift is 51 nm. To evaluate the insertion loss of the device, we did a fit of the central channel with a gaussian function as shown in Fig. 4.19. From the fit, it can be seen that the AWG has an insertion loss of 2.5 dB for TE polarization and 3.1 dB for TM polarization.

There are two points on which the design can be optimized further namely the polarization dependent shift of the wavelength channels and the insertion loss. The polarization dependent phase shift can be countered by making the effective index of both TE and TM mode equal. One way of doing that is by

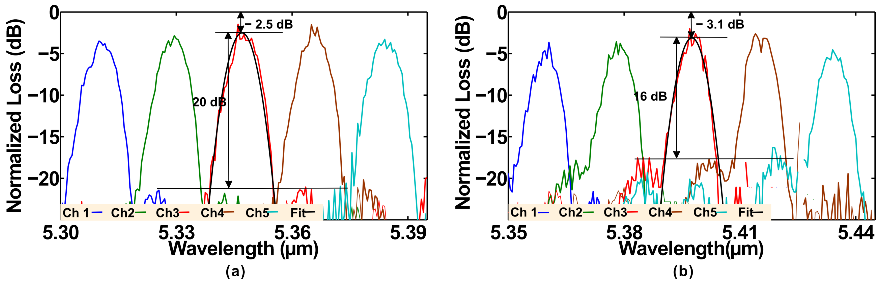

Figure 4.19: *Normalized transmission spectra of a 5×200 GHz AWG for (a) TE polarization and (b) TM polarization.*

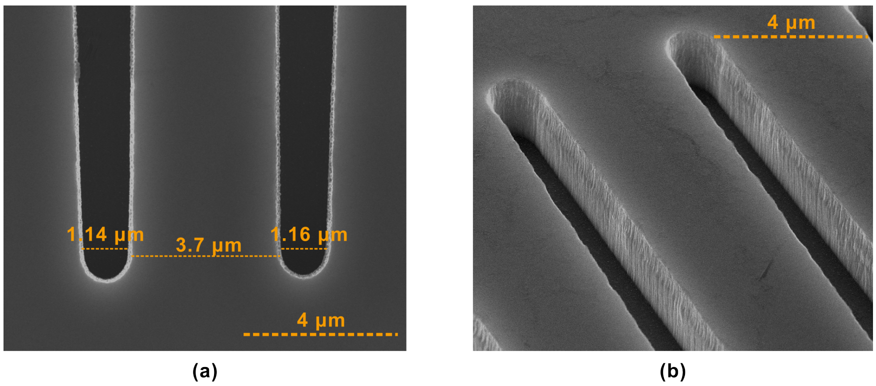

Figure 4.20: *SEM images showing the (a) corner rounding and line width reduction of the aperture waveguides and (b) roughness of the aperture waveguides.*

designing the waveguide to be square shaped and then growing a thick silicon cladding on top. This will however mean that the waveguide will become medium index contrast which will result in a larger bend radius and thus would require more space on a chip. Another way is by employing a rib type geometry where by selecting the etch depth and the width, both effective indices can be made equal [11]. The insertion loss is mainly related to lithography limitations. As explained above, the gap between the 4 μm array waveguide is kept at 1 μm. This roughly means that ~20% of the light coming from the input aperture is not coupled in the array waveguides. Also, the waveguides in the fabricated device have corner rounding and the width slightly varies from the design as seen in Fig. 4.20(a). This results in an uneven distribution of light in the individual arms and gives rise to insertion loss. The cross talk of the device mainly arises from the side wall roughness and width variations of the array waveguides. A SEM image showing the waveguide roughness can be seen in Fig. 4.20(b).

It is however worth noting that even though these were the first generation devices, their performance is already comparable to those manufactured in a CMOS fab for a SOI AWG operating at 3.8 μm [12]. This shows that with further improvement in design and access to better lithography tools, the insertion loss and crosstalk can be reduced further.

4.5.3 Planar Concave Grating

A planar concave grating (PCG) is another type of wavelength (de)multiplexer which works on the basis of interference of different light paths. Unlike an AWG which is a transmission type device, the PCG is a reflection type device. A PCG includes a slab region which is terminated by etched gratings on one side and the input and output apertures on the other side [13]. Light is launched in the slab region from an input waveguide. The concave grating performs the dual function of diffracting and refocusing the light back in a series of output waveguides. The grating facets are blazed in order to focus the light towards a specific direction where output waveguides are placed. In comparison to the AWG, the PCG offers much better control on the side lobe cross talk as the AWG is susceptible to the phase noise originating from the side wall roughness of the array waveguides while the PCG has only a slab region. On the other hand, the insertion loss of the PCG depends directly on the reflectivity of the grating facets while an AWG faces no such issue.

A major issue in AWG design is the routing of the array waveguide arms. As explained in previous section, the waveguide array requires narrowing and broadening of the waveguides and the path length difference is achieved only from the broader waveguides. As can be deducted from equation 4.1 that for larger FSR, the delay length will become smaller. It so happens that after a certain

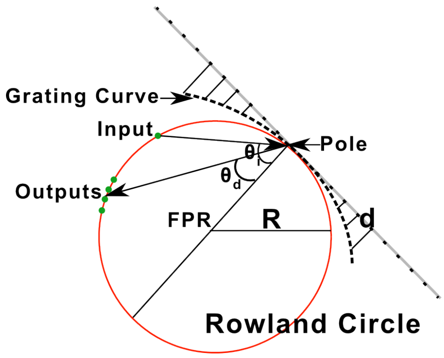

Figure 4.21: *Schematic diagram of a PCG showing the input and output apertures, grating curve and the rowland circle.*

FSR, it wouldn't be possible to design the AWG without overlapping the waveguide arms (see Fig.2 in [14]). Also, for a fixed FSR if we want more number of channels (i.e. decrease the channel spacing), it can be inferred from equation 4.2, the number of arms will become large and thus the device would become larger. As a result of this there is a higher chance of phase noise introduction and hence poor performance. As we will see in the coming sections, for wavelength (de)multiplexing with larger FSR and a large number of channels, a PCG is the preferred option over an AWG.

4.5.3.1 PCG Design

A schematic diagram of the PCG is shown in Fig. 4.21 showing the location of input and output waveguides, the grating curve and the Rowland circle. The detailed analysis of PCG design and simulation can be found in the thesis of Joost Brouckaert [15]. We are providing a brief overview here. The PCG is designed on the basis of the Rowland geometry with one stigmatic point [16]. The input and output channels are placed on a circle of radius R while the gratings are placed on a circle of radius 2R. The centers of the individual grating facets are positioned on the grating circle in such a way that, when projected onto the tangent of the circles at the pole, they are spaced equidistantly at distance d, the grating period. The imaging equation on any point of the circle can be written as,

$$d(sin\theta_i + sin\theta_d) = m\frac{\lambda}{n_{eff}} \tag{4.4}$$

where d is the grating period, θ_i and θ_d are the angle between the grating normal at the pole and the incident beam and the diffracted beam respectively, m is the order and n_{eff} is the effective index of the slab.

Another important parameter in PCG design is determination of linear dispersion (LD) which is defined as the shift of the image along the Rowland circle per unit of wavelength shift. In the Rowland geometry, it's possible to evaluate the as [15],

$$LD = \frac{\Delta s}{\Delta\lambda} = 2R\frac{d\theta_d}{d\lambda} = \frac{2R*m*n_g}{cos\theta_d*d*n_{eff}^2} \tag{4.5}$$

where Δs is the spacing between output waveguides, R is the radius, $\Delta\lambda$ is the wavelength channel spacing and n_g is the group index given as,

$$n_g = n_{eff} - \lambda\frac{dn_{eff}}{d\lambda} \tag{4.6}$$

It can be seen from equation 4.5 that for a fixed spacing between output waveguides, the radius (and thus the size of the slab) will decrease for large channel spacing. This means that the device will be less prone to layer thickness variations and hence the performance will improve.
The FSR of the PCG is given by [15]

$$FSR = \frac{\lambda}{m}\left[1 - \frac{m+1}{m}\left(1 - \frac{n_g}{n_{eff}}\right)\right]^{-1} \tag{4.7}$$

Equations 4.4, 4.5 and 4.7 provide the required parameters for the device design. We begin by first specifying a FSR of 240 nm which provides us with the diffraction order (m) of 21 once we calculate the values of n_g (=4.12) and n_{eff}(= 3.86) of the mode confined in the slab using FIMMWAVE. One can then fix the incident and the diffraction angle and calculate the grating period, d. The linear dispersion can now be calculated based on the required channel spacing and the distance between output waveguides. Knowing linear dispersion will allow one to calculate the radius of the grating curve.
The choice of incidence and diffraction angles and waveguide aperture width and spacings is made after performing the simulations in Matlab explained below.

4.5.3.2 Choice of angle

It's clear from equation 4.5 that for a constant waveguide aperture spacing and channel spacing, the radius is inversely proportional to the diffraction angle. Also, as seen in Fig. 4.22, as one increases the diffraction angle, light has to traverse a smaller distance to reach the grating facets. This implies that larger angles would result in smaller devices which would mean that device performance would be less dependent on slab layer thickness. However, larger diffraction angles also mean that the spectrum would get broader because of the aberrations caused by illumination of facets further away from the grating pole and hence

side lobe cross talk would increase. Moreover the larger angles of incidence mean that the facets away from the pole will be shaded and hence diffraction efficiency would decrease. To study the impact of diffraction angle, we carried out a simulation where light was launched in the FPR at three different angles for a fixed number of gratings assuming 100% reflectivity and fixed linear dispersion (= 400 nm/nm). The wavelength was fixed at 5.3 μm and both incidence and diffraction angles were chosen to be equal. We calculated the overlap integral between the diffracted light along the aperture waveguide and the fundamental mode of the aperture waveguide. The aperture was kept at a width of 4 μm. The results are plotted in Fig. 4.22.
It's clear that if linear dispersion is kept constant and diffraction angle is increased, the radius of the FPR will decrease which has been shown in Fig. 4.22. However we also see that the diffracted spectrum also starts to get broader with increase in angle which will increase the side lobe cross talk. At higher angles such as 80°, the output spectrum of the device is not a smooth gaussian and side lobes appear. Therefore a compromise is needed between the device size and the side lobe cross talk.

4.5.3.3 Waveguide width

Waveguide width is another parameter which plays a role in determining the device size as it controls the waveguide spacing (Δs). On the first glance from equation 4.5 one would draw a conclusion that smaller waveguide spacings would result in a smaller device. However the device size is also affected by the divergence angle of the beam launched in the FPR. Narrower waveguides have a larger divergence angle which would mean that they require more grating facets to capture all the light. This in turn would mean that aberrations would affect the spectrum as more grating facets need to be illuminated away from the pole. To study the effect of waveguide aperture width, we carried out a simulation of a PCG assuming fixed angle of incidence (= 40°) and linear dispersion (=400 nm/nm). The results are plotted in Fig. 4.23 where the electric field incident on the grating curve is plotted. It can be seen that for a 3 μm wide aperture one would require 79 facets to capture the electric field while for a 5 μm wide aperture, the number of grating facets reduces to 57. However if we plot the diffracted light back in same waveguide (as done in Fig. 4.24), we see that as the waveguide aperture increases, the spectrum gets broader which would mean an increase in the cross talk levels. It can be seen that the spectrum gets broader by 5 nm for an increase of 1 μm in the aperture width.
After keeping in mind the above mentioned points, we designed the PCG with single input and six output waveguides which had a aperture width of 4 μm. The waveguide spacing was chosen to be 10 μm. This spacing is chosen such that there is neither any optical coupling between the 4 μm wide waveguides nor any

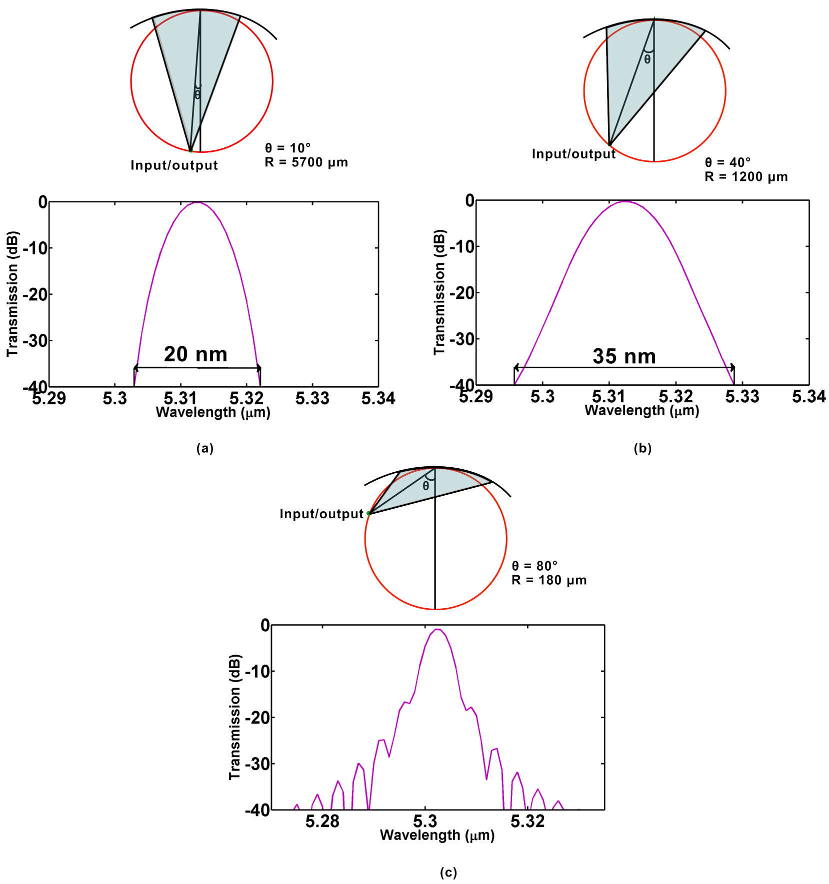

Figure 4.22: *Influence of the incidence and diffraction angle on device size and performance. The waveguide aperture is fixed at a width of 4 µm, linear dispersion at 400 nm/nm. The incidence and diffraction angles are equal. TM polarized light at 5.3 µm wavelength was launched from the waveguide.*

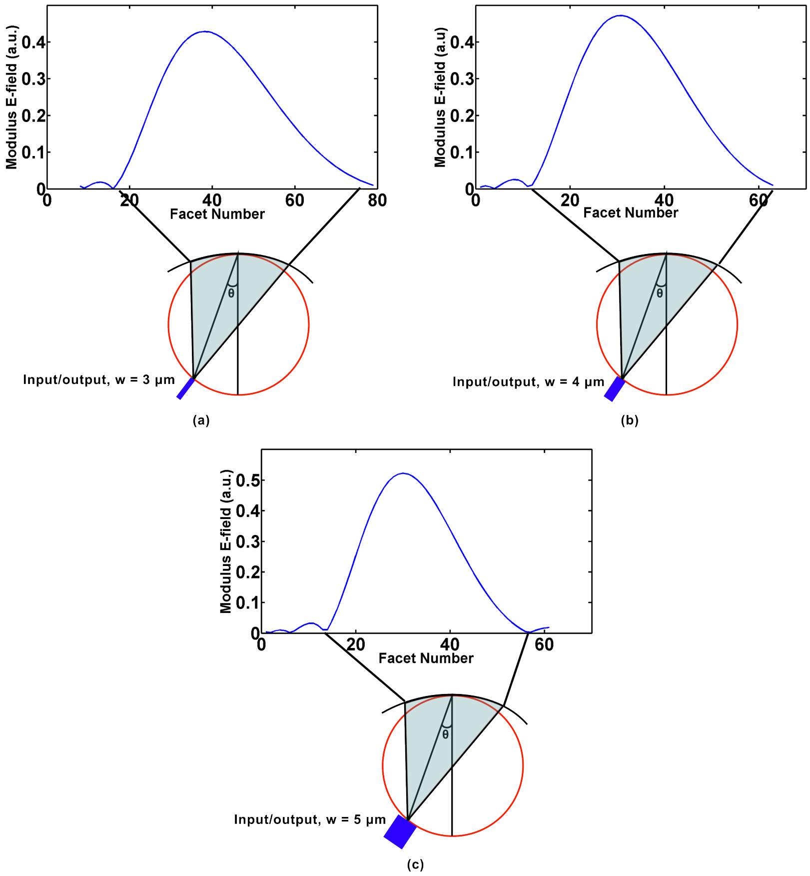

Figure 4.23: *Influence of the waveguide aperture width on the number of required grating facets. The input and output waveguide aperture is fixed at an angle of 40° and the linear dispersion at 400 nm/nm. TM polarized light at 5.3 µm wavelength was launched from the waveguide*

shading effect which would result in blockage of light going in apertures away from the input. The angle of incidence was chosen to be 44° while the angle of diffraction was chosen to be 41°. The input and output apertures were placed on a circle with a radius of 666 μm. The number of grating facets was chosen to be 63 which were placed on a circle of radius 1332 μm as seen in Fig. 4.25.The device footprint was 1.5 mm by 1.2 mm.

To get an idea of the device performance we obtained the transmission spectra of our PCG with above mentioned parameters assuming a 100% reflecting grating, the results of which are shown in Fig. 4.26. In the simulation we can't take

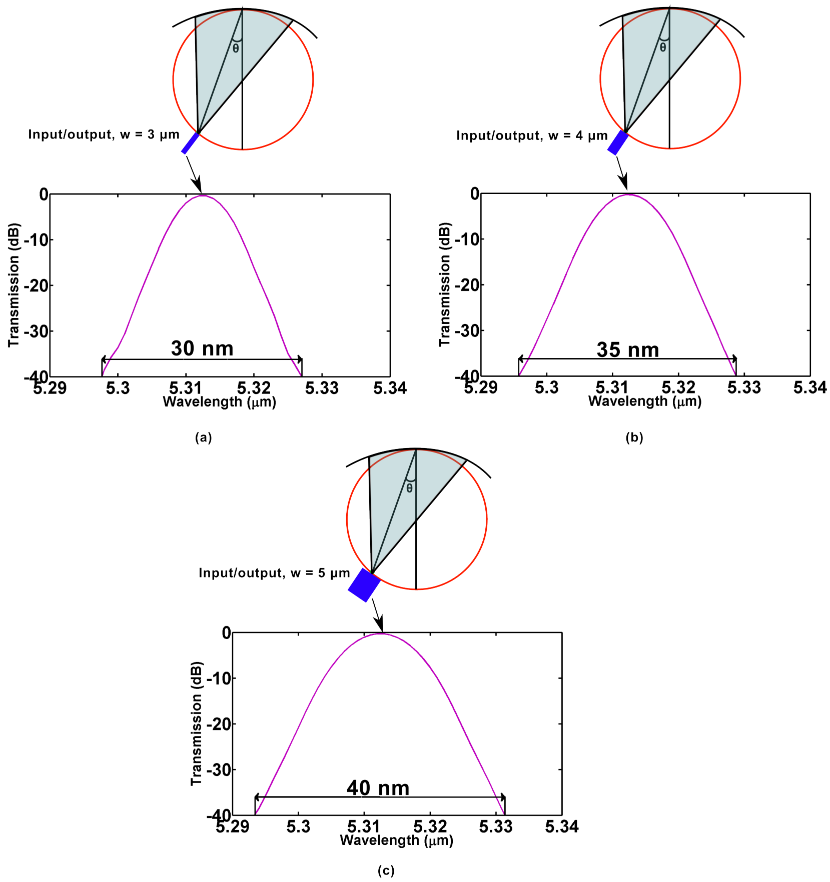

Figure 4.24: *Influence of the waveguide aperture width on the device performance. The input and output waveguide aperture is fixed at an angle of 40° and the linear dispersion at 400 nm/nm. TM polarized light at 5.3 µm wavelength was launched from the waveguide*

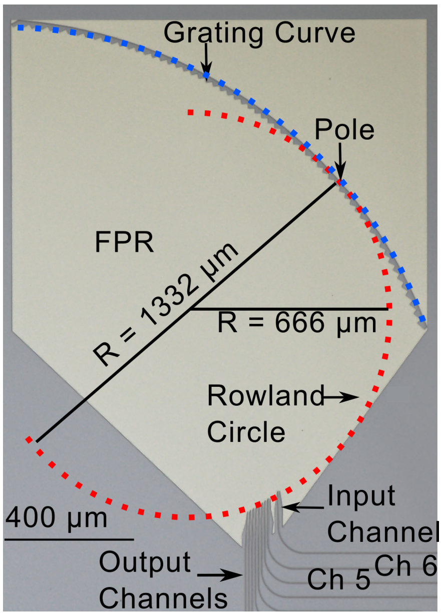

Figure 4.25: *(a) A microscopic image of the fabricated PCG detailing the specifications.*

into account the fabrication imperfections such as variations in the slab thickness and non-ideal grating facets. We expect crosstalk levels of -27 dB. In order to analyze our simulations, we fabricated the PCG with three different grating facets as described in the next section.

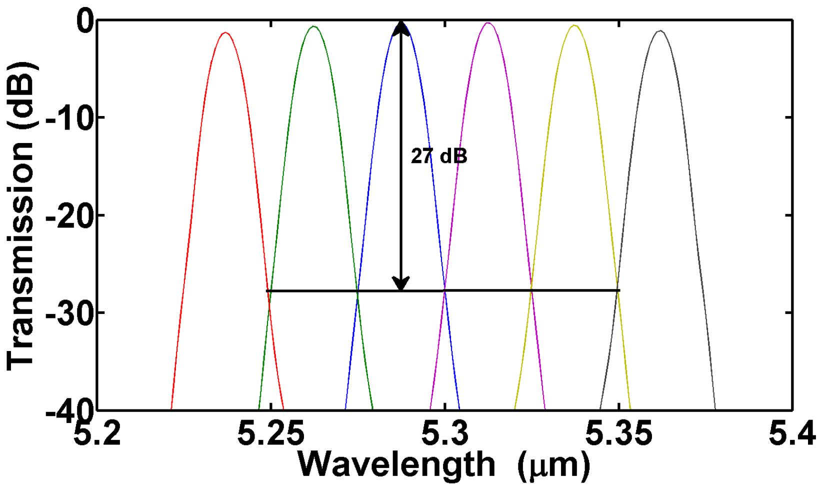

Figure 4.26: *Simulated response of a PCG with 25 nm channel spacing for TM polarization.*

4.5.3.4 Flat facet grating

First we fabricated a PCG with flat grating facet between germanium (n = 4) and air (n = 1). Assuming perpendicular incidence, the Fresnel power reflection coefficient can be calculated as,

$$R = \left\{ \frac{n_1 - n_2}{n_1 + n_2} \right\}^2 = 0.36. \tag{4.8}$$

A SEM image of such a flat facet can be seen in Fig. 4.27(a) and the normalized transmission spectra can be seen in Fig. 4.28 for TE and TM polarization. The side lobe cross talk is found out to be 23 dB and 21 dB for TE and TM polarization respectively and the corresponding insertion loss is calculated to be 7.6/6.4 dB. The side lobe cross talk is higher than the simulated cross talk which is attributed to variations in the thickness of the slab region. The relatively high insertion loss can be explained by the low reflection from the grating facets. The Fresnel reflection loss coming from the flat facet is -4.5 dB. To assess the extra 2-3 dB loss, let's have a closer look at the SEM image of the flat grating facet in Fig. 4.27(b). One can see that instead of being perfectly vertical, the facet has a step-like shape. A Lumerical FDTD simulation was performed to assess the impact of this on the reflection and it was found that the reflection coefficient differs only slightly. However, the facet has a rough side wall which would scatter the light in all the directions. Further losses are introduced by lithographic imperfections such as corner rounding. In order to characterize the individual channels spectrally, we plot the overlapped spectra of these channels in

Fig. 4.29. It can be seen that the central lobe of all channels overlap nicely. Only the side lobe of the sixth channel is seen prominently which is also attributed to fabrication imperfections.

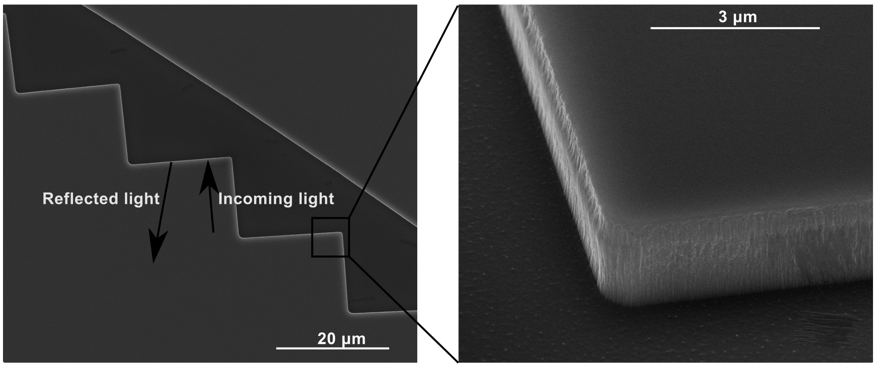

Figure 4.27: *SEM images showing (a) Flat grating facets and (b) fabrication imperfections such as non-vertical side walls, roughness and corner rounding.*

4.5.3.5 Total internal reflection grating

In order to increase the reflections from the grating facets, we fabricated total internal grating facets as shown in the SEM image in Fig. 4.30(a). The design of these facets is based on the principle of total internal reflection. The grating facets are designed such that the light hits each facet at an angle of $\approx 45°$ which is greater than the total internal reflection angle of $\approx 15°$ between germanium and air. As schematically shown in Fig. 4.30(a), the incoming light would

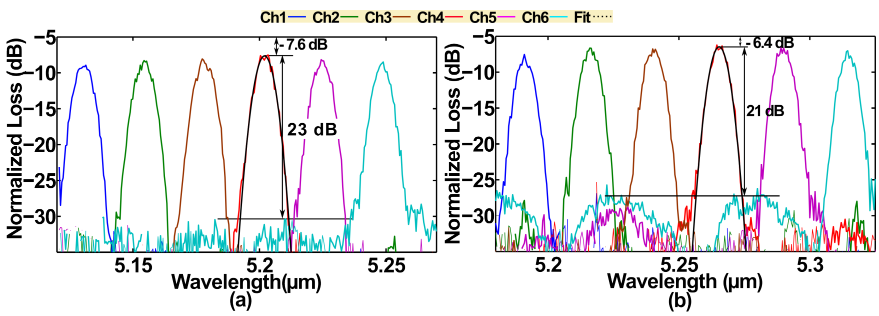

Figure 4.28: *Normalized transmission spectra of a six channel PCG with 25 nm channel spacing with flat facet gratings for (a) TE polarization and (b) TM polarization.*

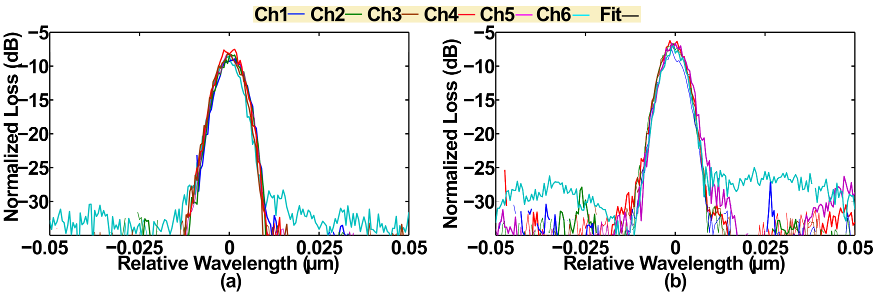

Figure 4.29: *Overlapped spectra of the six channels for (a) TE polarization and (b) TM polarization.*

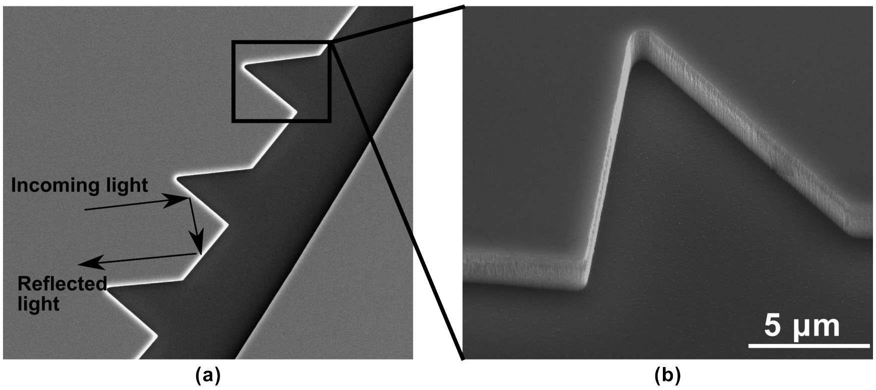

Figure 4.30: *SEM images showing (a) TIR grating facets and (b) fabrication imperfections such as non-vertical side walls, roughness and corner rounding.*

be reflected towards the output apertures. In theory, a very high reflection is possible, however since two reflections are needed, the loss due to roughness of the etched walls and the corner rounding increases. A SEM image in Fig. 4.30(b) shows these fabrication imperfections. Also, it's not possible to blaze each grating facet to reflect light and thus maximal light is sent back on the input waveguide.

Since it's not possible to blaze the grating facets, we observed that the output waveguides collect less light as we move away from the input aperture. As a result, the insertion loss increases for channels away from the input as seen in Fig. 4.31(a). Also the overlapped spectra of all the channels in Fig. 4.31(b) shows that there are significant variations in the spectral performance of all the channels which indicates that there might be some fabrication imperfections in this PCG.

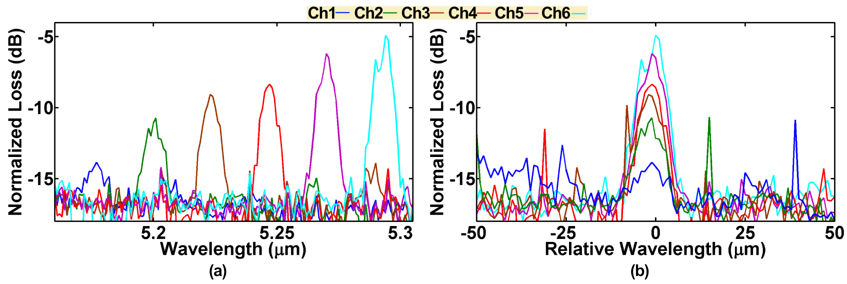

Figure 4.31: *(a) Normalized transmission spectra for TM polarization for a total internal reflection grating and (b) overlapped spectra of all the channels.*

4.5.4 Bragg Reflectors

In order to maximize the reflections from the grating facets, we put DBR gratings on the grating curve as seen in Fig. 4.32(a). The DBRs can be designed to have very high reflection and can be blazed as well to focus light in the output waveguides. Normally one would like to design first order DBRs which have maximal reflectivity however we are limited in the linewidth because of our lithography. Therefore we kept the DBR period to 2.15 μm with a fill factor of 50% which results in a third order grating. The normalized transmission spectrum for TE and TM polarization can be seen in Fig. 4.33 (a) and (b) respectively. It can be seen that the insertion loss for TE and TM polarizations is found to be 4.9 dB and 4.2 dB and the cross talk is 22 dB and 23 dB respectively. The overlapped spectra of the six channels for TE and TM polarizations can be seen in Fig. 4.34 (a) and (b) respectively which demonstrates that the spectral behavior of individual channels is almost the same.

The major cause of insertion loss is that the third order grating only reflects back ~65%. This would account for -1.8 dB of insertion loss. However the fabricated DBR gratings contain imperfections and suffer from high side wall roughness as seen in Fig. 4.32(b). Also, as can be seen in Fig. 4.32(c), the fabricated grating has teeth of width 950 nm while the gap is 1.15 μm. A 2-D simulation of the reflectivity of a four period DBR grating at a wavelength of 5.25 μm was carried out as a function of grating period and fill factor as shown in Fig. 4.35(a) for TM polarized light. We can see that the fabricated grating will have a reflectivity of ~55%. Another source of loss could be the corner rounding of the DBR gratings which is seen in Fig. 4.32(c). It can be shown from scalar diffraction theory that the electric field diffracted from a grating facet is proportional to its width. The amount of light lost due to corner rounding can be calculated as,

$$L_{CornerRounding} = 20 * log \frac{W_{eff}}{W} \tag{4.9}$$

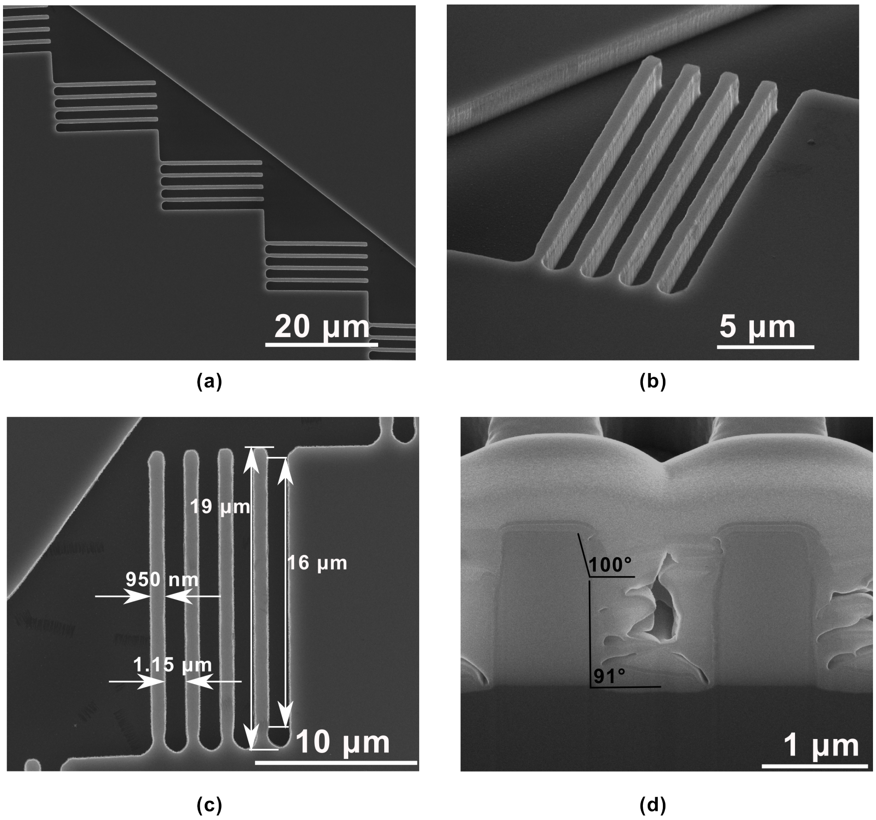

Figure 4.32: *SEM images showing (a) perspective view of the fabricated DBR gratings, (b) zoomed in view showing the side wall roughness, (c) top view showing the dimensions of the gratings and (d) cross section view demonstrating the non-vertical side walls. The grating in (d) has been covered by platinum to take a SEM image.*

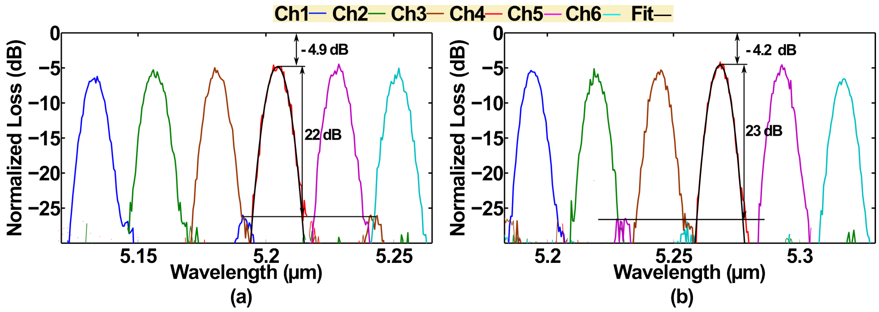

Figure 4.33: *Normalized transmission spectra of a six channel PCG with 25 nm channel spacing with DBR gratings for (a) TE polarization and (b) TM polarization.*

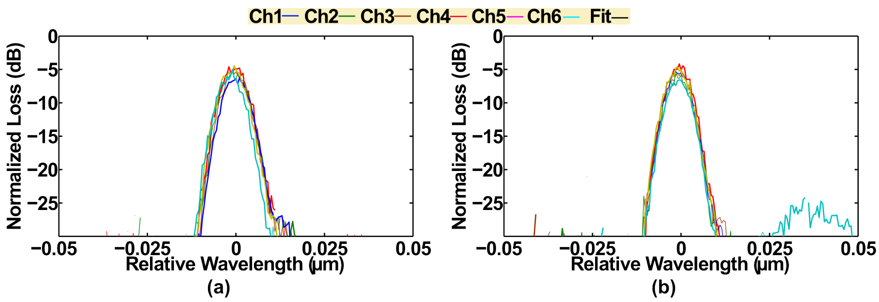

Figure 4.34: *Overlapped spectra of the six channels for (a) TE polarization and (b) TM polarization.*

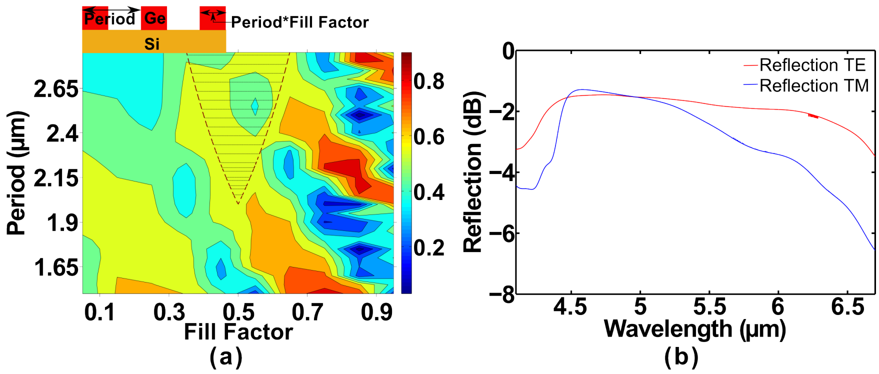

Figure 4.35: *(a) a 2-D contour plot showing the reflectivity of the grating as a function of period and the fill factor. The shaded area represents the combination which would result in a minimum feature size of 1 μm and the grating dimensions are shown above. (b) broadband reflectivity of the TE and TM polarized light of a four period DBR grating with period 2.15 μm and fill factor 50%.*

where W_{eff} is the length of the grating teeth which is straight and W is the total length of grating teeth. For our fabricated grating this would give an excess loss of 1.8 dB. Fig. 4.32(d) shows a cross section of the grating which shows that the side walls are not perfectly straight but have a polygon like shape. However our previous simulations indicate that this doesn't impact the reflection by a considerable amount. The insertion loss can be reduced by fabricating a grating with higher reflectivity. It can be seen in Fig. 4.35(a) that a period of 2.15 μm and a fill factor of 85%, will result in a reflectivity of 95%. This will mean a grating with slit of width 320 nm is required which is possible in a standard CMOS pilot line. Fig. 4.35(b) shows the simulated reflection spectrum of the four period DBR grating with a period of 2.15 μm and fill factor of 0.5 for both TE and TM polarized light in the 4-7 μm wavelength range showing a peak reflectivity of -1.45/-1.25 dB and -1 dB bandwidth of 2.1/1 μm for TE/TM polarization.

4.5.5 Ring Resonators

Ring resonators allow the realization of high-Q factor filters [17]. They are used in many configurations in integrated optics and complex filter functions can be obtained by combining them in series or parallel. However, ring resonators require the fabrication of directional couplers to couple light from an incoming waveguide to the ring itself. As explained in section 4.5.1.1 due to the lithographic limitations, it wouldn't be feasible for us to fabricate a directional coupler containing two fully etched waveguides as it would require fabricating two

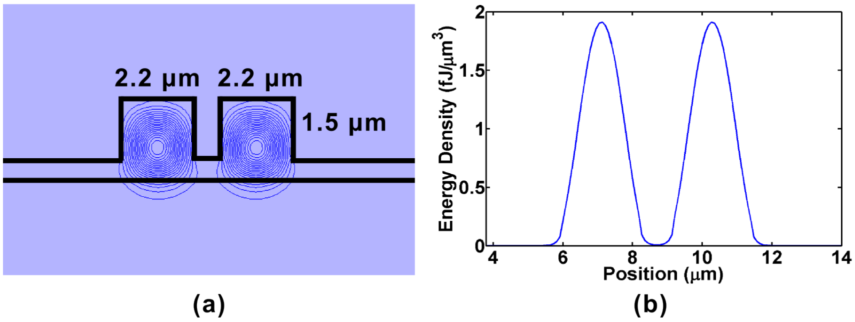

Figure 4.36: (a) Contour plot of the intensity of the TM mode at 5.3 μm wavelength in a partially etched directional coupler with 2.2 μm wide waveguides with 1 μm gap in between and (b) the corresponding intensity profile in the horizontal direction.

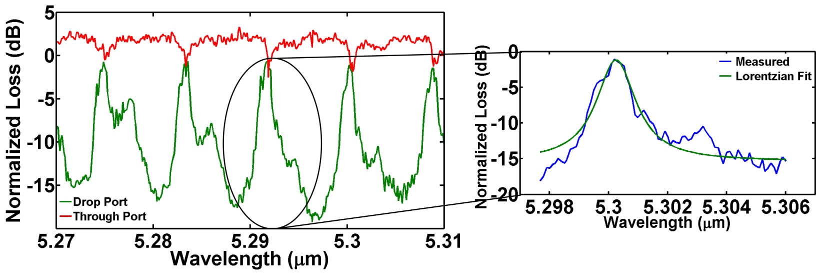

Figure 4.37: Normalized transmission spectra of an add-drop ring with directional coupler with 10% coupling. The zoomed figure on the right shows a peak with a Lorentzian fit. The normalized value is larger than zero because of a badly cleaved facet.

parallel waveguides very close to each other over a relatively large length. A way of increasing the coupling between waveguides is to partially etch the waveguide which increases the coupling and thereby allows a larger gap. The mode profile of the symmetrical TM supermode for such a directional coupler containing two partially etched 2.2 μm wide waveguides separated by a gap of 1 μm can be seen in Fig. 4.36(a) while Fig. 4.36(b) shows the intensity profile in the horizontal direction. The length required for 10% coupling was found to be 150 μm. We fabricated racetrack ring resonators in add drop configuration with a roundtrip length of 771 μm (having a radius of 75 μm, straight section of 150 μm and the gap between the waveguides of 1 μm). The spectra of such a ring can be seen in Fig. 4.37(a) where the length of directional coupler was also kept at 150 μm in order to achieve 10% coupling.

To calculate the FWHM and the Q-factor of our ring resonators, we carried

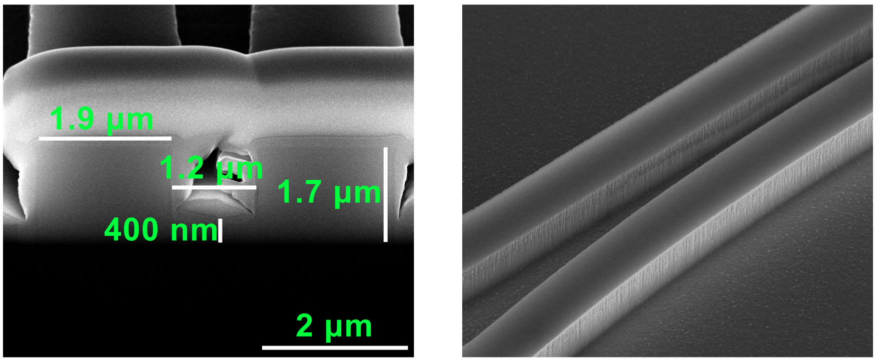

(a) (b)

Figure 4.38: *SEM image showing (a) cross section of the directional coupler section of the ring resonator (covered with platinum) and (b) bird's eye view of the directional coupler.*

out a lorentzian fit of a peak as shown on the right hand side of Fig. 4.37. The FWHM was found out to be 1 nm and the Q-factor was calculated to be 5300. The Q-factor of the fabricated ring resonator is significantly below what is required for an integrated filter. Another issue seen here is that a parasitic peak is observed in the spectrum. This is attributed either due to the fact that the polarization of the incident light is not purely TM polarized or due to the fact that the TE mode is weakly excited in the directional coupler (given the assymetrical vertical structure of the waveguides).

A major issue in fabricating the ring resonators with directional couplers was that the required gap between the coupling waveguide is very close to the limit of our lithography tool. This results in a yield of only 5%. A microscopic image of the directional coupler section after performing image reversal lithography is shown in Fig. 4.39(a) and (b). Fig. 4.39(a) shows a sample on which the lithography was successful while Fig. 4.39(b) shows a sample where the gap between the bus waveguide and the ring hasn't been defined. Because of the above mentioned reasons, ring resonators were not pursued further in this thesis.

4.6 Conclusions

In this chapter, we began by discussing the challenges which are faced to realize a measurement system for the mid-ir wavelength range and methods to overcome them. We then described the design methods and the performance of fabricated passive Ge-on-Si photonic devices. The waveguide losses were found to be in the range of 3-4 dB/cm which are low enough to realize most mid-infrared

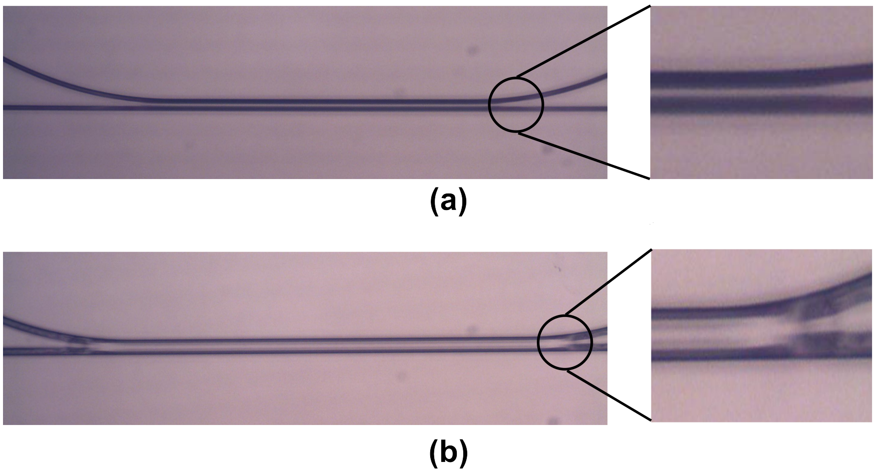

Figure 4.39: Microscopic image showing the photoresist pattern after image reversal lithography of the directional coupler section of the ring resonator (a) successful lithography and (b) unsuccessful lithography. The narrow gap between the waveguides won't be defined in case (b).

PICs. The waveguide losses arise mainly because of the defects at the Ge-Si interface and sidewall roughness. We fabricated devices like MZIs, AWGs, PCGs and ring resonators. It can be seen that although the fabrication of these devices is done with tools which are not comparable to standard CMOS pilot line equipment, the performance is still reasonable. Apart from ring resonators, whose fabrication was a challenge because of lithographic limitations, other devices perform reasonably. This shows that with improvement in design and fabrication, the performance of these devices can still be improved which could make the manufacturing of high performance passive integrated mid-infrared PICs in a CMOS fabrication environment a reality in the near future.

References

[1] Robert G. Hunsperger. *Integrated Optics.* Springer, 2009.

[2] Christophe Lafond, Jean-François Couillard, Jean-Luc Delarosbil, Fernand Sylvain, and Philippe de Sandro. *Recent improvements on mid-IR chalcogenide optical fibers.* In SPIE Defense+ Security, pages 90701C–90701C, 2014.

[3] Mohammed Saad. *Fluoride glass fiber: state of the art.* In SPIE Defense, Security, and Sensing, pages 73160N–73160N, 2009.

[4] Francesco De Leonardis, Benedetto Troia, and Vittorio Passaro. *Mid-IR Optical and Nonlinear Properties of Germanium on Silicon Optical Waveguides.* Journal of Lightwave Technology, 32(22):3747–3757, 2014.

[5] Yu-Chi Chang, Vincent Paeder, Lubos Hvozdara, Jean-Michel Hartmann, and Hans Peter Herzig. *Low-loss germanium strip waveguides on silicon for the mid-infrared.* Optics Letters, 37(14):2883–2885, Jul 2012.

[6] Laurent Souriau, Tanya Atanasova, Valentina Terzieva, Alain Moussa, Matty Caymax, Roger Loo, Marc Meuris, and Wilfried Vandervorst. *Characterization of threading dislocations in thin germanium layers by defect etching: Toward chromium and HF-Free solution.* Journal of The Electrochemical Society, 155(9):H677–H681, 2008.

[7] M. Nedeljkovic, J. Soler Penades, C. Mitchell, A. Khokhar, S. Stankovic, T. Dominguez Bucio, C. Littlejohns, F. Gardes, and G. Mashanovich. *Surface Grating Coupled Low Loss Ge-on-Si Rib Waveguides and Multimode Interferometers.* Photonics Technology Letters, IEEE, PP(99):1–1, 2015.

[8] Lucas B Soldano and Erik CM Pennings. *Optical multi-mode interference devices based on self-imaging: principles and applications.* Journal of Lightwave Technology, 13(4):615–627, 1995.

[9] Meint K Smit and Cor Van Dam. *PHASAR-based WDM-devices: Principles, design and applications.* IEEE Journal of Selected Topics in Quantum Electronics, 2(2):236–250, 1996.

[10] Shibnath Pathak. *Silicon Nano-Photonics Based Arrayed Waveguide Gratings.* PhD thesis, Gent University, 2014.

[11] L Vivien, S Laval, B Dumont, S Lardenois, A Koster, and E Cassan. *Polarization-independent single-mode rib waveguides on silicon-on-insulator for telecommunication wavelengths.* Optics communications, 210(1):43–49, 2002.

[12] M. Muneeb, X. Chen, P. Verheyen, G. Lepage, S. Pathak, E. Ryckeboer, A. Malik, B. Kuyken, M. Nedeljkovic, J. Van Campenhout, G. Z. Mashanovich, and G. Roelkens. *Demonstration of Silicon-on-insulator mid-infrared spectrometers operating at 3.8 um.* Optics Express, 21(10):11659–11669, May 2013.

[13] Reinhard Mearz. *Integrated optics: design and modeling.* Artech House, 1995.

[14] S. Pathak, P. Dumon, D. Van Thourhout, and W. Bogaerts. *Comparison of AWGs and Echelle Gratings for Wavelength Division Multiplexing on Silicon-on-Insulator.* IEEE Photonics Journal, 6(5):1–9, Oct 2014.

[15] Joost Brouckaert. *Integration of Photodetectors on Silicon Photonic Integrated Circuits (PICs) for Spectroscopic Applications.* PhD thesis, Ghent University, 2011.

[16] K.A McGreer. *Diffraction from concave gratings in planar waveguides.* IEEE Photonics Technology Letters, 7(3):324–326, March 1995.

[17] Dominik G Rabus. *Integrated ring resonators.* Springer, 2007.

5

Thermo-Optic Phase Shifters

"Design is a funny word. Some people think design means how it looks. But of course, if you dig deeper, it's really how it works."

– Steve Jobs

5.1 Introduction

Many applications in integrated optics such as "imprinting" the information on an optical carrier and optical switching require the modulation of the light propagating in a waveguide [1]. The phase of an optical wave can be changed by changing the effective index of the optical mode [2]. Modulation of the effective index can be done in several ways such as by using the thermo-optic effect [3], the plasma dispersion effect [4] or the electro-optic effects such as Kerr effect and Pockels effect. Although the plasma-dispersion effect allows one to achieve modulation at very high speeds (Gbit/sec [5]), the implementation of it requires generation of free carriers by means of doping in the waveguide. These free carriers give rise to optical losses through free carrier absorption (FCA) which are at tolerable levels at telecom wavelengths but increase in the mid-infrared wavelength range. This was shown in Fig.3.1 (c) and (d) where for n-type doping concentration of 10^{17} cm^{-2}, the FCA for Si at telecom wavelength was ~1 cm^{-1} while for germanium it rises to ~10 cm^{-1} at 5 μm. Electro-optic effects such as Kerr and Pockels effect are weak in silicon at telecom wavelengths [6] and we can expect a similar behavior at mid-infrared wavelengths for germanium. Another way of achieving modulation is using the electro-absorption effect using the quantum confined stark effect or Franz-Keldysh effect which requires implementation of other materials such as Ge or SiGe on SOI waveguides [7] for operation at 1.55 μm. Their operation window can be extended to 2.5 μm by using GeSn. As tailoring the bandgap of CMOS compatible materials to make them absorb mid-infrared wavelengths is challenging and hasn't been achieved till date, these electro-absorption modulators can't be utilized for the mid-infrared wavelength range. One can then conclude that the best candidate for tuning and low-frequency modulation on a mid-infrared PIC is the thermo-optic effect. The implementation of a thermo-optic phase shifter is straightforward. The phase modulation introduced by the thermo-optic phase shifter can be translated to intensity modulation by incorporating the phase shifter in an interferometer. One drawback of thermo-optic modulators is that they are limited to lower speeds (KHz-MHz) however most mid-infrared measurement systems don't require higher modulation bandwidth. Therefore in this thesis, we have focused on the realization of low power consumption thermo-optic phase shifters.

5.2 Design of thermo-optic phase shifters

The operation principle of a thermo-optic phase shifter is straightforward. Heat is generated in the vicinity of the waveguide by passing current through a resistor. This heat leads to a temperature increase, which then alters the refractive index of the surrounding materials depending on their thermo-optic coefficient. The change in the refractive index of the materials is transferred directly to the effective index of the waveguide mode. If this waveguide is integrated in an interferometer such as in one arm of a MZI, the phase of the light traveling in that arm can be tailored as a function of the dissipated heat thereby leading to an intensity variation at the output. There are two configurations in which the heater can be placed as shown in Fig. 5.1 (a) and (b). While the first configuration requires the deposition of an intermediate cladding layer in between the heater and the waveguide [8], in the second configuration the heater is placed on one side of the waveguide which requires enough separation between the waveguide and the heater to avoid losses [9].

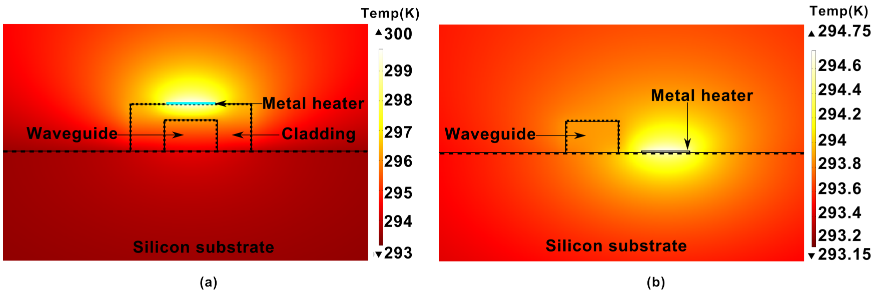

Figure 5.1: *Two schemes of placing a metal heater in the vicinity of the waveguide (a) Top heater and (b) side heater. The applied power to the heater in both the cases in 120 mW and the length of the heater was 700 μm.*

For the first approach (with metal heater on top) it's required that an intermediate cladding layer be deposited. This cladding should be transparent in the mid-infrared wavelength range and should also have sufficient thickness such that the optical mode in the waveguide is not absorbed by the metal. As described in chapter 2, chalcogenides can be made widely transparent in the mid-infrared wavelength range and their refractive index can be tailored as well. We carried out a simulation in FIMMWAVE to determine the required thickness of the cladding assuming a refractive index of 2. It can be seen in Fig. 5.2(a) that we would require a thickness of 1 μm to isolate the light traveling in the germanium core (assuming 5.3 μm wavelength in a waveguide of 2 μm height and 2.2 μm width) from the deposited metal (Ti(100 nm)/Au (20 nm)). We deposited Ti(100 nm)/Au (20 nm) heaters on GeSbSe chalcogenide films (provided by FotonLab, University of Rennes) and performed a VI measurement in order to obtain the maximum power which this heater could handle before burning. As seen in Fig. 5.2(b), the VI curve is fairly linear however after dissipating 120 mW, the heater of width 2 μm and length 700 μm got burned.
We carried out thermal simulations using COMSOL multiphysics, performing

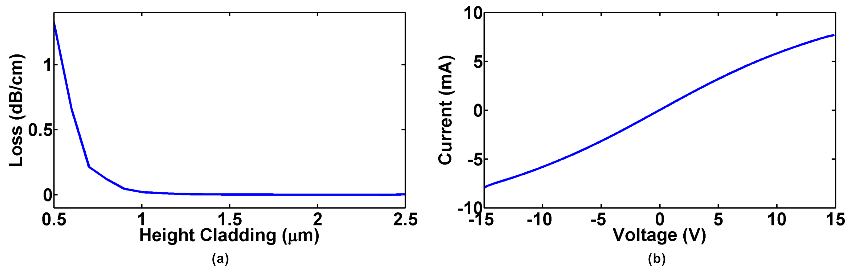

Figure 5.2: *(a) Fimmwave simulations showing the loss of the fundamental TM mode (by absorption from the top metal) as a function of cladding thickness and (b) measured VI curve of a Ti/Au heater placed on a chalcogenide film deposited on a silicon substrate.*

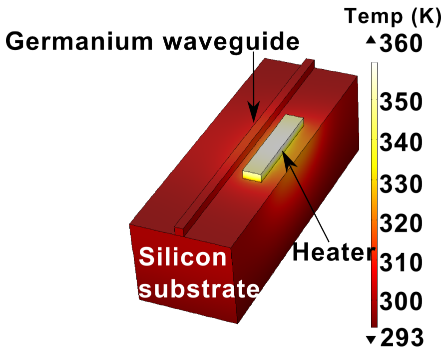

Figure 5.3: *Zoomed view of the simulation window showing the thermo-optic phase shifter in a side heating configuration. The spatial distribution of temperature in the waveguide can be seen. 700 mW of power was dissipated in the heater.*

steady state FEM 3-D simulations to calculate the temperature change as a function of dissipated power in the heater. It can be seen in Fig. 5.1 (a) and (b) that for both top and side heating configuration, if we dissipate 120 mW of power, the rise in temperature in the waveguide core is small leading to a phase shift of 0.2π and 0.1π respectively for a 700 μm long device structure. The top heater configuration has the additional problem that a transparent mid-infrared cladding is required and most probably will involve chalcogenides, the deposition of which is not CMOS compatible. We therefore designed the heaters in the side heating configuration with metal lines on top of a germanium strip. A zoomed in view of the simulation window can be seen in Fig. 5.3 which shows the spatial temperature distribution in the waveguide when a certain power is dissipated in the heater present next to it. In the simulations, we kept the silicon substrate

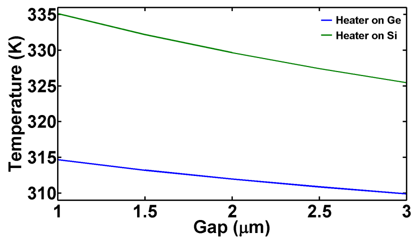

Figure 5.4: *Temperature in the center of the waveguide as a function of gap between the waveguide and center when the metal is placed on germanium strip (blue line) and when its placed on silicon substrate (green line). 700 mW of power was dissipated in the heater.*

and the top air cladding to be 200 μm high and 400 μm wide to take in account the heat sinking to the substrate. The length of the waveguide was kept 400 μm additional to the length of the heater to take in account the heat flow along the waveguide direction.

There are two ways to increase the efficiency of this side heater. Firstly, one can place the heater closer to the waveguide and as one can see in Fig. 5.4 that this would mean that the temperature in the waveguide core rises by ~5K if the gap is lowered to 1 μm from the value of 2 μm. As discussed in the previous chapter that a gap of 1 μm would lower the yield to ~5% due to limitations of our lithographic tool. Secondly, one can place the heater on the silicon substrate itself and as seen in Fig. 5.4 it would result in a temperature rise of ~20K for the same gap in comparison to the case when metal is deposited on germanium strip. For the first generation of our devices, we chose a gap of 2 μm between the waveguide and the heater to achieve a high yield of devices and placed the metal on a germanium strip instead of a silicon substrate. The improvements which would come from narrowing the distance between the heater and the waveguide and placing metal on a silicon substrate can be implemented in future designs. In order to test our phase shifters, we designed 1×2 MZIs with 25 nm FSR and the heater was placed on the longer arm as seen in Fig. 5.5(a). The heater itself consisted of a 2 μm wide metal stack of either Ti/Au or Cr/Au on a 4 μm wide Ge strip which is at a distance of 2 μm from the waveguide. The length of the heater was varied from 70 μm to 700 μm in steps of 70 μm and both the ends were connected to 100 μm × 100 μm pads which were probed by the electrical contacts. As shown in Fig. 5.5(b), the shift in the position of the destructive interference was used to calculate the phase shift as a function of dissipated power.

The temperature dependent thermo-optic coefficient of germanium has been experimentally determined in [10] and can be written as (T in Kelvin) in the form of following equation,

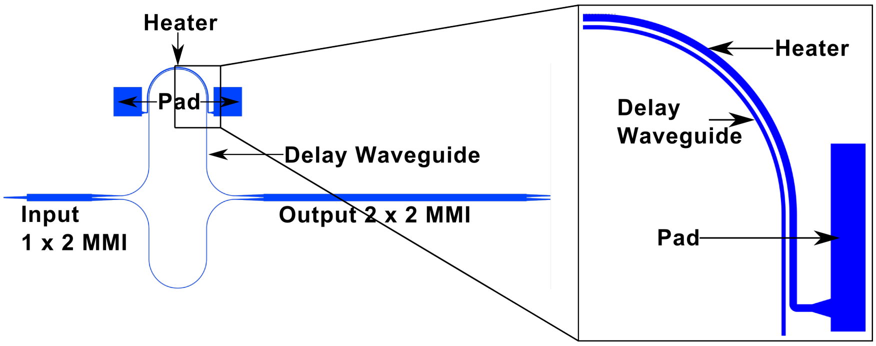

(a)

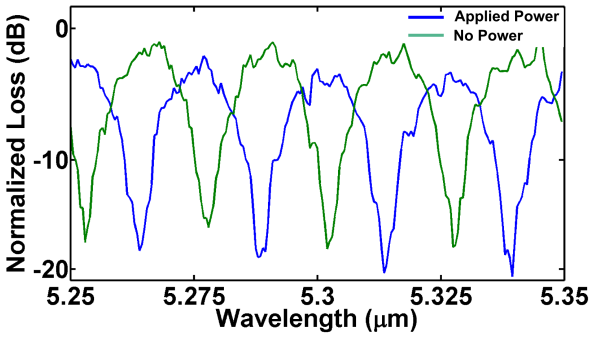

(b)

Figure 5.5: *(a) A schematic diagram showing the 1×2 MZI with heater in one of the arms along with the zoomed window showing the delay waveguide and the heater and (b) normalized spectra of the MZI with and without heater actuation. The dissipated power was 350 mW.*

$$\frac{dn}{dT} = 8.24.10^{-7}T + 0.000172 \tag{5.1}$$

Since the confinement of the optical mode in the germanium waveguide core is 96%, we only considered the thermo-optic effect in the Ge waveguide. In order to calculate the total phase change in a waveguide alongside the heater, we obtained the temperature profile along the length of the waveguide in the center as a line plot and then calculated the change in refractive index locally at each point using equation 5.1. The total phase change introduced in the heated waveguide can then be calculated by numerical integration as,

$$\Delta\phi = \int_0^L \frac{2\pi}{\lambda}\Delta n(z)dz \tag{5.2}$$

where λ is the wavelength of operation, Δn(z) is the change in the refractive index at a particular point and L is the total length of the waveguide.

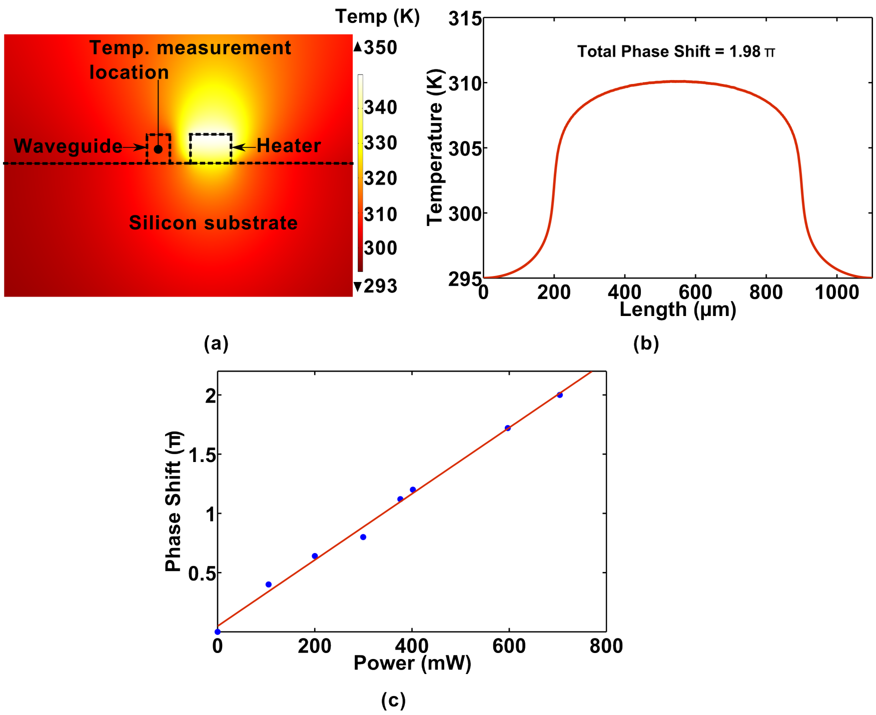

Figure 5.6: *(a) 2-D cross section in the middle of the simulation window, (b) line plot along the waveguide showing the temperature profile. The length of the heater was kept 700 μm and the power dissipated in the heater was 700 mW, (c) experimentally measured phase shift as a function of power dissipation along with a linear fit.*

5.3 Ge-on-Si phase shifters

5.3.1 Regular phase shifter

We performed a COMSOL simulation for the Ge-on-Si phase shifters as shown in Fig. 5.6(a) and found that one requires 700 mW (11 mA current and 64 V voltage) of power to achieve a 2π phase shift. The heater consisted of a stack of Ti/Au on a germanium strip, the length of which was kept 700 μm and the corresponding temperature profile in the center of the waveguide along its length can be seen in Fig. 5.6(b). This simulation was then confirmed by measuring the induced phase shift as a function of applied power as shown in Fig. 5.6(c). A good match between theory and experiment can be observed.
We can immediately draw the conclusion that a heater designed in this configuration is very power inefficient. The main reason behind this is that the underlying silicon (thermal conductivity = 130 W/(m*K)) acts as an efficient heat sink, which can also be seen in the simulation in Fig. 5.6. An improvement in the design is thus needed to bring down the required tuning power. Since the majority of the heat is being sunk in the silicon substrate, a way to improve the efficiency of the thermo-optic phase shifter is by thermally isolating it from the silicon substrate.

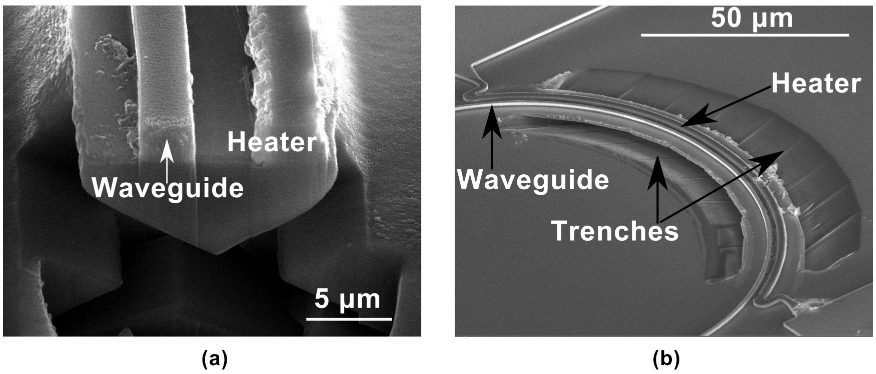

Figure 5.7: SEM image showing of (a) cross section of a fully undercut heater (the image is not of the measured device) and (b) top view of a fully undercut heater integrated in a MZI.

5.3.2 Fully undercut phase shifters

To prevent the heat to be sunk in the substrate, air trenches were created using a focused ion beam (FIB) tool on both sides of a heater/waveguide combination of length 210 μm as shown in Fig. 5.7(a). The rest of the chip was protected by photoresist and lithography was performed to define the areas where FIB is to be done. The total time taken to perform FIB was 8 hours. While in this prototype FIB was used, this undercutting can be realized on a wafer scale through chemically assisted ion beam etching. Fig. 5.7(b) shows the top view of the undercut heater (which consisted of a Ti/Au metal stack on a germanium strip) and the waveguide section. The simulated 2-D cross section and the temperature profile along the waveguide can be seen in Fig. 5.8(a) and Fig. 5.8(b) respectively. We confirmed the simulation results by measuring the phase shift as a function of applied power and found that 80 mW of power (2.5 mA current, 31.9 V voltage) is required to achieve a 2π phase shift as seen in Fig 5.8(c). The MZI normalized spectra is shown in Fig. 5.9 and it can be seen that both insertion loss and extinction ratio have not suffered.

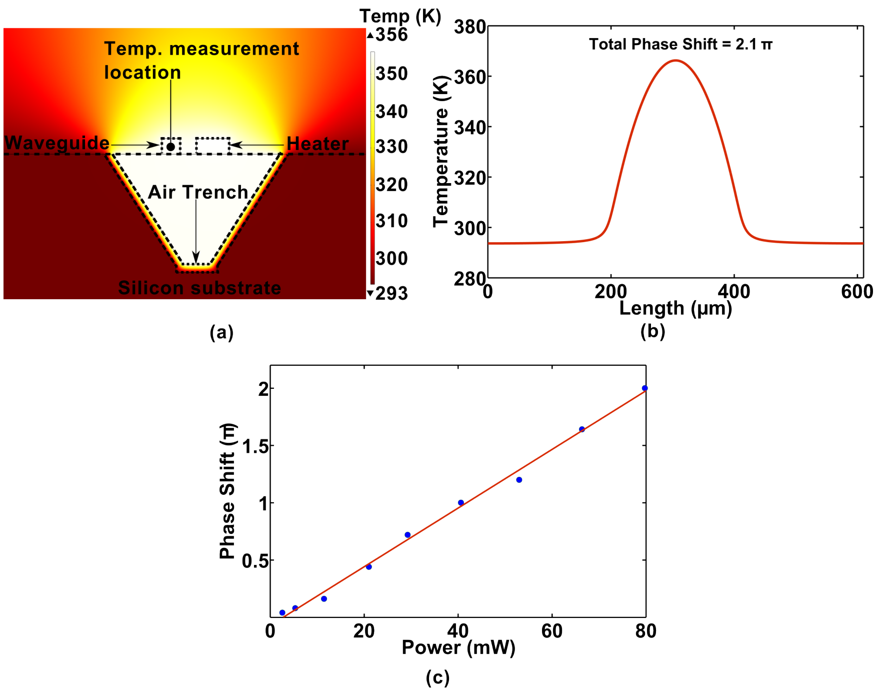

Figure 5.8: *(a) 2-D cross section in the middle of the simulation window, (b) line plot along the waveguide showing the temperature profile. The length of the heater was kept 210 μm and the power dissipated in the heater was 80 mW, (c) experimentally measured phase shift as a function of power dissipation along with the linear fit.*

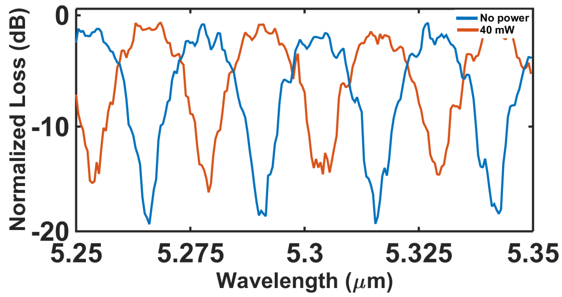

Figure 5.9: *Normalized spectra of the MZI with and without heater actuation after performing FIB.*

5.4 Ge-on-SOI

We have concluded in the previous sections that the introduction of an insulator between the heater and the silicon substrate will assist in confining the heat to the vicinity of the waveguide and hence increase the efficiency of the thermo-optic phase shifter. Although we have demonstrated a proof-of-principle concept using FIB, it remains a fact that this would be a rather time consuming process and although solutions like chemically assisted ion beam etching do exist, an elegant way would be to deliberately introduce a thermal insulator in the silicon substrate. SiO_2 is a known thermal insulator with thermal conductivity of 1.4 W/(m*K) and if we implement our phase shifters on Ge-on-Si-on-insulator, it could pave the way for the realization of efficient phase shifters with a relatively simple process flow. SiO_2 however has a disadvantage in the mid-infrared wavelength range as it absorbs strongly beyond 4 μm wavelength. Therefore, it must be ensured that the light traveling in the germanium waveguide is not absorbed by this underlying oxide. We calculated the absorption loss of the fundamental TM mode traveling in the waveguide core as a function of the bottom silicon cladding thickness as seen in Fig. 5.10(a) from which one can see that 3 μm silicon thickness is sufficient to achieve low loss propagation. The fabrication scheme of Ge-on-SOI phase shifters is described in Fig.3.6 in chapter 3. The waveguide loss for TM polarization of fully etched Ge-on-SOI single mode waveguides (2.2 μm wide and 2 μm high) was found to be 7 dB/cm in the 5.25 - 5.35 μm wavelength range as seen in Fig. 5.10(b). We tried to find the origin of these high losses by carrying out wet etching of 2 μm thick Ge films on SOI substrates in CrO_3:HF solution [11] for 5 minutes in order to reveal the threading dislocation density at different depths the results of which can be seen in Fig. 5.11. The defect density at various depths was found to be similar. However, comparing this image to Fig.4.8, one can see that the 2 μm thick Ge has no defects when grown on a Si substrate while there are defects present when

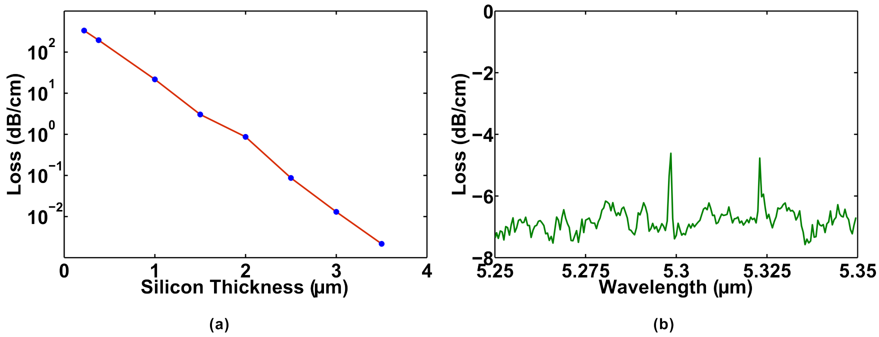

Figure 5.10: *(a) Simulated loss as a function of silicon thickness and (b) measured loss in 2.2 μm wide Ge-on-SOI waveguides.*

it's grown on SOI. This gives an indication that the germanium grown on a SOI substrate contains more defects than germanium grown on silicon substrate. This might point to the fact that the annealing conditions of the germanium layer need to be re-optimized for the case of Ge-on-SOI. Although the waveguide losses are higher compared to Ge-on-Si they are still low enough to realize mm scale integrated circuits.

5.4.1 Ge-on-SOI phase shifters

To evaluate the performance of the Ge-on-SOI phase shifters, we performed previously described COMSOL simulations, the results of which are shown in Fig. 5.12(a) and (b). Since the undercut by FIB was done on a 210 μm long heater, we measured the phase shift as a function of dissipated heat on a heater (consisting of a Ti/Au metal stack on a germanium strip) of similar length as shown in Fig. 5.12(c) and found that the results match well with the simulations in Fig. 5.12(b). To confine the heat in the vicinity of the heater/waveguide section, we etched 4 μm wide trenches in 3 μm thick silicon layer at a distance of 4 μm from the waveguide and the heater. A tuning power of 105 mW (13.5 mA current, 7.8 V voltage) was required to achieve a 2π phase shift. The heater performance as a function of length was also studied using COMSOL by calculating the tuning power required to achieve a phase shift of 2π and it was found that the power decays rapidly at first becoming almost constant for longer heaters as shown in Fig.. 5.13. This can be explained by the longitudinal flow of heat along the waveguide. As seen in the SEM image in Fig. 5.14(b), the heated waveguide is at its ends is connected to a 3.22 μm thick silicon slab (onto which the germanium waveguides are grown), which extends all over the circuit. This layer serves as an efficient heat spreader, which is the dominant source of heat sinking in the Ge-on-SOI phase shifters. This especially affects the shorter heaters

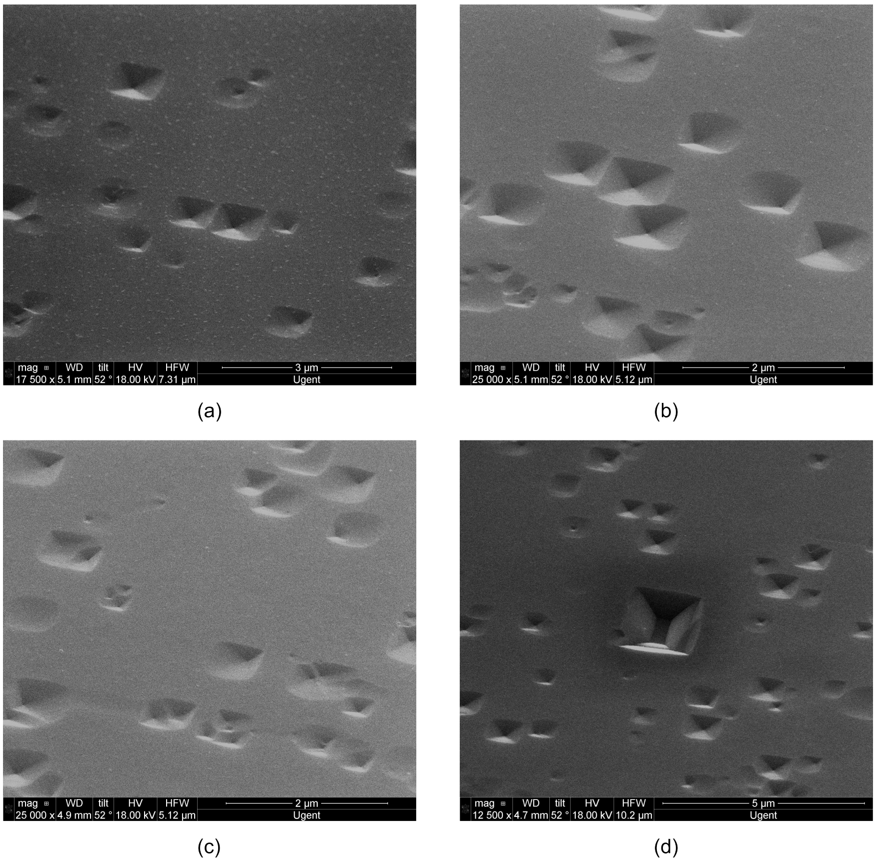

Figure 5.11: *Defects revealed in the 2 μm thick Ge-on-SOI film after wet etching. The Ge film was etched in RIE for (a) 0 minutes, (b) 5 minutes, (c) 10 minutes and (d) 14 minutes.*

since for longer devices the thermal resistance for the longitudinal heat flow becomes larger. This was also verified experimentally, the results of which are plotted together with the simulation results shown in Fig. 5.13.

5.4.2 Undercut Ge-on-SOI phase shifters

As described previously, the efficiency of the heater will increase if it is thermally isolated from the highly conducting silicon substrate. To enhance this, we removed the buried oxide using HF etching and carried out the measurements of the phase shift as a function of applied power for a heater of length 210 μm. The heaters consisted of a Cr/Au metal stack on a germanium strip. We chose Cr instead of Ti as Ti would be etched away by HF while performing the

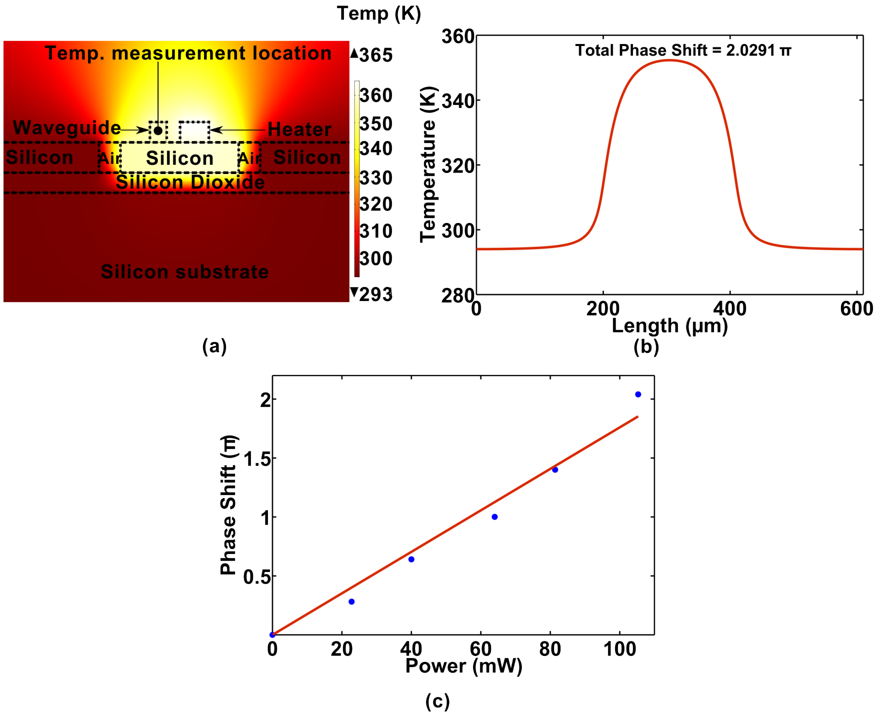

Figure 5.12: *(a) 2-D cross section in the middle of the simulation window, (b) line plot along the waveguide showing the temperature profile. The length of the heater was kept 210 μm and the power dissipated in the heater was 105 mW, (c) experimentally measured phase shift as a function of power dissipation along with the linear fit.*

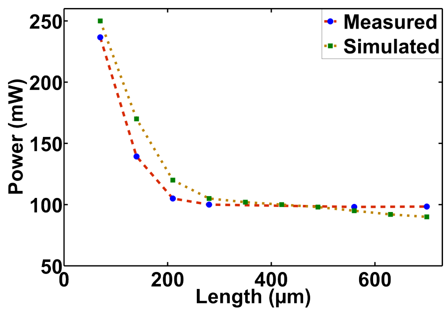

Figure 5.13: *Tuning power to achieve 2π phase shift as a function of length for a Ge-on-SOI phase shifter without undercut.*

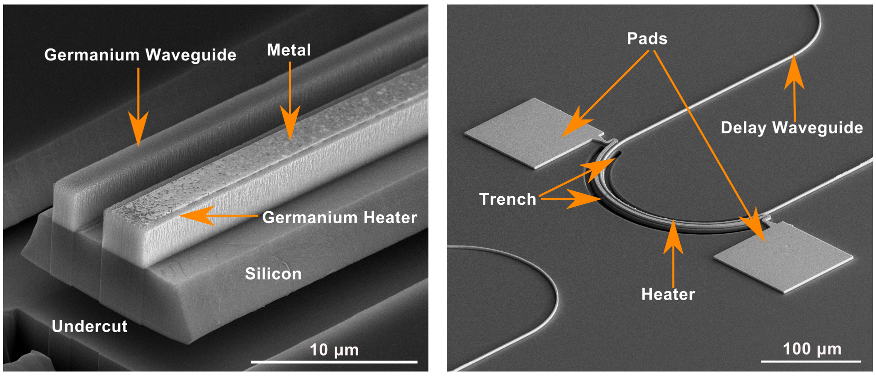

Figure 5.14: *SEM image showing (a) undercut Ge-on-SOI phase shifter and (b) the phase shifter integrated in one arm of the MZI.*

undercut. The COMSOL simulation in Fig. 5.15(a) and (b) suggest that a power of 20 mW would be needed to achieve the 2π phase shift, which is confirmed by the measurements in Fig 5.15(c). For heaters longer than 280 μm, it was observed that the free standing germanium waveguide and heater start bending and touch the substrate, which results in a parasitic heat sinking path, which hence again increases the required heating power as shown in Fig. 5.16. Taking into account this bending, the optimum configuration consists of a 280 μm long phase shifter, which dissipates 16 mW of power (3.2 mA current, 5.1 V voltage) for a 2π phase shift. The simulation of the tuning power required for a 2π phase shift as a function of heater length can also be seen in Fig. 5.16, which indicates that the graph would follow a similar trend as described in previous section, if the free standing section would not bend and touch the silicon substrate. Here the only heat flow is along the waveguide as the undercut completely isolates the heater from the silicon substrate underneath. The MZI normalized spectra after undercut are shown in Fig. 5.17 and it can be seen that both insertion loss and extinction ratio have not suffered.

5.5 Dynamic measurements

In the previous sections, we have focused on the DC operation of the thermo-optic phase shifters. Its also important to evaluate the AC response of phase shifters as that provides information regarding the maximal frequency of operation. In order to carry out this characterization, we provided the optical input as CW signal to the MZI and an alternating current was applied to the Ge-on-SOI undercut phase shifter. The duty cycle of the alternating current was fixed at 50% and the pulse width was varied. The output from the InSb detector in-

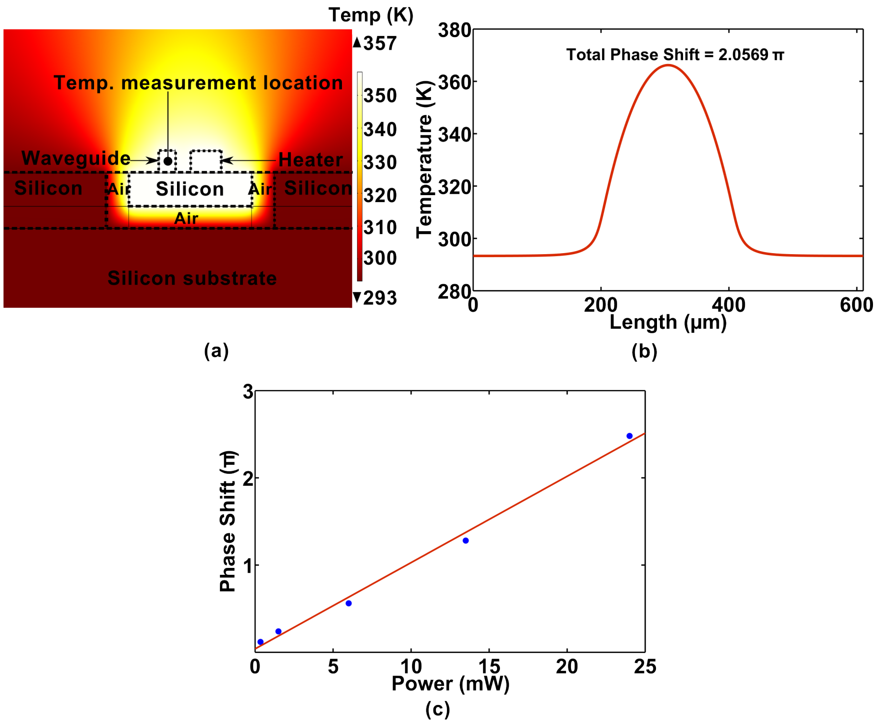

Figure 5.15: *(a) 2-D cross section in the middle of the simulation window, (b) line plot along the waveguide showing the temperature profile. The length of the heater was kept 210 μm and the power dissipated in the heater was 20 mW, (c) experimentally measured phase shift as a function of power dissipation along with the linear fit.*

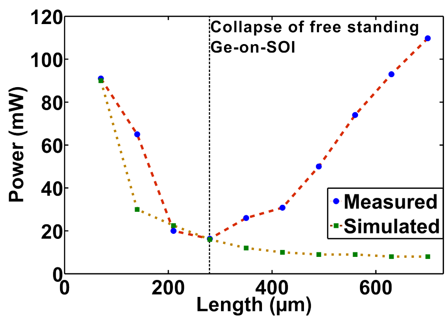

Figure 5.16: *Tuning power to achieve 2π phase shift as a function of length for a Ge-on-SOI phase shifter (a) without undercut and (b) with undercut.*

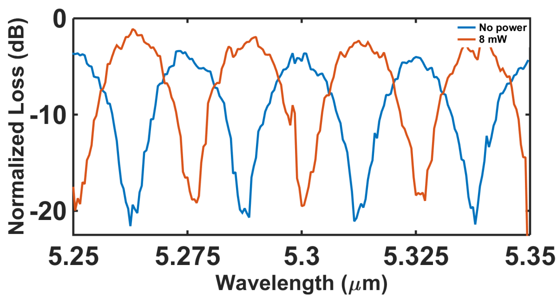

Figure 5.17: *Normalized spectra of the Ge-on-SOI MZI with and without heater actuation after performing undercut.*

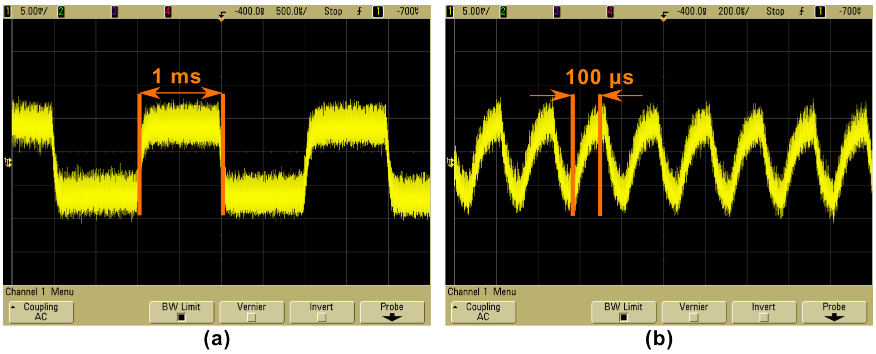

Figure 5.18: *AC response of the thermo-optic phase shifter (a) pulse width 1 ms and 50% duty cycle and (b) pulse width 100 μs and 50% duty cycle.*

side the FTIR was coupled to an oscilloscope which was used to study how the output changes as a function of current pulse width. The output of the detector as seen on the oscilloscope as a function of current pulse width is shown in Fig. 5.18. It can be seen that when the current pulse width is kept at 1 ms the output can follow the square pulse without any lag. However as we decrease the current pulse width to 100 μs, the output of the MZI starts to lag behind the applied alternating current and shows an exponential rise and fall.

In order to calculate the frequency of operation we analyzed the optical output when a 100 μs wide current pulse with 50% duty cycle was applied to the phase shifter as seen in Fig. 5.19(a). The frequency of operation is determined by carrying out an exponential fit to the rise and fall times respectively as seen in Fig. 5.19(b) and (c). The time constant from the exponential fit is calculated as 61 μs and 64 μs respectively which would translate in a frequency of operation of ~16 KHz which matches well with the recently demonstrated phase shifters in SOI working at 3.8 μm [12] where the -3 dB bandwidth is found out to be 23.8

KHz.

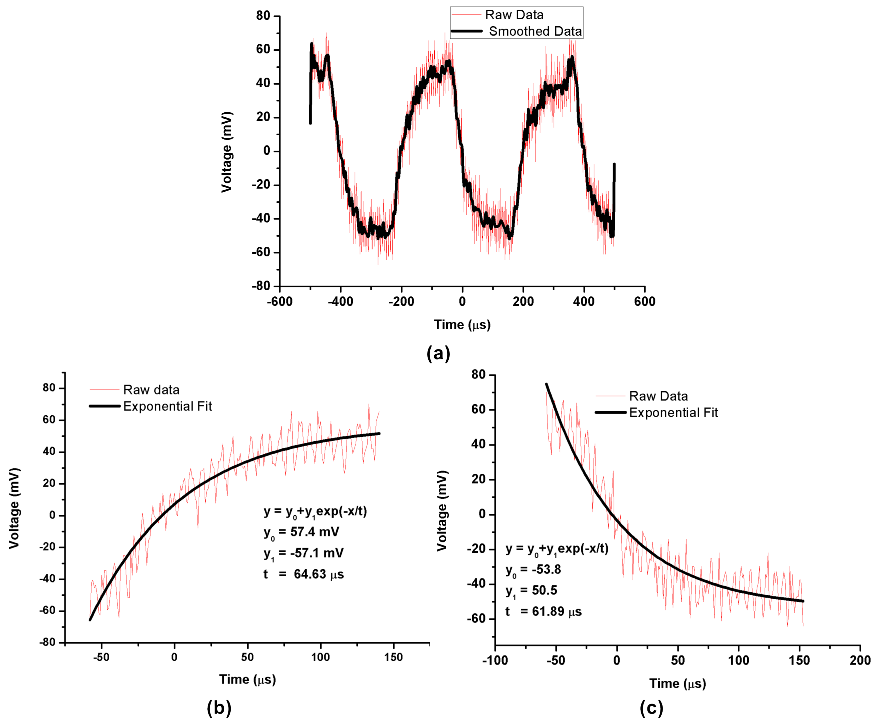

Figure 5.19: *(a) Analysis of the AC response of the thermo-optic phase shifter. The data smoothing is done using fast fourier transform. Exponential fit to determine the time constant for (b) rise and (c) fall of the output of the MZI.*

5.6 Conclusions

In this chapter we analyzed various configurations of thermo-optic phase shifters. In standard configuration, the power consumption for 2π phase tuning of a regular phase shifter is 700 mW as the heat produced is sunk in the silicon substrate. This makes it unattractive for usage in hand-held systems. We then demonstrated an efficient proof of principle phase shifter by introducing an air gap by FIB with power consumption of 80 mW. To enable mass manufacturing, an elegant solution in the form of Ge-on-SOI was proposed and the tuning power was found to be 105 mW. Finally Ge-on-SOI undercut phase shifters with 16 mW tuning power were demonstrated, fabricating which is possible on a large scale in a CMOS pilot line. The losses of the Ge-on-SOI waveguides are higher when compared to Ge-on-Si waveguides, however this issue can be addressed in the future with re-optimization of growth and annealing conditions. Also, the tuning power can be lowered further by placing the metal heaters on the silicon substrate and by providing support to the longer undercut heaters which would prevent bending and touching the silicon substrate.

References

[1] Robert G. Hunsperger. *Integrated Optics.* Springer, 2009.

[2] Graham T Reed, G Mashanovich, FY Gardes, and DJ Thomson. *Silicon optical modulators.* Nature photonics, 4(8):518–526, 2010.

[3] G Cocorullo and I Rendina. *Thermo-optical modulation at 1.5μm in silicon etalon.* Electronics Letters, 28(1):83–85, 1992.

[4] C. K. Tang and G.T. Reed. *Highly efficient optical phase modulator in SOI waveguides.* Electronics Letters, 31(6):451–452, Mar 1995.

[5] Ansheng Liu, Ling Liao, Doron Rubin, Hat Nguyen, Berkehan Ciftcioglu, Yoel Chetrit, Nahum Izhaky, and Mario Paniccia. *High-speed optical modulation based on carrier depletion in a silicon waveguide.* Optics Express, 15(2):660–668, 2007.

[6] Richard A Soref and B.R. Bennett. *Electrooptical effects in silicon.* IEEE Journal of Quantum Electronics,, 23(1):123–129, Jan 1987.

[7] Yu-Hsuan Kuo, Yong Kyu Lee, Yangsi Ge, Shen Ren, Jonathan E Roth, Theodore I Kamins, David AB Miller, and James S Harris. *Strong quantum-confined Stark effect in germanium quantum-well structures on silicon.* Nature, 437(7063):1334–1336, 2005.

[8] F Gan, T Barwicz, MA Popovic, MS Dahlem, CW Holzwarth, PT Rakich, HI Smith, EP Ippen, and FX Kartner. *Maximizing the thermo-optic tuning range of silicon photonic structures.* In Photonics in Switching, pages 67–68, 2007.

[9] Hui Yu, Marianna Pantouvaki, Sarvagya Dwivedi, Peter Verheyen, Guy Lepage, Roel Baets, Wim Bogaerts, Philippe Absil, and Joris Van Campenhout. *Compact thermally tunable silicon racetrack modulators based on an asymmetric waveguide.* Photonics Technology Letters, IEEE, 25(2):159–162, 2013.

[10] Bradley J Frey, Douglas B Leviton, and Timothy J Madison. *Temperature-dependent refractive index of silicon and germanium.* In Astronomical Telescopes and Instrumentation, pages 62732J–62732J. International Society for Optics and Photonics, 2006.

[11] Laurent Souriau, Tanya Atanasova, Valentina Terzieva, Alain Moussa, Matty Caymax, Roger Loo, Marc Meuris, and Wilfried Vandervorst. *Characterization of threading dislocations in thin germanium layers by defect*

etching: Toward chromium and HF-Free solution. Journal of The Electrochemical Society, 155(9):H677–H681, 2008.

[12] Milos Nedeljkovic, Stevan Stankovic, Colin J Mitchell, Ali Z Khokhar, Scott A Reynolds, David J Thomson, Frederic Y Gardes, Callum G Littlejohns, Graham T Reed, and Goran Z Mashanovich. *Mid-infrared thermo-optic modulators in SoI.* IEEE Photonics Technology Letters, 26(13):1352–1355, 2014.

6

Conclusions & Future Prospects

“His burden didn’t feel any lighter, but he felt strong enough to carry it."

– Amish

6.1 Conclusions

In this thesis we began by outlining the importance of the mid-ir wavelength range for spectroscopic sensing. Although the light source required to perform sensing has come down to a chip scale because of the invention of QCLs and ICLs, the tuning mechanism to realize operation over a wide wavelength range either consists of a moving grating to select the desired wavelength from a broad-band gain medium or a combination of lens and grating to combine various wavelengths emitted from an array of DFB lasers. These mechanisms make the entire system bulky and hence not appealing for hand-held usage. Since the absorption features often are spread over a large wavelength range (3-12 μm), these tuning mechanisms are needed and contribute a major cost towards the final system. Photonic integration has enabled implementation of various optical functionalities on a SOI semiconductor chip and together with integration with active III-V materials, its possible to realize miniature lasers working in the telecom wavelength range. The SOI waveguide platform has become attractive because of the mass manufacturing capabilities and hence the associated low cost. One can then conclude that the desirable waveguide platform for mid-infrared devices should have (a) a wide transparency range, (b) CMOS compatibility, and (c) a fabrication scheme with high yield.
A literature review reveals that beyond 4 μm, the SOI waveguide platform would become excessively lossy because of the underlying oxide absorption. Several waveguide platforms have been investigated by researchers worldwide most of which try to take advantage of the wide transparency of silicon and the fact that silicon processing is understood in great detail. Many of these waveguide platforms (e.g. free standing silicon, silicon on saphire, silicon on silicon nitride, silicon on CaF_2) replace the lossy underlying silicon dioxide by a mid-IR transparent cladding however either the fabrication scheme remains complicated resulting in a lower yield or transparency is limited as the cladding starts to absorb after a certain wavelength. Another possibility is the usage of mid-ir transparent materials such as chalcogenides which allow one to tune both the refractive index and the transparency window. However a major shortcoming of this waveguide platform is that its not CMOS compatible and hence mass manufacturing at a low cost is difficult. Germanium-on-silicon fits the above mentioned three requirements and hence offers a potential replacement for SOI in the mid-ir wavelength range.
The fabrication flow of Ge-on-Si waveguides starts with the epitaxial growth of a germanium film on a 200 mm silicon wafer in imec. The grown film was annealed to reduce the TDD. Lithography and dry etching were then carried out in a CF_4:O_2 plasma in RIE using a metal (Ti/Cr) mask. Ideally one would like to use a dielectric or photoresist mask in order to avoid possible metal contamina-

tion and the side wall roughness, which is introduced in the metal mask while performing lift-off. It was found that the selectivity of either the dielectric or the photoresist mask is not enough to completely etch a 2 μm thick germanium film. This issue however can be tackled by adapting different etching recipes involving CF_4:O_2:H_2 plasma or a Cl_2:N_2 plasma. It can be concluded that access to better tools would reduce the minimum definable feature size and the side wall roughness as well.

Various integrated photonic devices were realized in the course of this thesis, the first of which were low loss waveguides. It was found that the waveguides exhibit a loss in range of 3-4 dB/cm in the 5.15 μm-5.45 μm wavelength range for both TE and TM polarization. The origin of the waveguide loss comes from the side wall roughness and the defects present at the Ge-Si interface. In order to further reduce, one can either design a waveguide with larger core (in order to have minimal overlap with the defective interface) or reduce the side wall roughness as discussed in the last paragraph. Wavelength filtering devices like 1×1 and 1×2 MZIs were designed and found to have an extinction of 20 dB. Also wavelength (de)multiplexers in the form of a five channel 200 GHz AWG was realized and the insertion loss was found to be 2.5/3.1 dB for TE and TM polarization respectively with cross talk levels of 16 dB and 20 dB. A six channel PCG with 25 nm channel spacing was also realized with an insertion loss of 4.2/4.9 dB for TE and TM polarization respectively with cross talk levels of 22 dB and 23 dB. The performance of the wavelength (de)multiplexers would improve with a better processing scheme which allows for the definition of narrow waveguides with low side wall roughness. The narrow feature size would reduce the AWG and PCG insertion loss as less light would be lost in the star coupler in the first case and also allow to realize a DBR mirror in a PCG with higher reflectivity. The side wall roughness reduction would result in less phase errors in the AWG waveguide array improving the cross talk. One can then conclude that development of a new lithography and etching recipe would improve the performance of these devices.

Tuning of wavelength selective filters is also a desirable functionality in PICs. An easy way of achieving this functionality is by using the thermo-optic effect where heat is applied in the vicinity of the waveguide to alter the effective index of the propagating mode. However realizing an efficient thermo-optic phase shifter is challenging in Ge-on-Si waveguides as silicon acts as a heat sink which translates in a required power of 700 mW for a 2π phase shift. This tuning power can be brought down to 80 mW after introducing an air gap between the waveguide and the silicon substrate by the means of FIB. An elegant way of achieving lower tuning power levels is using Ge-on-SOI waveguides where the underlying oxide prevents the heat from dissipating in the silicon substrate and thus brings down the tuning power to 105 mW. This tuning power can further be

reduced to 16 mW if the underlying oxide is removed by wet etching. Although the tuning power is reduced by a factor of ~40, it was found that the waveguide loss of Ge-on-SOI waveguides is 7dB/cm which is higher than that of Ge-on-Si waveguides. This high loss might be related to the non-optimal annealing conditions. Its clear from this discussion that efficient thermo-optic phase shifters can be realized in Ge-on-SOI waveguides whose growth condition can be optimized in the future to achieve lower propagation losses. The waveguide propagation loss would also benefit from a fabrication scheme which reduces the side wall roughness and overlap with defective interface as has been discussed in previous paragraphs.
From the discussion above, it can be concluded that the Ge-on-Si waveguide platform is indeed appealing for realizing integrated waveguide circuits working in the mid-ir wavelength range. There is room for improvement in the current fabrication scheme which would bring down the waveguide losses and moreover improve the performance of the realized devices.

6.2 Short term prospects

There are several improvements which can be done in a relatively short term to improve the performance of the waveguide circuits fabricated in this thesis. Some of them are listed below.

1. **Waveguide loss reduction** Several solutions exist for lowering the waveguide losses, the most obvious being improving the fabrication process to reduce the side wall roughness. Another possibility is using a 4 μm thick germanium film and realizing partially etched (2 μm) waveguides. This would reduce the overlap of the mode with the defective interface. Also, ALD of mid-ir transparent oxides such as HfO_2 can be carried out to passivate the fabricated waveguides and reduce any loss coming from native oxide formation.

2. **Different etch depths** In order to reduce the overall footprint of the device, one can conceptualize about deeply etching the waveguide in the bends in order to increase the compactness of the waveguide circuit. It would be appealing therefore to combine different etch depths as done in SOI waveguide circuits to take leverage of low loss shallow etched waveguides and sharper bends. Also, a deep etch would improve the reflectivity of the DBR mirrors used in PCGs hence reducing the insertion loss.

3. **Increasing the efficiency of thermo-optic phase shifters** The efficiency of thermo-optic phase shifters can further be enhanced by placing the metal heaters directly on silicon. To avoid bending of free standing

heaters larger than 280 μm, tethers can be defined in the silicon bottom cladding.

4. **Realizing a flat top wavelength (de)multiplexer** The wavelength (de)multiplexer realized in this thesis had a gaussian output. Therefore,if the DFB laser is thermally tuned, the output power after passing through the multiplexer would substantially vary. In order to avoid this non-uniformity, one can realize a flat top AWG or PCG by replacing the input aperture by a MMI [1].

6.3 Long term prospects

In the previous chapters we have seen that Ge-on-Si is an attractive platform for mid-ir integration as compared to other (CMOS compatible) waveguide platforms. We have also discussed the fabrication flow which can be integrated in a standard CMOS pilot line with minimal technological development. We also demonstrated passive waveguide devices and have shown efficient tuning.
As discussed in the introductory chapter, the advantage of photonic integration for the mid-ir wavelength range is that it allows for miniaturization of laser modules or complete sensing systems. These systems will not only need passive waveguide devices as shown in this thesis but would also require the integration of a light source. For telecom wavelengths, the integration of light sources is achieved by bonding the III-V epitaxial stack to the SOI dies. One can either use molecular bonding [2], where two wafers are attached to each other by Van der Waals forces or by using a glue like benzocyclobutene (BCB) [3]. Usage of BCB to heterogeneously integrate the III-V dies relaxes the fabrication process in terms of cleanliness of sample surfaces as particles with height less than the glue thickness can be covered easily. It also doesn't require planarization as the glue itself can fill in trenches. There are however two issues associated with BCB which could prevent its usage in the mid-ir wavelength range

1. **Absorption of light:** BCB is transparent for telecom wavelengths and thus doesn't pose any challenges in designing of photonic circuits however it starts to absorb in the mid-ir wavelength range as seen in Fig. 6.1. It can therefore be deducted that one can't use BCB as a bonding agent for the mid-ir wavelength range. Moreover it would be difficult to find other polymer based glues transparent in the mid-ir laser integration as most polymers contain hydrocarbons which are the primary source of absorption.

2. **Heat sinking:** Another major issue with using BCB for mid-ir opto-electronic components is heat management. QCLs are power hungry devices consuming power in the range of several watts and effective heat management is an issue for QCL operation. Usage of BCB or any other

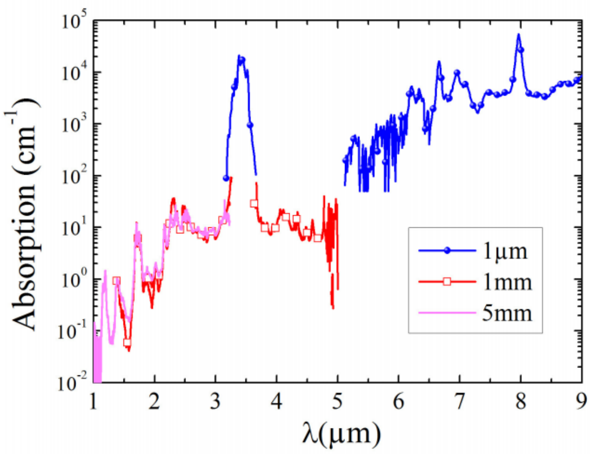

Figure 6.1: *Graph showing BCB absorption as a function of wavelength (from [4]). 1 mm and 0.5 mm path lengths are obtained by putting BCB in a cuvette while 1 μm path length is obtained by spin coating on a KBr window.*

polymer would prevent heat sinking in the highly conducting substrate and hence the device wouldn't perform optimally. Adhesive bonding can however be considered for lower power consumption ICLs.

As future work we therefore would propose to focus on the integration of ICLs and QCLs on Ge-on-Si waveguide circuits as discussed below.

6.3.1 Integration of ICLs for trace gas sensing

We discussed the usage of ICLs as mid-ir light sources particularly in the 3-6 μm wavelength range. ICLs consume less power as compared to QCLs. One application of integrated ICLs with passive waveguide circuits could be the detection of trace gases using the scheme as shown in Fig. 1.13. The integration could be carried out using molecular bonding of the ICL III-V epitaxial stack and then processing the lasers after integration. Even in this case BCB bonding can still be considered by either using very thin bonding layer or by making sure that the coupling section between the III-V waveguide and the germanium waveguide is free of BCB. In order to realize cost effective mass manufacturing, transfer printing can also be used. Transfer printing involves transfer of III-V layers in desired area on substrates such as silicon [5], [6] and bonding using Van der Waals forces. One can transfer hundreds of III-V coupons in one step thus making the entire process cost effective. Also, the yield remains quite high

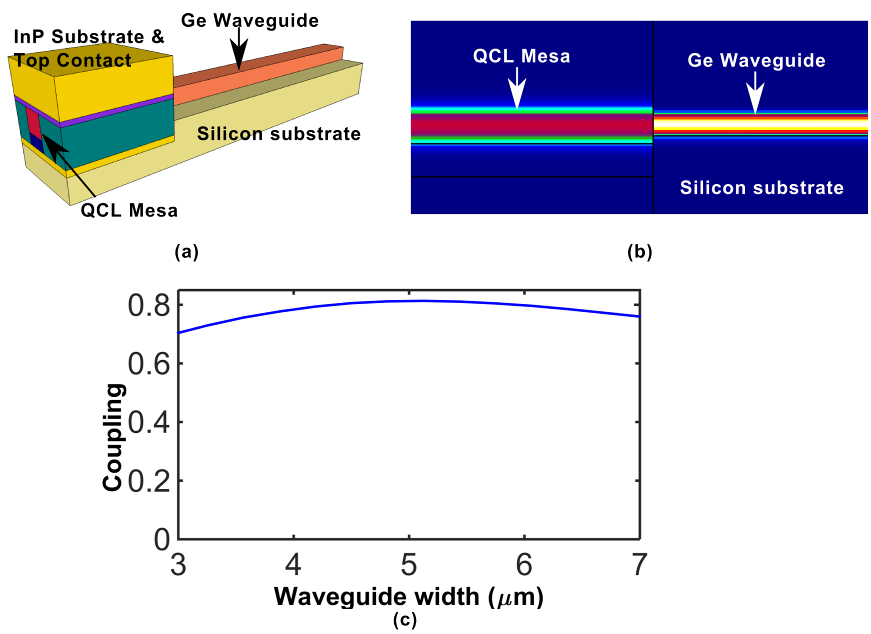

Figure 6.2: *(a) Schematic diagram showing butt coupling of a fabry-perot QCL with a Ge-on-Si waveguide circuit, (b) FIMMWAVE simulation showing the side view of light getting coupled in a germanium waveguide from a QCL and (c) coupling efficiency as a function of germanium waveguide width.*

because a defect arising from a contaminant particle would affect only the particular coupon.

6.3.2 Integration of QCLs for remote sensing & glucose monitoring

We pointed out in the first chapter that there are windows in the mid-ir wavelength regime in which the atmosphere is transparent. Remote sensing can pave the way for the detection of dangerous substances such as explosives (e.g. HMX).

The realization of an integrated widely tunable QCL could result in making this system truly hand-held. The integration could be done by butt-coupling a Fabry-Perot QCL laser to a tapered germanium-on-silicon waveguide. We carried out simulations on the coupling of the fundamental TM mode from the QCL mesa (design provided by University of Sheffield) to the germanium taper using FIMMWAVE and the results are plotted in Fig. 6.2 (c). It can be seen

that one can obtain ~80% coupling efficiency which makes butt-coupling an attractive option for integration.
Another application of integrated widely tunable QCLs could be in the area of glucose monitoring. As shown in Fig. 1.4(b), glucose has an absorption band in the 10 μm wavelength range. Presently glucose sensing has been carried out using EC-QCLs and a photo-acoustic cell which makes the implementation of the system difficult in a hand-held situation. Butt coupling a Fabry-Perot QCL with a germanium-on-silicon waveguide circuit would again allow for a low-cost hand-held device. However the thickness of the germanium layer would have to be increased in order to confine the optical mode. First experiments on 4 μm thick germanium-on-silicon waveguide circuits are currently ongoing.

6.4 Specifications required to realize tunable mid-ir light sources

As we described in chapter 1, the PICs working in the mid-ir wavelength range would be used in realizing an integrated light source. Two schemes were discussed which involved either providing feedback from the PIC to a broad band III-V gain chip or combining the output of an array of DFB lasers. In the first scheme, we discussed that 10% reflectivity is required to achieve low threshold operation. This includes the coupling to and from the chip and the insertion loss of the filter. As seen in Fig. 6.2(c), the coupling equals ~80%, which results in an allowable insertion loss of the filter of 8 dB. As realization of the high-Q ring resonators has not been possible in this thesis, we cannot comment on the required specifications for the configuration shown in Fig.1.10. However the cascaded MZI based wavelength filter can be realized. A simulation of a three-stage cascaded filter is shown in Fig. 6.3 and it can be seen that the overall loss from the delay lines is 1.8 dB (assuming a 3 dB/cm propagation loss). From the measurements performed, the excess insertion loss of the individual MZI is found to be 0.5 dB. This would mean a total round trip insertion loss of 6.6 dB which is acceptable for our system. If one considers Ge-on-SOI waveguides which have higher losses (7 dB/cm), then the total insertion loss would increase to 11.6 dB.
For combining the output of various DFB lasers, 1 dB of light is lost in coupling from the laser array. One can put an upper bound of 3 dB for the insertion loss of the (de)multiplexer itself bringing the total insertion loss to 4 dB. This would mean that the AWGs fabricated in this thesis are suitable for the use in such a scheme while the PCGs would need fabrication of higher reflectivity gratings in order to reduce their insertion loss. The fabricated AWGs and PCGs had a gaussian channel profile and as discussed above, one would like to get a flat top

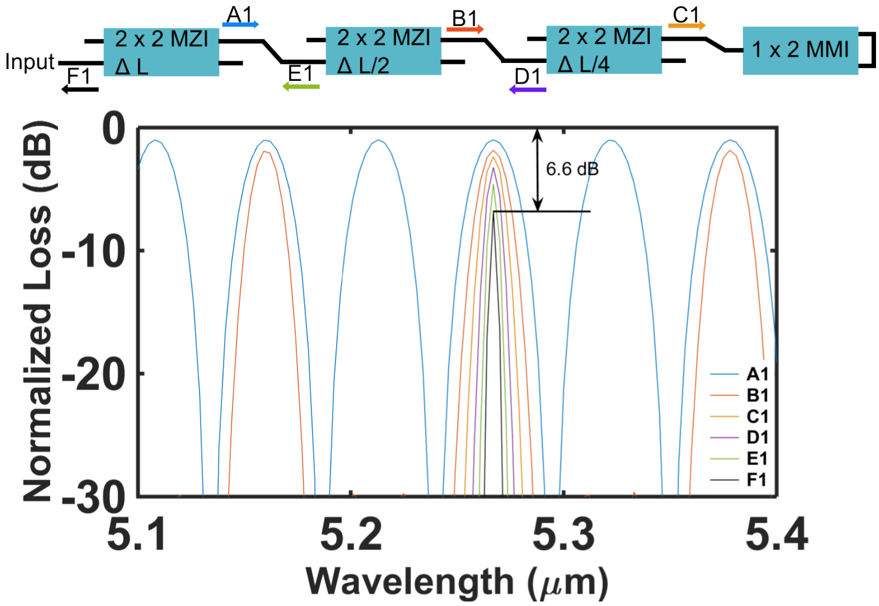

Figure 6.3: *Simulated response of a three stage cascaded MZI assuming a 3 dB/cm loss in the waveguides. ΔL was chosen to be 120 μm.*

response to get power variations when going away from the center of the pass-bands. However a flat top response would mean that the insertion loss would increase and hence the fabricated wavelength (de)multiplexers would need to be improved.

It can be concluded from this thesis that germanium-on-silicon has the potential to realize many interesting functionalities in the mid-ir wavelength range. The advent of SOI waveguides has dramatically reduced the size and cost of devices operating at telecom wavelengths and Ge-on-Si can play the same role for mid-infrared wavelengths. This waveguide platform can be transfered to a CMOS pilot line which would make mass manufacturing a possibility. One can expect even better performance of the waveguide devices fabricated in a CMOS pilot line because of better lithographic tools and etching recipes.

References

[1] S. Pathak, M. Vanslembrouck, P. Dumon, D. Van Thourhout, and W. Bogaerts. *Optimized Silicon AWG With Flattened Spectral Response Using an MMI Aperture*. Lightwave Technology, Journal of, 31(1):87–93, Jan 2013.

[2] Di Liang, Alexander W Fang, Hyundai Park, Tom E Reynolds, Keith Warner, Douglas C Oakley, and John E Bowers. *Low-temperature, strong SiO2-SiO2 covalent wafer bonding for III–V compound semiconductors-to-silicon photonic integrated circuits*. Journal of Electronic Materials, 37(10):1552–1559, 2008.

[3] Günther Roelkens, Dries Van Thourhout, Roel Baets, M Smit, et al. *Laser emission and photodetection in an InP/InGaAsP layer integrated on and coupled to a Silicon-on-Insulator waveguide circuit*. Optics Express, 14(18):8154–8159, 2006.

[4] Alban Gassenq, Nannicha Hattasan, Laurent Cerutti, Jean Batiste Rodriguez, Eric Tournie, and Gunther Roelkens. *Study of evanescently-coupled and grating-assisted GaInAsSb photodiodes integrated on a silicon photonic chip*. Optics Express, 20(11):11665–11672, 2012.

[5] John Justice, Chris Bower, Matthew Meitl, Marcus B Mooney, Mark A Gubbins, and Brian Corbett. *Wafer-scale integration of group III-V lasers on silicon using transfer printing of epitaxial layers*. Nature Photonics, 6(9):610–614, 2012.

[6] Hongjun Yang, Deyin Zhao, Santhad Chuwongin, Jung-Hun Seo, Weiquan Yang, Yichen Shuai, Jesper Berggren, Mattias Hammar, Zhenqiang Ma, and Weidong Zhou. *Transfer-printed stacked nanomembrane lasers on silicon*. Nature Photonics, 6(9):615–620, 2012.

A

Processing Steps

A.1 Introduction

In chapter 3 we discussed about the fabrication steps for the germanium-on-silicon waveguide circuits. However to keep the text clear and not to burden the reader with additional details, we didn't provide details of the exact parameters used in fabrication. Therefore in this appendix we include a detailed list of all the parameters used for defining the germanium-on-silicon waveguide circuits.

A.1.1 Definition of waveguide circuits

To define the waveguide circuits, we performed the following steps.

1. Cleave the wafer received from imec in desired size.
2. Remove the thin photoresist by a acetone, IPA, DI water rinse and blow dry with nitrogen.
3. Remove the thin (~30 nm) SiO_2 by a 30 second dip in BHF.
4. Rinse for alleast 5 minutes in DI water and blow dry.
5. Put on hot plate at 100° for 5 minutes. Do not use higher temperature as that would lead in resist tearing.
6. Spin coat AZ 5214 photoresist at 3000 rpm for 40 seconds.
7. Bake on hot plate at 100° for 3 minutes.
8. Expose the resist through mask in MA6 for 12 seconds.
9. Bake on hot plate for 120° for 3 minutes.
10. Flood expose for 50 seconds.
11. Develop in 1:4 (AZ400 developer:DI water) for 32 seconds.
12. Perform metalization (20 nm Ti-100 nm Cr)in e-gun.
13. Perform liftoff in DMSO at 80°.
14. Load the samples in RIE and etch using recipe 'Ge CF4 10 mtorr' for 15 minutes. Adjust the power to be 600 mW, CF_4 flow to be 40 sccm and O_2 flow to be 10 sccm.
15. Spin coat AZ9026 photoresist at 1000 rpm for 20 seconds.
16. Bake on hot plate at 120° for 3 minutes.

17. Load the sample on lapmaster and perform lapping for ~20 minutes to thin the substrate to ~300 μm.
18. Rinse the photoresist with acetone, IPA and DI water and blow dry.
19. Remove the metal hard mask by performing a 30 minute dip in 40% HF.
20. Spin coat AZ5214 at 3000 rpm for 40 seconds.
21. Bake at 120° for 3 minutes.
22. Cleave the sample at desired location.
23. Rinse the photoresist with acetone, IPA, DI water and blow dry.

A.1.2 Definition of metal lines on top of germanium strips

To define metal lines on top of germanium waveguides for heaters, perform the above mentioned steps till step 14, then perform step 19 to remove the metal. After that follow the undermentioned steps,

1. Bake at 100° for 3 minutes.
2. Spin coat Ti-prime adhesion promoter for 40 seconds at 3000 rpm.
3. Bake at 120° for 3 minutes.
4. Spin coat Ti-35 E at 3000 rpm for 40 second.
5. Bake at 100° for 3 minutes.
6. Expose for 55 seconds through mask in MA6.
7. Wait for alteast 10 minutes.
8. Bake at 123° for 2 minutes.
9. Flood expose for 185 seconds.
10. Develop in 1:3 solution of AZ400:DI water for 1 minute.
11. Load in e-gun to deposit metal (Ti-Au in case no undercut is done and Cr-Au in case undercut is done).
12. Perform liftoff in DMSO at 80° for ~15 minutes.

Perform steps 20-23 in the previous section if no undercut has to be done. For undercut, see the next section.

A.1.3 Definition of trenches in silicon substrate

To etch trenches in silicon substrate to access the underlying oxide follow the steps in above mentioned section. After that follow these steps,

1. Spin coat Ti-prime adhesion promoter for 40 seconds at 3000 rpm.
2. Bake at 120° for 3 minutes.
3. Spin coat photoresist AZ9026 at 5000 rpm for 40 seconds.
4. Bake at 110° for 3 minutes.
5. Expose for 200 seconds through mask in MA6.
6. Develop in 1:3 solution of AZ400:DI water for 2 minutes.
7. Postbake at 120° for 2 minutes.

B

List of publications

B.1 Publications in international journals

1. A.Malik, S. Dwivedi, L. Van Landschoot, M. Muneeb, Y. Shimura, G. Lepage, J. Van Campenhout, W. Vanherle, T. Van Opstal, R. Loo, G. Roelkens, "Ge-on-Si and Ge-on-SOI thermo-optic phase shifters for the mid-infrared", Optics Express, 22(23), pp. 28479-28488 (2014).

2. M. Muneeb, A. Ruocco, A.Malik, S. Pathak, E.M.P. Ryckeboer, D. Sanchez, L. Cerutti, J.B. Rodriguez, E. Tournie, M. Smit, G. Roelkens, "Silicon-on-insulator shortwave infrared wavelength meter with integrated photodiodes for on-chip laser monitoring", Optics Express, 22(22), pp. 27300-27308 (2014).

3. G. Roelkens, U.D. Dave, A. Gassenq, N. Hattasan, C. Hu, B. Kuyken, F. Leo, A.Malik, M. Muneeb, E.M.P. Ryckeboer, D. Sanchez, S. Uvin, Z. Hens, R. Baets, Y. Shimura, F. Gencarelli, B. Vincent, R. Loo, J. Van Campenhout, L. Cerutti, J.B. Rodriguez, E. Tournie, X. Chen, M. Nedeljkovic, G. Mashanovich, L. shen, N. Healy, A. Peacock, X. Liu, R. Osgood, W.M.J. Green, "Silicon-based photonic integration beyond the telecommunication wavelength range", IEEE Journal of Selected Topics in Quantum Electronics, 20(4), pp. 8201511 (2014).

4. A.Malik, M. Muneeb, Y.Shimura, J. Van Campenhout, R.Loo, G. Roelkens, "Germanium-on-Silicon Planar Concave Grating Wavelength (de)multiplexers in the Mid-Infrared", Applied Physics Letters, 103(16), pp. 161119 (2013).

5. A.Malik, M. Muneeb, S. Pathak, Y.Shimura, J. Van Campenhout, R.Loo, G. Roelkens, "Germanium-on-Silicon Mid-infrared Arrayed Waveguide Grating Multiplexers", IEEE Photonics Technology Letters, 25(18), pp. 1805-1808 (2013).

6. G. Roelkens, U.D. Dave, A. Gassenq, N. Hattasan, C. Hu, B. Kuyken, F. Leo, A.Malik, M. Muneeb, E.M.P. Ryckeboer, S. Uvin, Z. Hens, R. Baets, "silicon-based heterogeneous photonic integrated circuits for the mid-infrared", Optical Materials Express, 3(9), pp. 1523-1536 (2013).

7. M. Muneeb, X. Chen, P. Verheyen, G. Lepage, S. Pathak, E.M.P. Ryckeboer, A.Malik, B. Kuyken, M. Nedeljkovic, J. Van Campenhout, G. Mashanovich, G. Roelkens, "Demonstration of silicon on insulator mid-infrared spectrometers operating at 3.8um", Optics Express, 21(10), pp. 11659-11669 (2013).

B.2 Publications in international conferences

1. Z. Wang, A. Malik, B. Tian, M. Muneeb, Clement Merckling, Marianna Pantouvaki, Yosuke Shimura, Roger Loo, Joris Van Campenhout, D. Van Thourhout, G. Roelkens, "Near/Mid-Infrared Heterogeneous Si Photonics", The 9th International Conference On Silicon Epitaxy And Heterostructures.

2. J.S.Penades, Y.Hu, M.Nedeljkovic, C. G. Littlejohns, A. Z. Khokhar, A. Malik, G. Roelkens, F. Y. Gardes, G. Z. Mashanovich, "Angled MMI CWDM structure on Germanium on Silicon", submitted for publication in CLEO Europe.

3. G. Roelkens, U.D. Dave, A. Gassenq, N. Hattasan, C. Hu, B. Kuyken, F. Leo, A.Malik, M. Muneeb, E.M.P. Ryckeboer, D. Sanchez, S. Uvin, R. Wang, Z. Hens, R. Baets, Y. Shimura, F. Gencarelli, B. Vincent, R. Loo, J. Van Campenhout, L. Cerutti, J.B. Rodriguez, E. Tournie, X. Chen, M. Nedeljkovic, G. Mashanovich, L. shen, N. Healy, A. Peacock, X. Liu, R. Osgood, W.M.J. Green, "long-wavelength silicon photonic integrated circuits", 11th International Conference on Group IV Photonics (GFP), France, pp. 23-24 (2014).

4. G. Roelkens, U.D. Dave, A. Gassenq, N. Hattasan, C. Hu, B. Kuyken, F. Leo, A.Malik, M. Muneeb, E.M.P. Ryckeboer, S. Uvin, Z. Hens, R. Baets, Y. Shimura, F. Gencarelli, B. Vincent, R. Loo, J. Van Campenhout, L. Cerutti, J.B. Rodriguez, E. Torunie, X. Chen, M. Nedeljkovic, G. Mashanovich, L. Shen, N. Healy, A.C. Peacock, X. Liu, R. Osgood, W. Green, "Mid-IR heterogeneous silicon photonics", Conference on Silicon Photonics IX, United States, pp. article 899316 (6 pages) (2014).

5. G. Roelkens, U.D. Dave, A. Gassenq, N. Hattasan, C. Hu, B. Kuyken, F. Leo, A.Malik, M. Muneeb, E.M.P. Ryckeboer, S. Uvin, Z. Hens, R. Baets, Y. Shimura, F. Gencarelli, B. Vincent, R. Loo, J. Van Campenhout, L. Cerutti, J. Rodriguez, E. Tournie, X. Chen, M. Nedeljkovic, G.Z. Mashanovich, L. Shen, N. Healy, A.C. Peacock, X. Liu, R. M. Osgood, W. Green, "Mid-IR heterogeneous silicon photonics", Photonics West 2014, 899316, (2013).

6. A.Malik, M. Muneeb, S. Pathak, Y.Shimura, J. Van Campenhout, R.Loo, G. Roelkens, "Germanium-on-Silicon Mid-Infrared Photonic Integrated Circuits", Proceedings of the 18th Annual Symposium of the IEEE Photonics Society Belenux Chapter, pp. 21-24 (2013).

7. M. Muneeb, X. Chen, E.M.P. Ryckeboer, A.Malik, G. Mashanovich, G. Roelkens, "Silicon-o-insulator mid-infrared planar concave grating based

(de)multiplexer", IEEE Photonic Conference 2013 (IPC), United States, pp. paper MF 1.2 (2013).

8. A.Malik, M. Muneeb, Yosuke Shimura, Joris Van Campenhout, R.Loo, G. Roelkens, "Germanium-on-silicon mid-infrared waveguides and Mach-Zehnder interferometers", IEEE Photonics Conference 2013 (IPC), United States, pp. paper MF 1.4 (2013).

9. G. Roelkens, B. Kuyken, F. Leo, N. Hattasan, E.M.P. Ryckeboer, M. Muneeb, C. Hu, A.Malik, Z. Hens, R. Baets, Y. Shimura, F. Gencarelli, B. Vincent, R. Loo, P. Verheyen, G. Lepage , J. Van Campenhout, L. Cerutti, J.B. Rodriguez, E. Tournie, X. Chen, M. Nedeljkovic, G. Mashanovich, X. Liu, W. Green, "Long-wavelength III-V/silicon photonic integrated circuits", Advanced Photonics - OSA Optics & Photonics Congress, United States, pp. paper IT2A.1 (2013).

10. A.Malik, G. Roelkens, "Mid-IR Photonic integrated circuits", Proceedings of the 17th Annual Symposium of the IEEE Photonics Society Belenux Chapter, Belgium, pp. 151-154 (2012).